Università Politecnica delle Marche
Scuola di Dottorato di Ricerca in Scienze dell'Ingegneria
Curriculum in Ingegneria Civile, Ambientale, Edile e Architettura

---

Experimental study of alternative solutions for integrated energy and structural buildings retrofits

Ph.D Dissertation of:
Marianna Pergolini

Advisor:
Prof. Francesca Stazi

Co-Advisor:
Prof. Costanzo Di Perna

Curriculum Supervisor:
Prof. Stefano Lenci

XXXI ciclo del Corso di Dottorato di Ricerca
in Ingegneria Civile, Ambientale, Edile e Architettura

Università Politecnica delle Marche
Scuola di Dottorato di Ricerca in Scienze dell’Ingegneria
Facoltà di Ingegneria
Via Brecce Bianche – 60131 Ancona (An), Italy

To my grandparents

Aknowledgements

First and foremost, I want to thank my advisor Prof. Francesca Stazi for the continuous support of my PhD study. Her office was always open whenever I ran into a trouble spot or had a question about my research or writing. My sincere thanks also go to my co-advisor, Prof. Costanzo Di Perna for his patience, willingness, and immense knowledge.
A special mention goes to the other PhD fellows of my department (the infamous CeCAS group). Sharing the everyday ups and down of the last three years with them was amusing, especially when food was involved.
Finally, I want to thank my family. Really, this milestone would have not have been possible without them. Again, thank you.

Abstract

A holistic approach in the design of interventions is strongly boosted by recent Horizon Calls on energy-efficiency to perform a more sustainable and cost-effective building rehabilitation. Solving all building deficiencies at once with a unique solution is highly promoted, but the topic is still seldom addressed by the scientific community. The present thesis outlines an experimental research on alternative solutions for energy and structural retrofits strategies for wooden buildings.

The first objective of the study deals with the energy optimization of cross laminated timber (CLT) buildings, that will eventually be implemented with a structural rehabilitation. The second objective focuses on an integrated energy and structural alternative solution for platform frame (PF) buildings by means of a masonry wall, made of unbaked earth blocks, on the internal and external sides of the structure, to optimize its global shear behavior and thermal responsiveness.

The methodology comprised: extensive monitoring campaigns on a case study in different seasons and operative conditions, by means of simultaneous comparative studies of different internal and external linings; mechanical testing on unbaked masonry wallettes by means of digital image correlation (DIC) technique.

Firstly, the outcomes demonstrated that, for CLT buildings, in the Mediterranean climate, the adoption of a massive innermost layer guarantees the best thermal performance on annual basis under different indoor operative conditions. Moreover, a ventilated technology, with an outer thermal mass, is the best choice yearly, being beneficial for minimizing the incoming heat fluxes through the envelope.

Secondly, regarding the retrofit strategy of PF buildings, it was experimentally verified that the earth block masonry has a good thermal performance, regardless of the switching on/off of the cooling system, and that the presence of the dovetail joints improve the overall shear behavior of masonry veneer walls in wooden light-framing structures.

Contents

List of Figures

List of Tables

Chapter 1

Introduction

The European commission is stressing the importance of the development of solutions to guide the building renovation by adopting cost-effective and multi-functional techniques. Innovative energy efficient and price affordable breakthrough solutions should be developed through a deep holistic approach. The existing building stock is characterized by poor energy efficiency, high seismic vulnerability and indoor discomfort, thus representing a large improvement potential. The way to transform existing energy-consuming and seismic-prone buildings into energy-efficient and seismic-resistant ones was addressed in the past and several techniques able to reduce seismic vulnerability, as well as heat loss, have been set up and implemented. However, these techniques dealt separately with the different components of the building at hand, in order to increase either the seismic or thermal performance.

Therefore, a deep renovation is not merely about optimizing the technical performance of a building, but prescribes a holistic approach, in which measures are considered for their interdependence rather than as separate elements. Nevertheless, even though the adoption of combined thermal and structural features is deeply encouraged by the very recent Horizon Calls on energy-efficiency, the issue is still scarcely investigated by the scientific scene. Indeed, only few integrated retrofit solutions have been developed in the research field, which are mainly based on a “double skin” approach.

The present thesis deals with alternative solutions concerning the external building envelope by combining in a novel and holistic manner the most recent technologies present on the market. The work mainly focuses on two integrated technologies both based on the use of wood. The first one adopts cross laminated timber (CLT) panels, while the other focuses on platform-frame (PF) structures, with the aim of optimizing their energy and structural behavior.

The CLT panels are designed as infills (shear dissipating structure) in a reinforced concrete (RC) framed structure. In literature, studies that have covered the possibility of introducing CLT panels in RC frames buildings are very few. The assumed strategy provides for the replacement of a damaged external infill with a CLT shear wall, externally insulated. The energy efficiency upgrading could be guaranteed by the presence of vented air gap on the external side (Fig.1.1). The first objective of the present research regards the energy optimization of such technique, by means of experimental comparative studies of alternative internal and external solutions with different inertial features in order to reduce the thermal stresses coming both from the indoors and outdoors. The structural optimization of this technique panel is still at the first stage and will continue with other studies of the same research group. Therefore, such preliminary findings will not be tackled in this thesis.

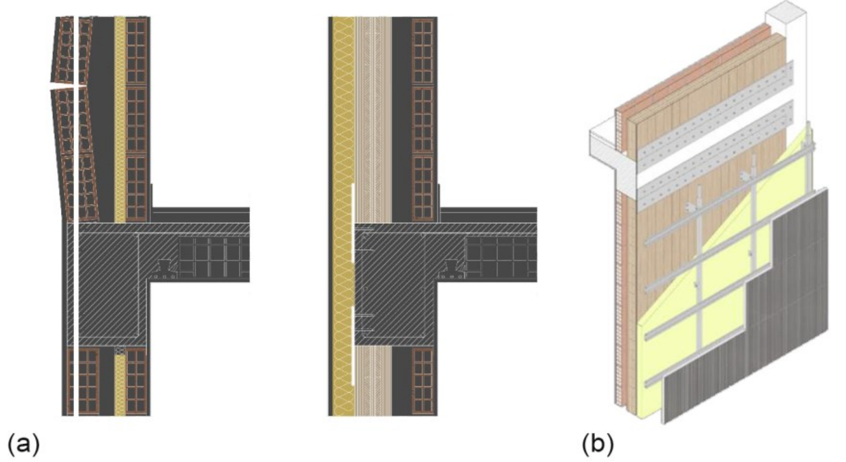

Figure 1.1: (a) Example of CLT infill panel with eternal insulation and (b) with a hooked external skin, namely ventilated façade, as integrated seismic and energy strategy.

Platform Frame (PF) structures are usually characterized by a wooden framing comprised of vertical studs at reduced distance (typically 60 cm or closer). The bracing could be either made of oriented strand boards (OSB) or diagonal fir boards. The integrated strategy taken into account provides for the adoption of enclosure walls, positioned on both sides of the sheathing boards, made of unfired extruded earth blocks in order to upgrade the structure thermal responsiveness and shear behavior (Fig.1.2). The second objective of the present work aims at experimentally assessing the thermal contribution of a masonry veneer wall for platform frame bracing, made of unbaked clay blocks for the mitigation of summer indoor heat gains. The mechanical behavior of such technology is also determined in order to investigate its shear behavior and structural potential.

The research was carried out through a multi-disciplinary approach and included a series of experimental activities. Extensive monitoring campaigns were performed on a lightweight and hyper insulated CLT mock-up, with the aim of collecting data on the thermal behavior of the internal and external tested solutions with respect to variable boundary conditions coming from the outdoor and indoor environment. Moreover, a set of laboratory tests involving unbaked clay masonry walls were performed in order to gain insights into the mechanical shear behavior of such a technology.

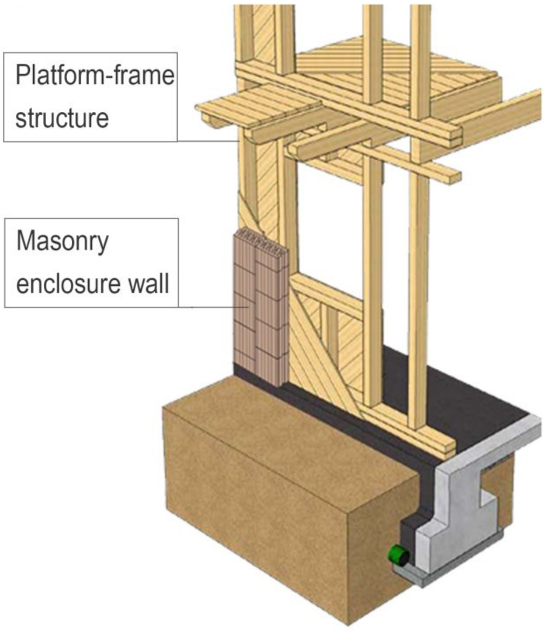

Figure 1.2: Example of PF structure with masonry enclosure walls on the inner and outer sides as integrated seismic and energy strategy.

Chapter 2

Literary review

2.1 Combined energy and structural retrofit strategies

The construction sector is one of the key consumers of energy in Europe; it has therefore a huge impact on the economic, ecological and social environment. In this light, Europe is involved in several initiatives and strategies aimed at making this sector one of the most competitive and innovative, focusing on the achievement of the environmental and energy targets in line with 2020 Europe Strategy and EU 2050 roadmap, but also ensuring safety both in ordinary conditions and in presence of exceptional events, such as earthquakes [1].

The analyses of the European building stock show that about 40% of existing buildings in Europe are old and obsolete. They were designed not only by disregarding energy efficiency measures but also without any seismic safety standard or any reference to good anti-seismic construction practice [2].

Common structural and energy retrofit interventions were employed in the past at separate moments. For example, the simplest and most common energy retrofit approach was to upgrade existing equipment, where the equipment's efficiency improvements are the main contribution towards energy savings. Often these retrofits were implemented incrementally, applied one at a time over the course of several years, often coinciding with the end-of-life replacement of existing equipment, or with tenant improvements [3].

Therefore, today`s challenge in the retrofitting sector is the realization of building retrofits that consider ecological and social aspects under the pressure of cost-optimization and climate policy goals. The most recently Horizon 2020 calls address the need to develop methodologies and solutions, integrating the most promising cost-effective technologies and considering occupants behavior [4].

Innovative, highly energy efficient and price affordable solutions with long service life should be selected through a deep holistic approach for building envelopes, systems, and energy management. According to very recent hierarchical approaches, the retrofitting of the building envelopes to higher standards is the first step to achieving zero carbon refurbishments [5].

Thus far, the most commonly adopted solution for envelope energy retrofit is the external thermal insulation composite system, namely ETICS. However, this solution is not enough to reach the very high energy saving goals that were set, unless adopting very high thickness. Advanced studies on the cost-efficacy of retrofitting suggest the adoption of capacitive materials [6]. But of major importance, no response to the structural safety issue is given by adopting such ETICS solutions. Instead, external global solutions, aimed at complementing the existing structures with new earthquake-resistant systems, namely shear walls either over-resistant or dissipative, are very promising from a cost-effectiveness point of view. Therefore, external insulating over-resistant skins could be a cost-effective combination of both thermal and structural performance. Integrated interventions will allow saving energy in the whole building renovation process and strongly decrease the installation times [7].

Even though the adoption of integrated holistic solutions is highly encouraged by the EU and scientific community, very rarely the studies were focused on both thermal and structural aspects [8,9]. Due to this lack, my research contributes to the topic by experimentally assessing alternative solutions for combined energy and structural retrofits.

2.2 Optimized walls composition

It is well acknowledged that the reduction of the energy consumption throughout the building stock is a priority in the European roadmap to contain the greenhouse gas emissions. The NZEB paradigm, prospected by the European Directive 2010/31/CE, has established high performance targets for new buildings that entail optimized design of the single components, as well as of the building as a whole system framed in its specific climatic context [1,10].

Against such backdrop, the envelope's role is pivotal, since it governs the amount of energy necessary to maintain adequate indoor comfort levels, by arbitrating the perturbing action of the weather outside and occupancy patterns inside [5].

In winter, as apparent from previous studies [11–15], a proper design allows to retain the heat, that is stored inside because of the free gains given by internal and external sources, thus limiting the heating system workload. Conversely, in the warm seasons and especially in cooling-dominated climates, the goal is to dissipate the potential overheat or at least to shave/shift its peak so that less heat stays entrapped: by misaligning the hours of maximum outdoor temperature and solar radiation and the time by which the heat is released, the benefits in summertime and those in wintertime get harmonized [16–18].

Indeed, envelopes with a great amount of thermal mass, phase out and flatten out the heat flow triggered by external ambient temperature fluctuations and display a reduced and delayed reaction to the perturbing excitation; this transient effect is referred to as the thermal inertia of the building and stands for the resistance to temperature change of the components interacting dynamically with the outdoors, during a full heating/cooling cycle (24 hours). As a consequence, a thermal flywheel behavior is established and, when probably tweaked, this might assist in creating favorable indoor thermal comfort conditions without the need for active cooling and heating, especially in climates with high diurnal temperature variations [19].

It is well proven though that, when it comes to very hot areas, other cooling strategies need to be in place to counteract the discomfort events that are likely to occur given the overabundance of heat gains and the recent escalation of extreme climate events such as tropical nights [20].

Extensive literature exists on the topic, notably to define the design criteria for optimized walls composition. Even though the ingredients for designing a high performance envelope are pretty much disclosed, designers are still faced with a challenging task since the best wall composition comes out of a tradeoff between the simultaneous optimization of diverse parameters: the steady state thermal transmittance U should be advantageously minimized to optimize the winter performance, while in summer, high time lags t (for example close to 10-12h) and internal areal heat capacity κ_1 alongside with low decrement factors f are postulated to reduce the fluctuations of the indoor air temperature and avert the cumulative effect of multiple simultaneous heat fluxes [21].

Several studies advocate that a general practice suitable to maximize both energy savings and thermal comfort for most buildings and climates is to locate higher amounts of thermal mass at the inner side of the thermal insulation: [13, 19, 21–25].

Bearing this in mind, recently developed solutions turned out to be inefficient. For instance, light and hyper-insulated building configurations, adopted in the last decades, not only in the North–European region, but also in the Mediterranean area, currently achieve very low thermal transmittance U, with external thick insulation layers that act as thermal barriers blocking the ingoing and outgoing heat flows, hence limiting the heat transmission through the external wall [26,27].

Yet, such envelope setting, especially when unshaded, is way far from attaining an optimal performance in summer time, when the heat barrier effect backfires, turning into a detrimental “oven” effect: overheating frequently occurs and impinges on cooling consumptions. Latest researches have demonstrated that for this type of envelopes, the adoption of an internal finishing layer with appropriate thermo-physical properties can reduce the discomfort [28]. In these studies the effect of various combination of κ_1 and f are announced but they are preponderantly simulation-based without any experimental double-check on this particular feature.

Moreover, the exact energy saving potential and comfort benefit bound to thermal inertia is hard to ascertain, not just for the plethora of parameters at stake (which contribution is rather challenging to isolate), but also for the lack of proper metrics, experimental procedures and standards to thoroughly describe the effect [19]. This mirrors in the extensive variability of results in literature: the reported energy saving, for instance, scatters from + 10% [29] to - 80% [15]. Such variability stems from the time varying nature of the heat flows, first in line the daily swing of outdoor air temperature and solar radiation.

The present work contributes to the international debate by simultaneously evaluate the thermal performance of multi layered external walls in highly insulated and lightweight CLT buildings, characterized by the same wall composition but with different internal linings (featuring different levels of internal areal heat capacity κ_1 and decrement factor f).

2.3 Mitigating the urban microclimate through the building envelope

Recently, much research effort is focused on a new social challenge regarding the mitigation of the urban overheating [30,31]. It is due to the elevate density of buildings creating urban canyons, highly absorbing materials and the lack of water for evapotranspiration [32]. The reduction of urban temperatures will determine energy saving on cooling demand of buildings, improvement of urban building thermal comfort and benefits on human health [33,34]. Moreover, the lowering of outdoor heat peaks will limit the degradation of construction material [35]. A cost-effective solution to such problems could be the adoption of ventilated layers on the external building skin that will remove the heat in a passive way, thus cooling down the air and reducing the thermal stress on constructive components [36].

Within this framework, Ventilated Skins (VS) were born as rain screens in the roadmap for a constant pursuit of durability improvement of outer building surfaces, attracting the attention of designers for both retrofitting and new buildings. Moreover, international studies demonstrated that the adoption of ventilated systems could be also an effective passive cooling strategy on annual basis, with respect to the unventilated option [37].

The ventilated skin is an external coating system, using mechanical anchoring points to secure an additional extern skin to the building envelope. It consists of four functional layers (from the inner side to the outer side): (i) massive layer; (ii) continuous insulation layer applied on the external wall; (iii) ventilation chamber with lower and upper openings connected to the outdoor air; (iv) external cladding [38,39]. The parameters influencing the air gap behavior and the energy performance could be divided in two main categories: (i) outdoor boundary conditions, such as the geographical localization [40], the solar radiation [41] and wind speed [42]; (ii) design choices, namely width and height of the ventilation gap [43], external cladding material [6] and joints configuration that can be either open [44] or closed [45] . These abovementioned researches focused on the evaluation of one single facade type but no study concerned the simultaneous comparison between walls with different external layers.

The ventilated skin is both an efficient system for summer and winter. In the summertime, the thermal gradient between upper and lower ends of the ventilation layer façade activates an air flow (driven by buoyancy and wind forces) allowing the heated air in the ventilation chamber to be expelled through the outlet opening, hence reducing the heat gains towards the indoor [35,38,40,45]. Moreover, the stack effect could help reducing the heat peaks of the external claddings, thus mitigating the heat transfer to the local outdoors. While there is a great amount of literature on the former aspect, very limited information is available on the latter [46]. In the wintertime, the ventilation gap behaves as a thermal buffer, accumulating heat and dampening the temperature difference between inside and outside, hence transmission losses can be curbed. Moreover, it might affect positively the thermal resistance of the wall. This issue was very rarely surveyed in existing studies [47]. Within this framework, my experimental research contributes by identifying the optimal mass for the external cladding of such ventilated skins through simultaneous experimental comparison of three prototypes: one lightweight, one with internal mass and external lightweight cladding and one with external mass cladding. Extensive measurements were collected and the data processing allowed to establish a comparison between the configurations under study, both in terms of thermo-physical performance and natural ventilation potential, with respect to the buoyancy and wind forces.

2.4 Unbaked clay in the building sector

Benefits associated with the adoption of unfired clay units include the improvement of the building energy efficiency [48][49], and its environmental and economic sustainability [50]–[52]. The blocks are made of a mixture of natural components (clay, water and wooden fibres). Clay acts as natural binder, conferring strength to the building component. However, this material can be subject to cracks due to drying shrinkage [53], leading to poor mechanical properties.

The compressive strength of raw clay can be enhanced by the addition of stabilizers and it is influenced by the manufacturing process. Regarding the adoption of stabilizers, numerous studies suggest the use of fibres within the mixture to favour the drying process and to allow water drainage towards the outdoor. This prevents the outbreak of tensile forces and the consequent drying shrinkage [54]. The use of natural stabilizers, such as pine, sisal and straw fibres, has been researched in [55]–[57] while the employment of artificial stabilizers, such as plastic and polystyrene fabric, was deepened by [58]. Regarding the manufacturing process, building technique practice is considered to be one of the crucial parameters affecting performance of earth block masonry [59]. Among the widespread methods of unbaked earth construction, the most promising is represented by the extrusion of bricks, since it determines comparable strength values with respect to traditional fired brick, with lower environmental impact [60]. In this research, it has been chosen an unbaked extruded block with wood fibers which couples the most advantageous manufacturing technique with natural stabilization method. My contribute was to acquire better knowledge of the mechanical properties of a masonry veneer wall with horizontally staggered bed joints for the structural retrofit of a PF building.

2.5 Adoption of DIC in structural engineering

The Standard Test Methods of masonry [61], [62] in structural mechanics provide the adoption of contact sensors, usually linear variable displacement transducers (LVDTs) and strain gauges, for the measurement of the displacement and strain, respectively. A wide spectrum of past and present researches have employed this technique [63], [64]. However, the application of this method provides a restricted selection of measurement points, limiting the evaluation of the strains and stresses. Moreover, crack maps are hand-drawn based on visual inspection, thus being prone to human errors [65].

Currently, in the building structure framework, one of the most promising measurement method is the Digital Image Correlation (DIC). The adoption of such optical and non-destructive contactless method allows to obtain a remarkable amount of information relative to the strain state of the material/structure and a complete reconstruction of the crack pattern [66]. Several authors have advantageously applied this technique in different frameworks, such as the analysis of the mechanical and fracture behavior of reinforced concrete beams, see [67]–[69]. Other authors used the correlation of digital image in tensile and bond tests on composite reinforcements, comprising different textiles and matrices [67].
Even though the use of DIC in structural engineering has increased over the last two decades, its application is rather limited on masonry structures. The following researches applied this technique on different scale levels: Caggegi et al. [68] studied small specimens (320 × 250 × 120mm^3) of a textile reinforced mortar (TRM), used for historical masonry structures strengthening; Ghiassi et al. [70] investigated the bonding behavior in FRP–brick specimens' interfaces (200 x 100 x 50 mm^3); finally, Markulak et al. [71] characterized the compression and shear behavior of small- scale masonry units (490 x 390 x 120 mm^3).

Recently, researchers have acknowledged that DIC could improve the understanding and the mechanical characterization of masonry structures, thus they have applied it also at higher scales, namely, wallettes and full-scale prototypes (see e.g.[65]). A major step forward is represented by two pilot studies that used the DIC method for the assessment of displacement and strain fields in full-scale masonry panels subject to cyclic lateral loads. In [72], Guerrero et. al. tested infilled and partially infilled frames specimens (2.80 x 2.00 m^2) under cyclical loading. In particular, DIC was useful for the assessment of the boundary conditions, describing the contact between the infill and the RC frame at the variation of the lateral load magnitude. Real-scale confined masonry walls (2.43 x 2.49 m^2) were tested under reverse cycle load also by Ghorbani et al.[73]. High-resolution crack maps enabled design implications. Recently, the use of DIC was also extended to map the crack propagation in existing masonry building [74].

My contribute to the topic was to proceed along this path by investigating, through DIC, the mechanical behavior of a new type of masonry wall made of extruded unbaked clay blocks with horizontally staggered bed joints for the structural retrofit of PF buildings.

Chapter 3

Phases and experimental methods

The methodology adopted in this research integrates in-field experimental activities on a case study to collect real measured data and structural testing on specimens to characterize masonry assemblies. This chapter is divided in three sections: the first one (3.1) outlines the distinct stages of the work, the second one (3.2) describes the selected case studies and the third one (3.3) illustrates the assumed experimental methods.

3.1 Phases

The experimental research regards integrated solutions for the buildings energy and structural retrofits. The present work is divided in two main parts:
(i) *energy optimization of cross laminated timber buildings*, by means of comparative studies of lightweight and massive internal and external linings to minimize the thermal stress coming from the indoor and outdoor environments;
(ii) *energy and seismic retrofit strategy for platform frame buildings*, by means of thermal and mechanical evaluation of an unbaked masonry wall.

The first phase encompassed the thermal responsiveness of a multi-layered and highly-insulated CLT building subject to distinct indoor and outdoor boundary conditions. Initially, the research concerned the evaluation of four internal linings with different inertial features in order to (i) collect experimental data on the thermal response of the innermost side of the envelope at the varying of the internal loads; (ii) highlight the incidence of the internal thermal inertia on the daily temperature fluctuations. A preliminary study of the thermo-physical properties and transient parameters of a fictitious building material was conducted in order to identify the features that affect the internal areal heat capacity κ_1 and decrement factor f. Consequently, a selection of internal linings to represent increasing levels of thermal capacity and decreasing ones of decrement factor were chosen. Four different internal linings typologies were compared: plasterboard (as baseline reference), double layer of raw clay panel, triple layer of raw clay panel and brick coupled with an additional EPS layer. These linings had increasing levels of internal areal heat capacity κ_1 and decreasing levels of decrement factor $\jmath$, respectively. The panels (60 cm x 200 cm each) were installed on the south- facing wall of a hyper-insulated and lightweight mock-up and monitored yearly. The heat transfer through each portion of the south wall was assessed under different internal heat loads and throughout the seasons. The comparison was conducted in terms of flywheel effect (heat flowing), responsiveness (time trends) and expected operative indoor conditions (surface temperature).

Further, the research focused on the evaluation of three ventilated skins prototypes in which the massive layers assumed different positions with respect to the ventilated air cavity in order to (i) understand how different inertial layering affects the thermal performance of the ventilated technology; (ii) outline the configuration that exhibits the better thermal behaviour for the indoors and heat losses through the ventilated component. Three ventilated configurations of distinct inertial properties were designed and constructed on the west-facing wall of a mock-up: L, with a lightweight external enclosure, IM and EM with a massive layer immediately before and after the air cavity, respectively. The heat transfers through each facade were simultaneously monitored and an extensive field of measurements was obtained in summer and winter. The trends of the external surface temperatures, the airflow parameters (air temperature and speed) in the gaps and the surface temperatures and heat fluxes towards the internal side of the wall were compared in terms of buoyancy and wind-driven ventilation potential.

The second phase covered the combined energy and seismic retrofit strategy for lightweight wooden buildings that adopts enclosure walls made of unbaked extruded clay blocks both on the innermost and outermost sides of the load-bearing structures. The thermal behaviour of the unbaked wall was assessed in the summer season in order to evaluate its mitigation potential against the indoor overheating phenomenon. A panel made of unbaked earth blocks was installed on the south-facing wall of a mock-up and was monitored in the warmest months simultaneously with plasterboard and 2 layers of dry clay lining, for comparison. The linings were subject to different cooling scenarios. Surface temperature and heath flux profiles of the three linings were retrieved and compared under free-running and cooling regimes. Moreover, a set of thermocouples was inserted in the block holes as a means of investigating its inertial behaviour.

The seismic potential of the unbaked wall with horizontally staggered bed joints, made of extruded unfired clay blocks, was determined through a set of laboratory tests with the purpose of (i) deepen the knowledge of the mechanical properties of such a configuration and (ii) evaluate possible applications as load bearing walls. The study was structured in:

- *Preliminary phase*: material characterization of unfired blocks in order to obtain the compressive strength of single units and the initial shear strength of triplets. The displacements and strains fields of the preliminary phase were obtained by means of traditional contact measurement sensors.
- *Main phase*: mechanical characterization of the earth wall in order to obtain its compressive and shear strengths. The displacements and strains fields of the main phase were obtained by employing the digital image correlation (DIC) technique.

3.2 Case studies

3.2.1 Building with cross laminated timber wall

The thermal behaviour of internal and external linings of a CLT building envelope was assessed through an extensive in-field monitoring campaign carried out on a mock-up.

The mock-up is located in Agugliano, Central Italy, climatic zone D (latitude: 43° 62’ N; longitude: 13°37’ E; elevation 137 m a.s.l.). According to Köeppen-Geiger classification, the climatic condition is classified as Csa (temperate climate) where the hottest month is August (average temperature around 32°C) and the coldest one is January (average temperature around 8°C with significant rainfall). The test room is representative of a full-scale, compact indoor environment (Fig.3.1). The prototype is a rectangular room with gross area equal to (3.2×5.2 m^2). The net area is 12.2 m^2, the indoor volume is 36 m^3 and the surface to volume ratio (S/V) is 1.88 m^{-1}. The load bearing structure is realized with CLT panels. The building is hyper-insulated, with rock wool layers placed both in the external and in the internal side. The thermal transmittance of the floor, vertical walls and roof are 0.248 W/(m^2K), 0.22 W/(m^2K) and 0.205 W/(m^2K) respectively. The envelope layers succession and their thermo-physical properties are reported in Table 3.1. The test room floor is raised 40 cm above ground level to minimize thermal losses. Moreover, the mock-up is unoccupied, and it is designed without transparent surfaces in order to avoid unequal contributions of the solar radiation and uncontrollable internal heat gains. A greenhouse was later built adjacent to the south facing wall.

Figure 3.1: External view of the mock-up.

Table 3.1. Thermo-physical properties of the envelope layers.

Material	Thickness t (cm)	Thermal conductivity λ (W/(mK))	Specific heat capacity c (J/(kgK))	Density ρ (kg/m^3)
Internal Plasterboard	1.25	0.2	837	760
Vapour Barrier	-	0.17	1500	425
Internal Insulation	5	0.035	1030	70
CLT	12	1.4	2700	500
External Insulation	10	0.036	1030	90
Shaving	1.5	0.48	1000	1150

The internal linings

The internal areal heat capacity κ_I of a wall envelope depends on the inner lining material thermo-physical properties, namely on its thickness t, thermal conductivity λ, specific heat capacity c and density ρ. Therefore, in order to deeply understand the relation between such properties and the transient thermal parameters, a fictitious material was considered for the internal panel.

The fictitious material is characterized by a thickness of 20 mm, a thermal conductivity of 0.3 W/(mK), a specific heat capacity of 1000 Jkg/K and a density of 1200 kg/m^3. These values were varied (one at a time within specific thresholds based on UNI 10351:2015) to verify their incidence on κ_I and f parameters. The decrement factor and internal areal heat capacity were calculated according to UNI EN ISO 13786. The decrement factor f is the ratio between the modulus of the dynamic thermal transmittance Y_{12} to the steady state thermal transmittance U and it can be expressed by the following equation:

$$f = (|Y_{12}|) \ / \ U \qquad (1)$$

The internal areal heat capacity κ_1 is described as the heat capacity C_1 divided by area of element A where the heat capacity is the modulus of the net periodic thermal conductance divided by the angular frequency ω and it can be expressed as follows:

$$\kappa_1 = C_1/A = 1/\omega \ |Y_{11}–Y_{12}| \qquad (2)$$

Both formula include complex numbers and involve calculations with matrices. For a more detailed description of the method the reader could refer to [75].

The external layers were the same of the test room described in the abovementioned section 3.2.1. As shown in (Fig.3.2a), internal areal heat capacity and decrement factor display opposite trends with the increase of the inner massive lining thickness. The trends of both f and κ_1 curves level up after medium values of thermal conductivity are reached (Fig.3.2b). Finally, the internal areal heat capacity considerably increases, and the decrement factor mildly decreases when heat capacity and density assume high values (Fig.3.2c and Fig.3.2d). In summary, to get a high internal areal heat capacity wall it is necessary to adopt thick innermost layers, characterized by medium thermal conductivity and high values of both heat capacity and density. For the purpose of the study here discussed, four innermost layers with the following features were chosen:

- L, representative of a material with low thermal capacity, as a baseline for subsequent comparisons;
- Lining M, indicative of a medium thermal capacity layer;
- Lining H, typical of a high thermal capacity material;
- Lining H_I, with high thermal capacity and an additional layer of internal insulation.

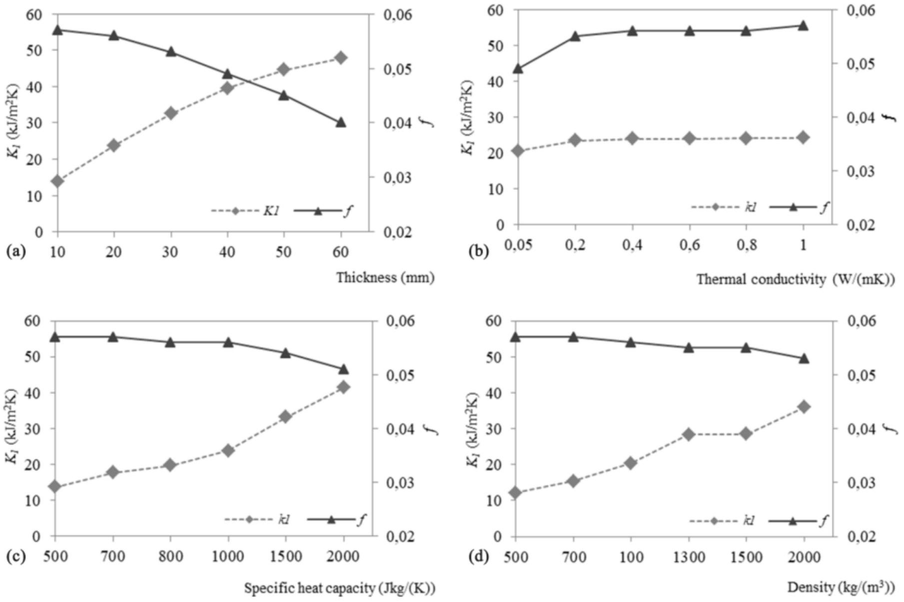

Figure 3.2: Internal areal heat capacity and decrement factor of a fictitious material at the varying of its (a) thickness (λ= 0.3 W/(mK), *c*=1000 Jkg/K, ρ=1200 kg/m^3), (b) thermal conductivity (*t*=20 mm, *c*=1000 Jkg/K, ρ=1200 kg/m^3), (c) specific heat capacity (*t*=20 mm, λ= 0.3 W/(mK), ρ=1200 kg/m^3), (d) density (*t*=20 mm, λ= 0.3 W/(mK), *c*=1000 Jkg/K).

Within the mock-up, the four internal linings L, M, H and H_I were installed and tested on the south facing wall. Table 3.2 provides information on the walls composition: basically, lining L stands for classic plasterboard finishing which is replaced, in the case of lining M by a 2.8-cm-thick panel of dry clay, in the case of lining H by a furtherly thicker dry clay layer and in the case of lining H_I by two 4 cm-thick layers of insulation and bricks respectively. Table 3.3 reports the steady and transient parameters of the distinct envelopes.

Table 3.2: Thermal characteristics of the innermost layers.

		Lining L	Lining M	Lining H	Lining H_I
Thickness *t*	(cm)	1.25	2.8	4.2	8
Thermal Conductivity λ	(W/mK)	0.2	0.47	0.47	0.398
Specific Heat *c*	(J/kgK)	837	1000	1000	1000
Density ρ	(kg/m^3)	760	1300	1300	1491

Table 3.3. Characteristics of the entire walls.

Steady and transient parameters	Lining L	Lining M	Lining H	Lining H_I
Steady Transmittance U (W/(m^{2}K))	0.22	0.22	0.218	0.179
Decrement Factor *f*	0.076	0.072	0.065	0.047
Time Lag Δt (h)	8.39	9.46	10.23	11.02
Periodic Thermal Transmittance Y_{12} (W/(m^{2}K))	0.017	0.016	0.014	0.0008
Internal Areal Heat Capacity κ_1 (kJ/(m^{2}K))	12	33	44	47

Wall envelopes with innermost layers L, M and H present similar steady state thermal transmittance U, around 0.22 W/(m^{2}K), whereas the addition of a further insulation layer on the internal side of the wall (as occurs for lining H_I) significantly increases the thermal resistance of the wall (therefore lowering the U-value to 0.179 W/(m^{2}K)). The selected wall configurations exhibit four increasing levels of internal areal heat capacity, from a minimum of 12 kJ/(m^{2}K) (lining L) to a maximum of 47 kJ/(m^{2}K) (lining H_I). Low and medium thermal capacity envelopes (with lining L and M) have comparable values of decrement factor (around 0.07) and similar time lags (about 1 h gap) but substantially different levels of internal areal heat capacity κ_1, with lining M almost triplicating lining L's value. High thermal capacity wall configurations (with lining H and H_I) have similar values of internal areal heat capacity (over 40 kJ/(m^{2}K)) but quite different levels of decrement factor (30% reduction between the H_I and the H configurations).

The ventilated prototypes

The west-facing wall of the same mock-up was used to install the ventilated prototypes. The wall covers 9 m^2 (3.22 m length x 2.80 m height) and three rectangular-shaped ventilated skins were tailor made to fit the available surface, with each modulus of 1 m length x 2.30 m height. (Fig.3.3).

As specified in Table 3.4, the first configuration (L) is the lightweight typology. It was conceived with an aerated gap enclosed by a white plastered oriented strand board (OSB) panel and it is used as reference for comparisons. The second configuration (IM) presents the massive layer adjacent to the insulation material and the external gap enclosed by the same white plastered as above. The third configuration (EM) features an outer mass with external white plaster. It was intentionally adopted the same surface color for the three outer skins as to prevent any bias. Regarding the optical properties, white plaster exhibits an emissivity ε of 0.9 and a solar reflectance R of 0.60. The cross-section drawing of the three walls is illustrated in (Fig.3.4). The thermo-physical properties of the materials adopted are listed in Table 3.5.

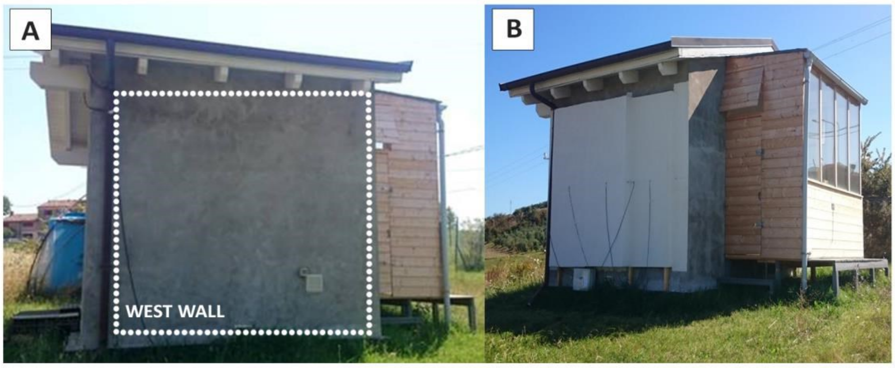

Figure 3.3: West oriented wall (a) before the study and (b) after, with the built ventilated facades.

Table 3.4: Composition of the three ventilated envelopes.

	VS with no mass (L)	VS with internal mass (IM)	VS with external mass (EM)
	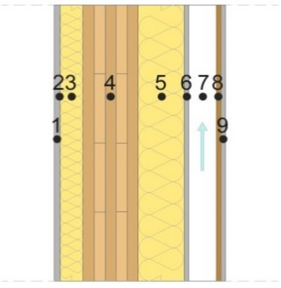	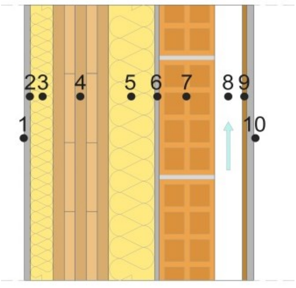	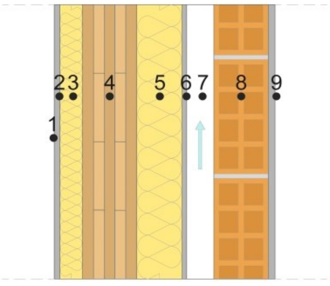
	Layer		
1	Internal Plasterboard	Internal Plasterboard	Internal Plasterboard
2	Vapour Barrier	Vapour Barrier	Vapour Barrier
3	Internal Insulation	Internal Insulation	Internal Insulation
4	Cross laminated timber	Cross laminated timber	Cross laminated timber
5	External Insulation	External Insulation	External Insulation
6	Shaving	Shaving	Shaving
7	Air Cavity	Hollow Bricks	Air Cavity
8	OSB Panel	Air Cavity	Hollow Bricks

9	External Plaster	OSB Panel	External Plaster
10	-	External Plaster	-

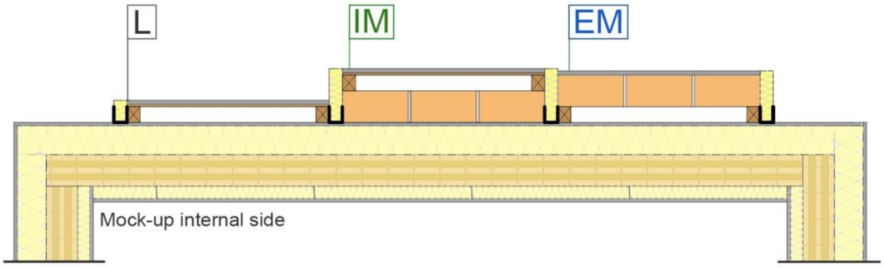

Figure 3.4: Cross-section of the three ventilated prototypes.

Table 3.5: Thermo-physical properties of the ventilated enclosures.

Material	Thickness t (cm)	Thermal conductivity λ (W/(mK))	Specific heat capacity c (J/(kgK))	Density ρ (kg/m^3)
Hollow Bricks	12	0.292	1000	920
External Plaster	0.125	0.33	1110	1150
OSB Panel	-	0.1	1700	600

The walls were assembled through the following procedure, as illustrated in (Fig.3.5):

- Vertical wooden batten support frames (0.05 x 0.06 m^2) were screwed to the cross laminated timber structure, in order to create a 6-cm thick ventilation chamber between the existing surface and the new external cladding;
- The external massive layers (IM and EM) were positioned on the bottom stainless high-grade steel support brackets, connected with the internal cross laminated timber structure, hence functioning as load bearing structures for massive overhanging layers. The brackets were equipped with a thermal cutting plate to eliminate the thermal bridges (Fig.3.5, insert A). The hollow blocks were also anchored to the cross laminated timber load-bearing panels with cavity ties, distributed for the entire surfaces, thus preventing possible out of plane mechanisms (Fig.3.5, insert B);
- XPS insulation layers were sealed on either side of each wall for enclosing the air chambers;
- An OSB panel (0.09 m width) was placed on the outer side of the air gap (IM and L). A white external shaving was adopted as external finishing for the

three walls. Honey-combed nets were placed to protect the cavities (Fig.3.5, insert C).

- The lower inlet and upper outlet are completely open and protected by a steel honey-combed mesh.

Figure 3.5: Construction phases of the ventilated prototypes.

Standards EN ISO 6946:2008 and EN ISO 13786:2008 were adopted for the characterization of the thermal parameters of the three ventilated modules, considering a well-ventilated air chamber (see Table 3.6). L and EM enclosures have equal thermal features, given the fact that the calculation was done by disregarding the thermal resistance of the air layer and all other layers between the air layer and external environment, and including an external surface resistance corresponding to still air. Moreover, the three envelopes differ for dynamic parameters, given the unequal value that the three prototypes assume regarding the external areal heat capacity κ_2. When the calculation is done by disregarding the outermost layers, when the mass is positioned on the outer side of the ventilation chamber (EM and L configuration), the κ_2 parameter reaches the lowest value (16 kJ/(m^{2}K)). When the mass is instead positioned on its inner side (IM configuration), the κ_2 parameter significantly increases (60 kJ/(m^{2}K)). Table 3.6 also reports between brackets the values of the external areal heat capacity κ_2 (obtained according to the same standards) that the experimental enclosures would assume considering still air in the air cavity and including even the outermost layers in the calculation. In this case, the three prototypes show increasing levels of inertia, with the lowest κ_2 value belonging to the L configuration (28 kJ/(m^{2}K)) and the highest one registered by the EM wall (60 kJ/(m^{2}K)).

Table 3.6: Steady state and dynamic thermal parameters of the ventilated facades.

Thermal Properties	Wall Typology		
	L	IM	EM
Thermal Trasmittance U* ($W/(m^2K)$)	0.22*	0.2	0.22
Decrement Factor f	0.08	0.04	0.08
Time Lag Δt (h)	8.4	13.9	8.4
Periodic Thermal Trasmittance Y_{12} (W/m^2K)	0.017	0.07	0.017
External Areal Heat Capacity κ_2 ($kJ/(m^2K)$)	16 (28)**	60 (40)	16 (60)

*values are calculated according to EN ISO 6946:2008 and EN ISO 13786:2008, considering a well ventilated facade by disregarding the outer layers.

**values between brackets are calculated considering all the envelope layers and still air in the gap to better highlight the increasing levels of external mass.

3.2.2 Buildings with wooden framing structure

The energy and seismic retrofit strategy was assessed for a distinct masonry enclosure wall made of unfired hollow earth blocks provided by Ton-Gruppe, an Italian construction company. The mineralogical composition of the block consists of clay (70%) as the main matrix and spoils of wooden fibers (30%) as natural stabilizers. The material properties specified by the manufacturer are listed in Table 3.7. The block is extruded through a die machine and left naturally air-dried. Each clay unit has nominal dimensions of (215 x 230 x 115 mm^3).

Table 3.7: Properties of the earth block.

Bulk density	1450 (Kg/m^3)
Moisture absorption WA	4.69 (%)
Declared thermal conductivity λ_D	0.248 (W/(mK))
Specific heat c	1.1 (kJ/(KgK))
Water vapour diffusion resistance factor	10
Fire resistance	EI 30 (min)

Each masonry unit presents one flat vertical surface and one ribbed side to improve the adhesion of the external plaster (Fig.3.6a). On the lateral surfaces, dovetail joints serve a dual purpose: guide the positioning and alignment of the clay units during the wall assembly and ensure their mechanical connection, thus enhancing the overall global behaviour.

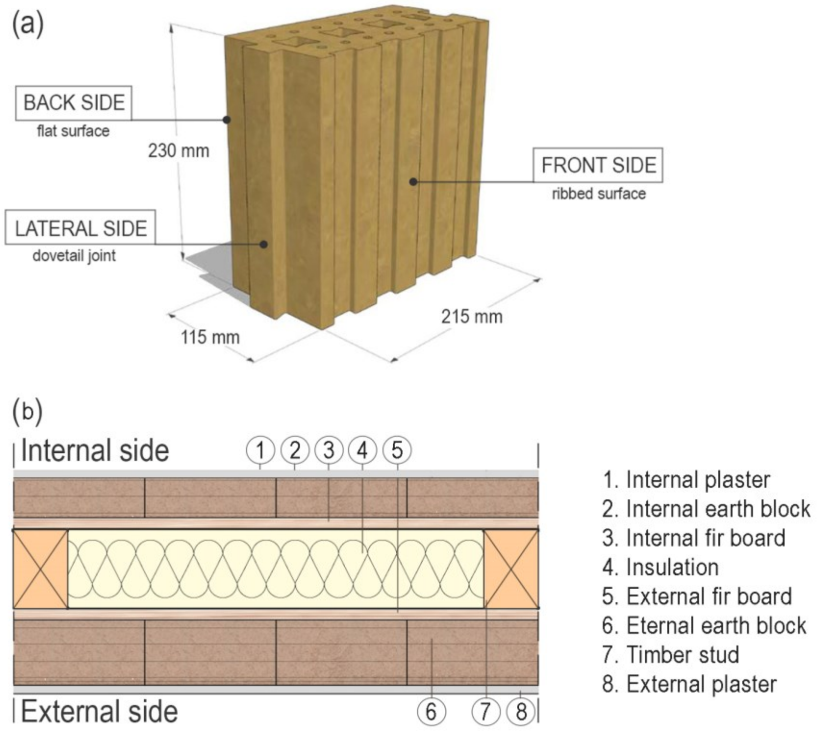

Figure 3.6: (a) Earth block geometry and (b) building envelope configuration.

The block is supported and confined by a Platform-Frame construction system in which walls and floors are composed of evenly spaced structural timber studs braced both exterior and interior sides, by 45° degree-angled fir boards, fixed by means of ring-shank nails (Fig.3.6b). Earth blocks are positioned on both sides of the fir boards. Clay masonries are anchored to the fir boards inserting flat steel plates in the horizontal joints. The construction of earth block masonry comprises the following steps:

- clay is mixed with water in a ratio of 2:1 until a dense mortar paste is formed;
- the two lateral and the bottom surfaces are uniformly soaked on the aforementioned paste;
- each block is then secured to the other by vertically scrolling it along their dovetail joints.

The thermal experimentation of the earth block panel was carried out on the mock-up described in section 3.2.1. A masonry panel made of unbaked earth blocks (0.86 x 1.15 m^2) was built on the mock-up southern-exposed wall (Fig.3.7). The steady and transient parameters of the earth block panel were calculated according to EN ISO 6946:2008 and EN ISO 13786:2008 and are summarized in Table 3.8. The adoption of a 11.5-cm-thick earth panel on the innermost side of the wall increased the thermal resistance of the wall, thus lowering the value of the thermal transmittance U to 0.192 W/(m^2K).

Figure 3.7: Earth blocks masonry panel built in the internal southbound wall.

Table 3.8: Steady and transient parameters of the earth blocks masonry panel.

Steady Transmittance U (W/(m^2K))	0.192
Decrement Factor *f*	0.013
Time Lag Δt (h)	17.4
Periodic Thermal Transmittance Y_{12} (W/(m^2K))	0.002
Internal Areal Heat Capacity κ_1 (kJ/(m^2K))	47

The mechanical experimentation was carried out on the following samples: 9 single blocks (215 x 230 x 115 mm^3); 6 triplets (configuration A with staggered horizontal joints and configuration B with aligned horizontal joints; 12 wallettes (1.075 x 1.035 x 0.115 m^3).

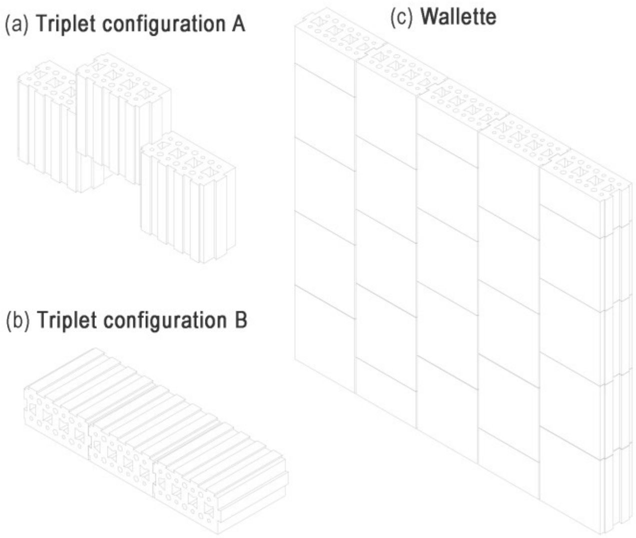

Fig. 3.8: Overview of the tested assemblies: (a) triplet configuration A, (b) triplet configuration B, (c) earth blocks wallette.

The upper bed of each sample was levelled to remove excess materials as to guarantee a plane surface for the subsequent load application. All materials and assemblies were stored in the laboratory until testing and the curing process lasted 30 days in a controlled laboratory environment (Fig.3.9).

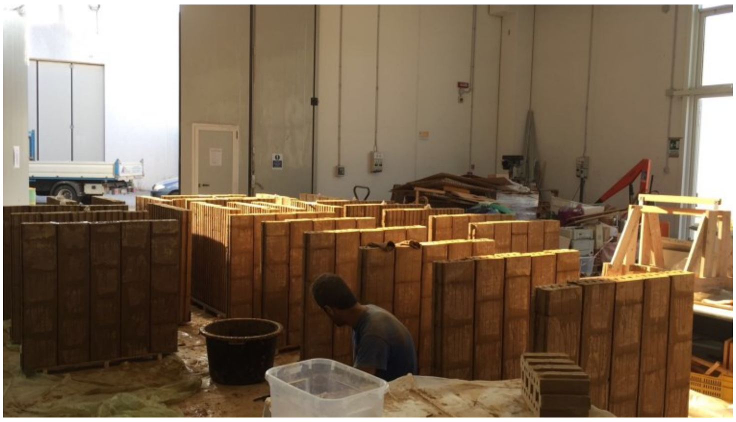

Figure 3.9: Wallettes built and stored in the laboratory environment.

3.3 Experimental methods for heat transfer studies

This chapter details the adopted experimental methodology. The three sub-sections regard the method for the evaluation of the thermal behavior of lightweight and massive internal linings (3.3.1), of the ventilated prototypes (3.3.2) and of the earth block panel (3.3.3.).

3.3.1. Evaluation of internal linings with different inertia

The yearly on-field monitoring campaign incorporated the measurements of both the indoor and outdoor microclimate conditions (Fig.3.10). The sensor network (devised in compliance with UNI EN ISO 7726:1998 and preventively calibrated) communicated to the data logger (data Taker DT85) the output of the probes with a 5-minute rate. The data was stored and analyzed by a dedicated laptop, remotely controlled by means of TeamViewer software. An articulated net of measuring equipment was installed and is presented below according to the pertaining subset of investigated parameters:

- *Outdoor climatic framework.* A weather station was used to recreate the external boundary conditions: global solar radiation, dry-bulb air temperature, relative humidity, wind speed and direction were monitored;
- *Indoor environment.* A microclimate station was placed in the mid-point of the room to detect the thermo-hygrometric variations of the internal air volume. Sensors measured wet and dry-bulb temperature;
- *Envelope performance.* A net of heat flux meters and flat thermistors was implemented on the internal side of the tested linings to map the surface temperature distribution of the south wall.

Detailed information regarding measurements, sensor types and their location is summarized in Table 3.9.

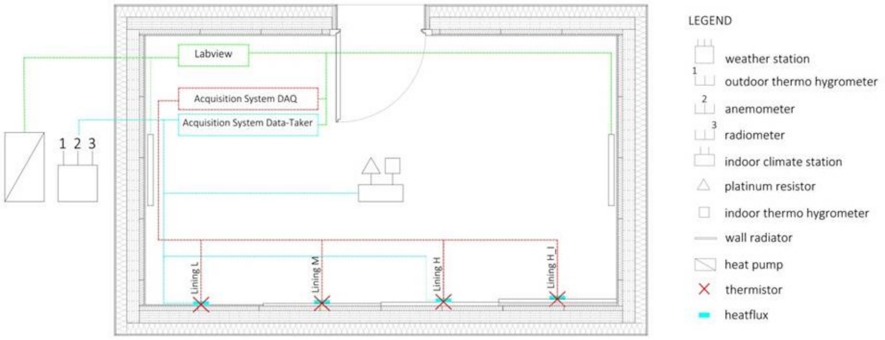

Figure 3.10: Monitoring setup and control system inside the test room.

Table 3.9: Sensor details.

Measure	Sensor Type	Position	Accuracy	Range
Outdoor climate conditions				
Air temperature	Thermo hygrometer	Weather station	±0.2°C	30 ÷ 70°C
Relative humidity	Thermo hygrometer	Weather station	±1.5%	0 ÷ 100 %
Wind direction	Anemometer	Weather station	±2°C	0 ÷ 360°
Wind speed	Anemometer	Weather station	±0.1 ms^{-1}	0 ÷ 60 ms^{-1}
Solar radiation	Radiometer	Weather station	< 5%	30 ÷ 45 V/W/m^2
Indoor climate conditions				
Air temperature	Platinum resistor	centre of the room - h. 140 cm	±0.05°C	200 ÷ 850 °C
Relative humidity	Thermo hygrometer	centre of the room - h. 140 cm	±1.5%	0 ÷ 100 %
Envelope performance				
Heat flow across Lining L	Heatflux	Panel surface - h.140 cm	± 3%	± 2000 W/m^2
Heat flow across Lining M	Heatflux	Panel surface - h.140 cm	± 3%	± 2000 W/m^2
Heat flow across Lining H	Heatflux	Panel surface - h.140 cm	± 3%	± 2000 W/m^2
Heat flow across Lining H_I	Heatflux	Panel surface - h.140 cm	± 3%	± 2000 W/m^2
Lining L surface temperature	Thermistor	Panel surface - h.140 cm	± 0.05°C	200 ÷ 850 °C
Lining M surface temperature	Thermistor	Panel surface - h.140 cm	± 0.05°C	201 ÷ 850 °C
Lining H surface temperature	Thermistor	Panel surface - h.140 cm	± 0.05°C	202 ÷ 850 °C
Lining H_I surface temperature	Thermistor	Panel surface - h.140 cm	± 0.05°C	203 ÷ 850 °C

The air conditioning system consisted of ceiling radiant panels coupled with an outdoor heat pump with inverter. The internal heat gains were instead provided by two electric radiators, installed on the west walls to evenly distribute the heat throughout the mock-up. The energy efficient electric radiators were wall-mounted and white painted, with Carbon Fiber resistance. As it is possible to see in (Fig.3.11), these radiators operate as radiant surfaces and convectively at almost equal quota. The radiators mimic a window on the west orientation. This position excludes direct radiation on the linings under test that are in the inner side of the southern façade. So even if the spectra are remarkably different (electric radiators cover a limited quota of the shortwave range), the convective and longwave radiative effects on the linings could be considered well simulated. Besides, such contribution would have not affect the comparison between the different linings, being invariant in all the testing runs.

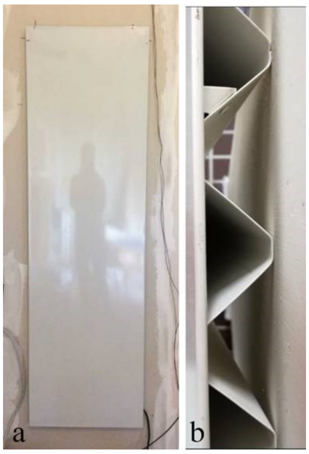

Figure 3.11: (a) Front view of the electric radiator and (b) top view of the tubular section.

As previously mentioned, the test room is windowless and uninhabited, thus both solar and internal heat sources are driven to zero. This peculiar experimental choice allows to fully control the effect of heat gains with bespoke profiles, which come in circumstantially appropriate when further insight into the interrelation among such parameters still needs to be disclosed. Given the paramount role played by the climatic conditions over the results of any experimental methodology, some sort of control strategy had to be implemented in order to homogenize and systematize the outcomes.

First, the use of a test room: some authors confined their studies to component level (wall or roof assemblies [12, 16, 76, 77]), whereas others focused on the whole building and the following variables: solar gains through windows, real life occupancy patterns, variable set points, internal gains from electrical devices, cross ventilation, etc… Although the latter approach depicts more truthfully the dynamics of the energy balance, it introduces a variety of extra parameters including personal ones (occupancy and behavioral patterns), those related to geometry and orientation (of each component and opening), those dictated by local meteorological profiles and those linked to the specific set and tuning of HVACs [13,78]. Generally speaking, the penalty in terms of applicability and repeatability of the whole experiment is fairly significant, since the results, derived for the specific case study, are hard to be transferred to whichever other building typology and climatic context. The adoption of a test room is an in-between solution which retains the complexity of a building without the actual uncontrollability of a real-scale fabric.

The second *escamotage* to extend the validity of the study was the "fabrication" of the indoor gains fluctuations: the internal loads of a residential unit room in summertime were simulated by powering the electric radiators according tailored gains curves. The entire system of sensors and actuators, as well as the dataflow management was demanded to a Virtual Instrument (VI), specifically developed in LabVIEW (programming platform by National Instruments). The gains simulator was incorporated as a stand-alone sub-routine.

Both solar gains and occupancy/equipment loads were contemplated and supplied to the electric radiators. The solar gains curve mimicked the typical variable trend of the heat transmitted through a window, in two periods, one characterized by medium levels of solar radiation, iconic of the average condition, and one much more pronounced, standing for the borderline case with respect to the geographical location of the test room. In detail, the shape of the curves mirrors the experimental profile of a generic medium sized window (1.5 m^2) facing west, respectful of the solar pathway for the given latitude and longitude coordinates. Moreover, this window size is typical of a residential unit in terms of proper artificial lighting (glazed area higher than one-eighth of the floor area). In order to define the amount of total solar transmittance through a westbound glazing surface, the model of the mock-up was reconstructed on Sketch Up, using the Open Studio plug-in (see insert A in Fig.3.12) and a dynamic thermal simulation was carried out with Energy Plus software. The model was calibrated with the monitored outdoor temperatures and solar radiation levels.

Under such real boundary conditions, the curves of the total solar transmittance due to a west-oriented window were obtained through simulations. In particular, we have chosen two levels of heat transmitted through a window in the summer season (Fig.3.12): a medium level, from the typical solar transmittance obtained for cloudy days (Test 1) and a high level, considering the typical solar transmittance on sunny days (Test 2). The relative values were converted in solar gains (W/m^2) and adopted as heat to supply. The loads generation was chrono-programmed to portray the time trends in (Fig.3.13a). The simulated internal and solar gains converged into an add node for later normalization over the nominal power supplied by the electric radiators.

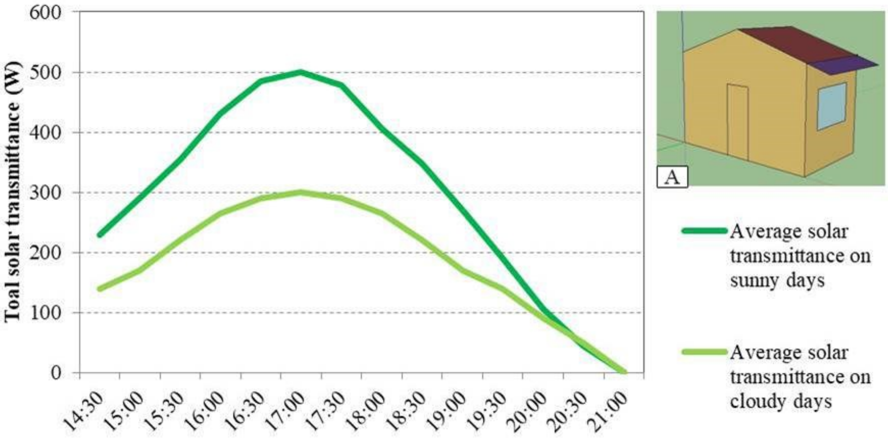

Figure 3.12: Average simulated total solar transmittance passing through the west window of the mock-up on summer season.

The resultant value was eventually multiplied by the output range (in Volts) and fed to the static relé that governed the amount of current running through the electric resistance of the heating units. The internal gains respected the UNI/TS 11300-1 reference values for residential use (see table in Fig.3.13a).

While the radiators were deployed to generate the internal loads, the heat pump served as actual conditioning system, both in cooling and heating mode depending on the season. The consensus to the activation of the heat pump was subjected to an on-off logic, customized on the same VI. The hysteresis was set to 0.15°C as the result of a trial-and-error tuning procedure, aimed at minimizing the indoor temperature fluctuations. The set-points were afferent to the Italian legislation, thus 20°C in winter time and 26°C in summer time. During the monitoring campaign, the following configurations (Fig.3.13b) were characterized:

- Test 1: medium internal loads (occupancy and equipment) and medium solar heat gains, cooling system on;
- Test 2: high internal loads and high solar heat gains, heating system on;
- Test 3: no internal loads or solar gains, heating system on.

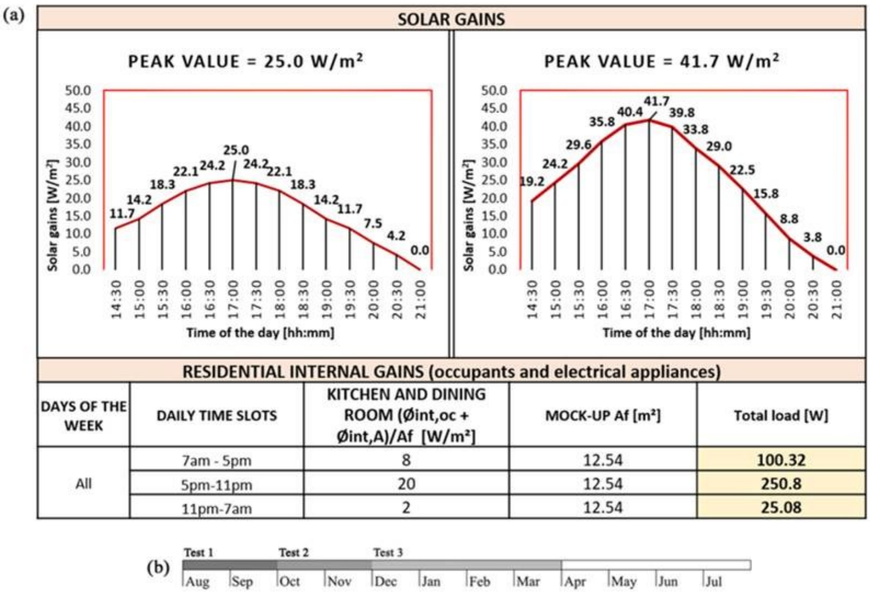

DAYS OF THE WEEK	DAILY TIME SLOTS	KITCHEN AND DINING ROOM (Øint,oc + Øint,A)/Af [W/m²]	MOCK-UP Af [m²]	Total load [W]
All	7am - 5pm	8	12.54	100.32
	5pm-11pm	20	12.54	250.8
	11pm-7am	2	12.54	25.08

Figure 3.13: (a) Internal heat load supplied by the gains simulator and (b) testing timeline.

3.3.2 Evaluation of external linings with different inertia

The monitoring activity was carried out on a yearly basis in order to examine the thermal behavior of the proposed ventilated skins technologies. A proper set of devices was installed for acquiring the following measurements: (Fig.3.14):

- Outdoor temperature, relative humidity, global solar radiation, speed and direction of the wind. Data were collected using a weather station, positioned 3 m away from the ventilated prototypes;
- Surface temperatures of the outermost and innermost layers measured at the bottom (68 cm), at the middle (115 cm) and at the top (168 cm) of each façade. Data were collected adopting thermo-resistance sensors (accuracy ±0.05 °C);
- Incoming and outgoing heat fluxes measured at mid-height (115 cm) in the innermost side of the air chamber. Data were collected through heat flux plates (precision ± 3%);

- Air velocity and air temperature inside the ventilation chamber recorded at mid-height (115 cm). Data were collected using hot-sphere anemometers (tolerance of ±0.03 m/s).

Data acquisition involved gathering analog signals from the probes and digitizing them, by means of NI-DAQ acquisition modules. LabVIEW software was used and implemented for real-time data and elaboration. The sample was set every 5 minutes.

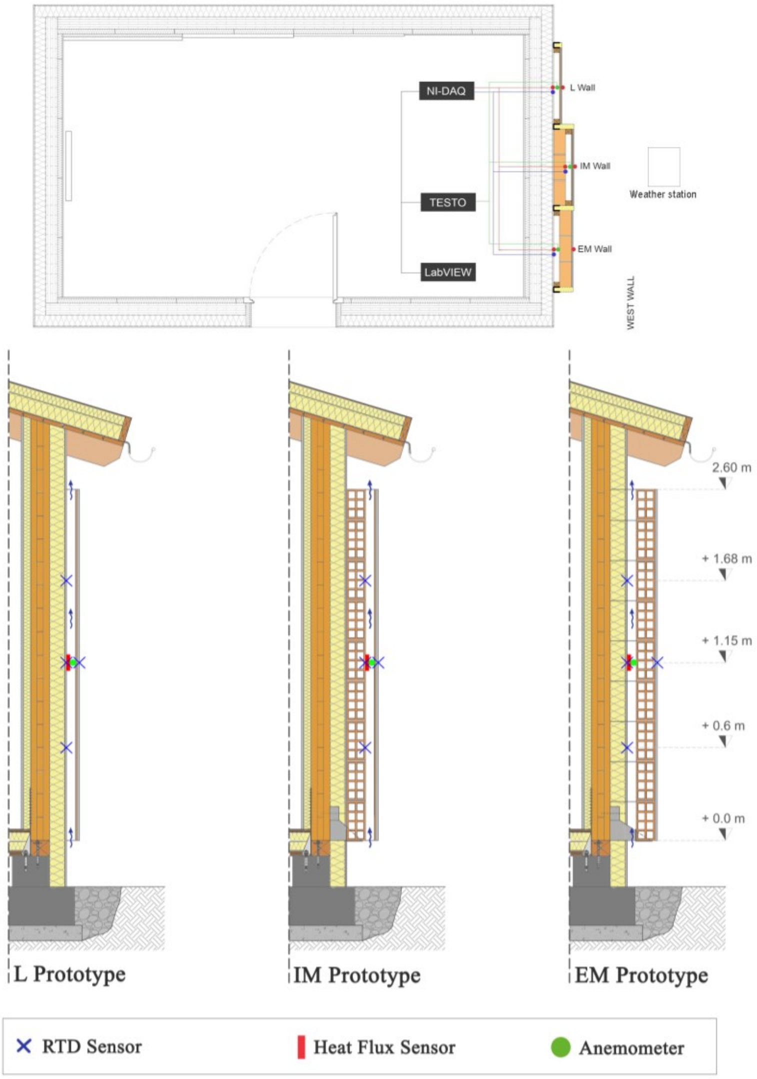

Figure 3.14: Ventilated prototypes monitoring setup.

3.3.3 Evaluation of earth block panel for the mitigation of indoor overheating

The energy experimentation on the earth blocks panel was based on the data collected through a net of previously calibrated probes. The outdoor and indoor microclimate station, mentioned in section 3.3.1, was used to monitor the external and internal boundary conditions of the mock-up. A thermistor and heath flux meter were positioned on the surface of the panel, in line with the center of one of its components (Fig.3.15a). Moreover, in order to get insights into the earth blocks panel inertial behavior, a set of four thermocouples were positioned within the hollows of the same block (Fig.3.15b). The surface temperature and heat flux trends of the earth block (lining EB) were compared with the plasterboard (lining L) and two layers of dry clay panel (lining M).

The entire network of equipment, cooling system and dataflow was demanded to a custom Virtual Instrument (VI), specifically developed in LabVIEW. The acquisition rate was set at 1 minute and the monitoring campaign was carried out during the warmest months. The thermal responsiveness with regard to the summer indoor overheating of the three internal linings was investigated considering the following scenarios:

- Test 1: cooling system switched on (set-point 26°C);
- Test 2: cooling system switched off, free running regime.

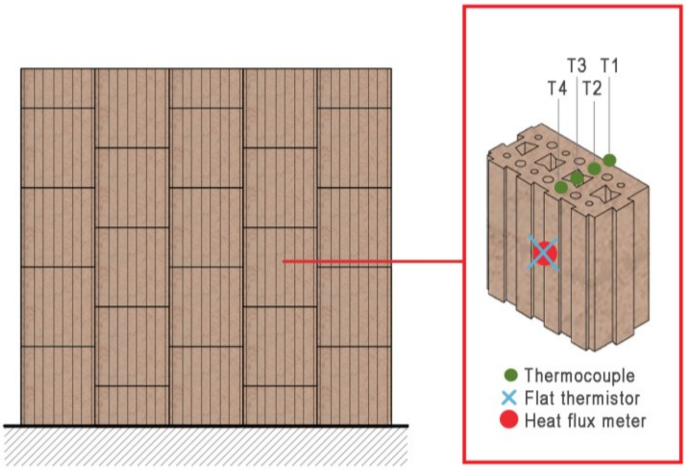

Figure 3.15: Earth block panel monitoring setup and position of the thermocouples inside the block.

3.4 Methods for masonry testing

This sub-section addresses the standards used for characterizing the mechanical behavior of the earth blocks masonry walls and it is divided in three parts: 3.4.1 focuses on the characterization of the unfired clay blocks, 3.4.2 describes the employed DIC technique and 3.4.3. illustrates the procedure for the characterization of the wallettes.

3.4.1 Preliminary characterization of the unbaked clay block

The compressive strength of 9 uncapped earth blocks was determined in accordance to the UNI EN 772-1:2015 standard. The testing apparatus was a hydraulic press machine (maximum load capacity of 5000 kN) showed in (Fig.3.16a). The rate of compression was set at 0.05 (N/mm^2)/s. The earth blocks were tested in the direction in the extrusion direction corresponding to the direction in which they are generally laid.

The initial shear strength parallel to the dovetail joints was determined on 3 specimens according to UNI EN 1052-3:2007 standard (Procedure B). The test set up consisted of two flat stiff plates of 20 mm thickness placed at the top and at the bottom of the specimen (Fig.3.16b). Compressive load was applied on the central plate using of Zwick Roell Z050 testing machine (maximum load of 1000 kN) in force control at a rate of 2645 N/min until failure.

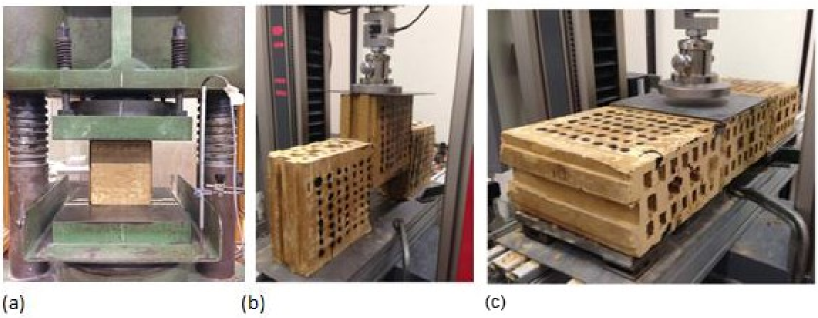

Figure 3.16: Tests set up for the determination of (a) the compressive strength of the earth block, (b) the initial shear strength parallel to the dovetail joints and (c) the initial shear strength perpendicular to the dovetail joints.

The initial shear strength perpendicular to the dovetail joints, subject to an out-of-plane load, was obtained on 3 specimens by adapting the aforementioned procedure, since a specific standard was lacking (Fig.3.16c).

3.4.2 DIC Set-up

A three-dimensional DIC technique was used to obtain data on the masonry mechanical properties and crack maps, taking into account the influence of possible out-of-plane mechanisms on measurements. DIC was applied to all the tests on the wallettes.

This optical measurement system enables the evaluation of deformation phenomena through the evolution in time of a displacement vector. A high-resolution camera records the digital images of the specimen's surface mapped with a speckle texture (Fig.3.17), through which the surface movements will be tracked under the applied load. The set-up is presented in (Fig.3.18). Two Pixelink camera with a 12mm f/1.8 focal lenses (focal length of 12 mm) were mounted at a distance of 2 m from the specimen to monitor its front and back sides (see insert A in Fig.3.18). A third camera recorded the out-of-plane displacements. The region of interest (ROI) was spray-painted with black and white dots, of different dimensions and intensity. During the tests, each manometer was coupled with a high-resolution camera that acquired the frames needed to register the pressure trend against time. Pressure drops, and friction phenomena were neglected. Then, compression and tensile resistance values were obtained, according to the relative test standards. Obtained data were elaborated with MATLAB. The coordinates (x,y,z) of a single point in the tridimensional space of the scene uniquely corresponds to a pixel of the image. Then, the specimen image at the initial state was compared with those acquired through the test as to obtain the normal and shear strains of the whole strain field of the wallettes.

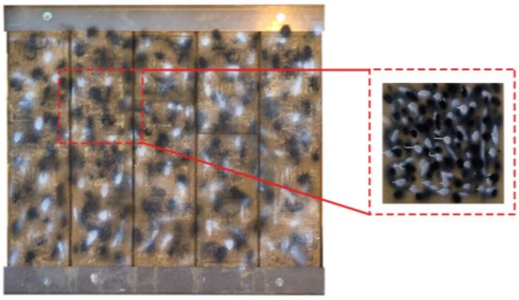

Figure 3.17: Zooming of the spray-painted speckle texture.

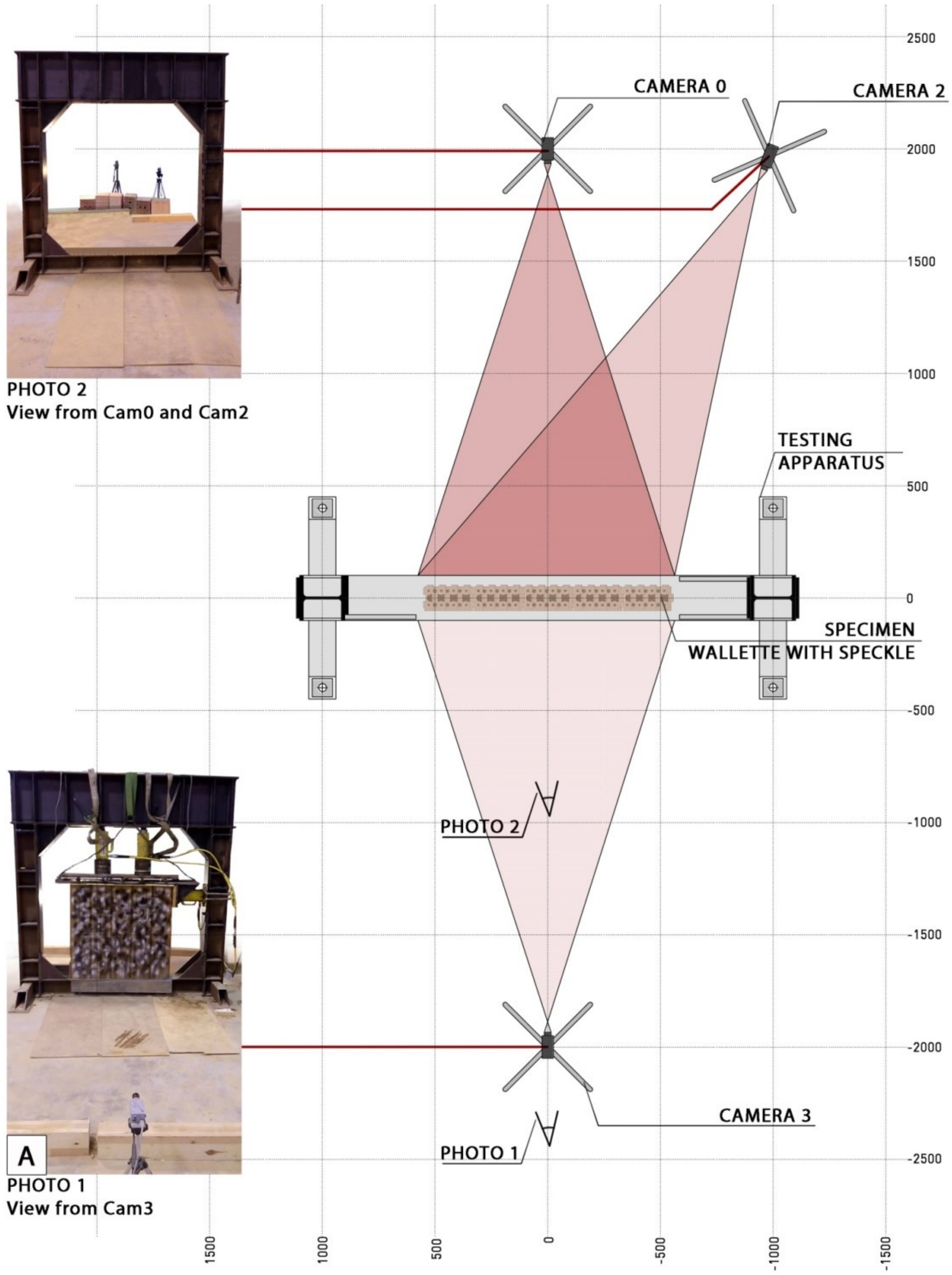

Figure 3.18: DIC set up.

3.4.3 Determination of the compressive and tensile strengths of the earth wallettes

The compressive strength of earth wallettes was determined on 3 samples according to UNI EN 1052-1. The specimens were subject to a compression force by means of two 500 kN hydraulic jacks, uniformly distributed thanks to a 25 mm-thick steel plate (Fig.3.19a). The strain γ_{xy} were obtained by averaging the strain values recorded through DIC on the whole specimen area.

The shear strength of earth wallettes was obtained through diagonal compression tests on 9 samples following the ASTM E519 – 07 standards. The shear test apparatus consisted of a single hydraulic jack (500 kN) (Fig.3.19b). The shear strain γ was obtained through DIC, as the mean γ recorded on the ROI.

The shear strength of earth wallettes under a constant pre-compression load was obtained on 6 samples following the experimental guidelines provided by [87]. Two set of shear tests with different pre-compression load were carried out: 0.2 N/mm^2 and 0.4 N/mm^2. A steel plate (1107 x 120 x 40 mm^3) was welded to the bottom part of the contrast frame, in order to block the possible slide of the specimen during the test (Fig.3.19c). An “L” shaped steel profile was placed on the upper part of the specimen to transmit the horizontal force. Then, a further rectangular steel plate (1275 × 275 × 25 mm^3) was placed over the L shaped one. Between them, four metal cylinders were inserted, to allow a slider between the two plates and to maintain the compression load vertical and to transmit the compression force possibly by friction.

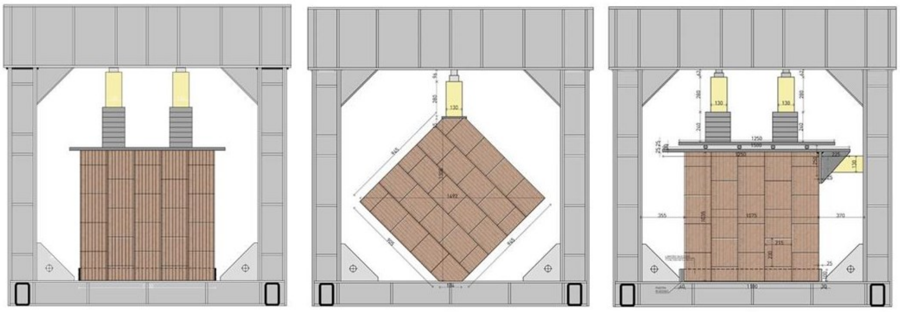

(a) (b) (c)

Figure 3.19: Tests set up of the wallette specimen for the determination of its (a) compressive strength, (b) its tensile strength and (c) its shear strength with a constant compression load.

Chapter 4

Thermal optimization of a CLT wall

This chapter illustrates the experimental results of the thermal behavior of internal (4.1) and external linings (4.2) with different inertial features. Their thermal performance was analyzed using data collected from the annual monitoring on the case study in different seasons and operation conditions.

4.1 Experimentation on internal linings

Results of thermal monitoring experiments are presented for representative periods of the different seasons investigated: summer, autumn and winter.

4.1.1 Outdoor conditions

Outdoor boundary conditions, namely solar radiation and outdoor temperature for all the selected periods, are displayed in (Fig.4.1). Over the representative days of Test 1, the outdoor temperature peaked at 31.2°C and 17.8°C during daytime and nighttime respectively, maintaining an average of 23.8°C, whereas during the intermediate period (October, Test 2) the daily outdoor mean temperature was 11.9°C, with an absolute maximum of 17.5°C and a minimum of 7.1°C. In the coldest period (December, Test 3), the daily outdoor mean temperature dropped down to 7.9°C, with fluctuations between a diurnal peak of 16.2°C and an overnight peak of 4°C.

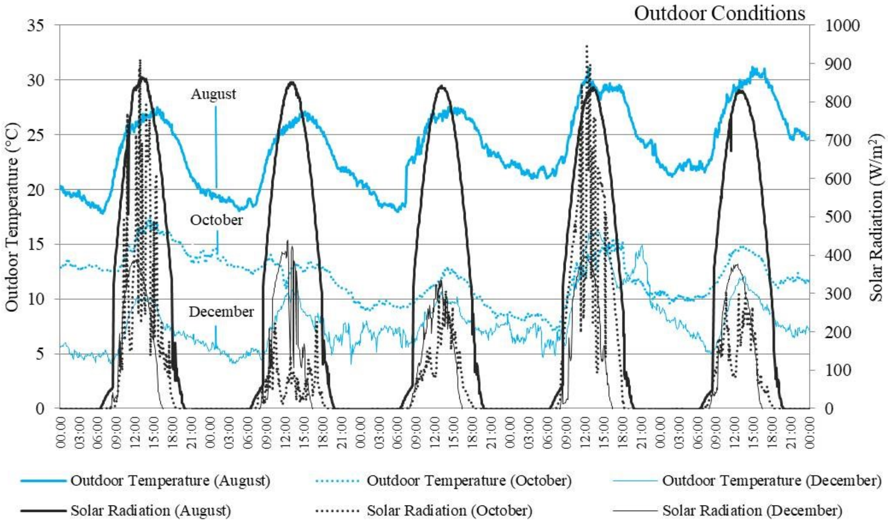

Figure 4.1: Outdoor temperature and solar radiation in the selected periods of August, October and December.

4.1.2 Thermal behavior of internal linings with the same decrement factor but different internal areal heat capacity

During the warmest season, when the test room was under medium thermal stress (Test 1), the internal surface temperatures of both linings varied between 25.9°C and 28.2°C. As expected, Lining M showed milder thermal fluctuations than lining L, with lower surface temperature values during the day and higher values at night (Fig.4.2). As displayed in fig.8b, in the morning and the afternoon, the thermal heat wave was alternatively incoming and outgoing, without a prevailing direction. In the evening (15:00-21:00), lining M stored more heat (positive heat fluxes) with no significant rise in terms of surface temperature. By contrast, the surface temperature of lining L grew noticeably, reaching its high. This demonstrated the expected result that medium-thermal-capacity envelopes could delay and mitigate the peak temperature on the wall surface. Thereafter, at night (21:00-07:00), the heat accumulated throughout the day was released inside the test room: the surface cooled down, with a sudden drop for lining L, and a more attenuated trend for lining M. The less pronounced reaction of lining M to whichever excitation, would determine a more stable operative temperature, which is key factor to achieve thermal comfort and cap out the energy consumption.

Analogous results for Test 2 are shown in (Fig.4.3). At increased solar gains, both linings reached higher surface temperatures than those recorded in the previous run, yet lining M stayed cooler throughout the day, reporting a daily mean surface temperature about 1°C lower than lining L (Fig.4.3a). The peak value fell within the evening hours in both cases.

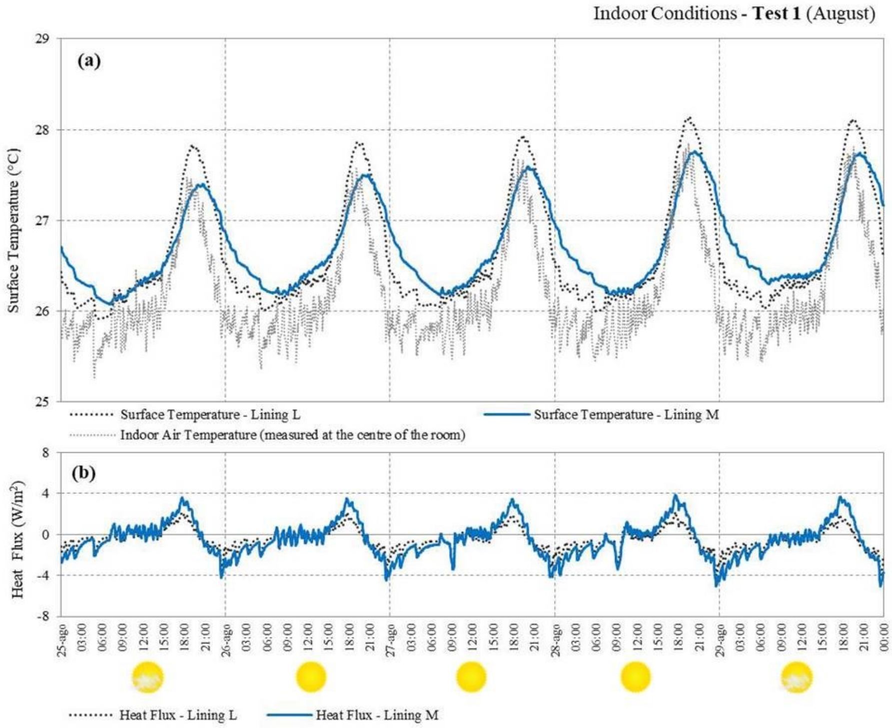

Figure 4.2: Indoor climatic conditions of Linings L (f =0.076, κ_1=12 kJ/m^{2}K) and M (f =0.072, κ_1=33 kJ/m^{2}K) registered in August: surface temperatures and indoor air temperature (a) and heat fluxes (b).

The heat fluxes, measured by the flux meters on the surface of the linings, are displayed in (Fig.4.3b). It can be plainly viewed that the thermal transfer was no more evenly distributed between ingoing and outgoing fluxes, but rather skewed towards the positive side of the plot: the greater amount of supplied solar gains frequently saturated the capacity of the thermal mass to equalize the heat transfer throughout the day and dramatically impinged on the air temperature inside. Comparatively speaking, there was a significant increase of the heat accumulated by Lining M, with respect to the previous scenario. After 23:00, the graph shows an inversion of the thermal fluxes through the wall for both linings, followed by a reduction of their surface temperatures. However, Lining M dropped its temperature at a slower rate than Lining L even if it released more heat inside the test room.

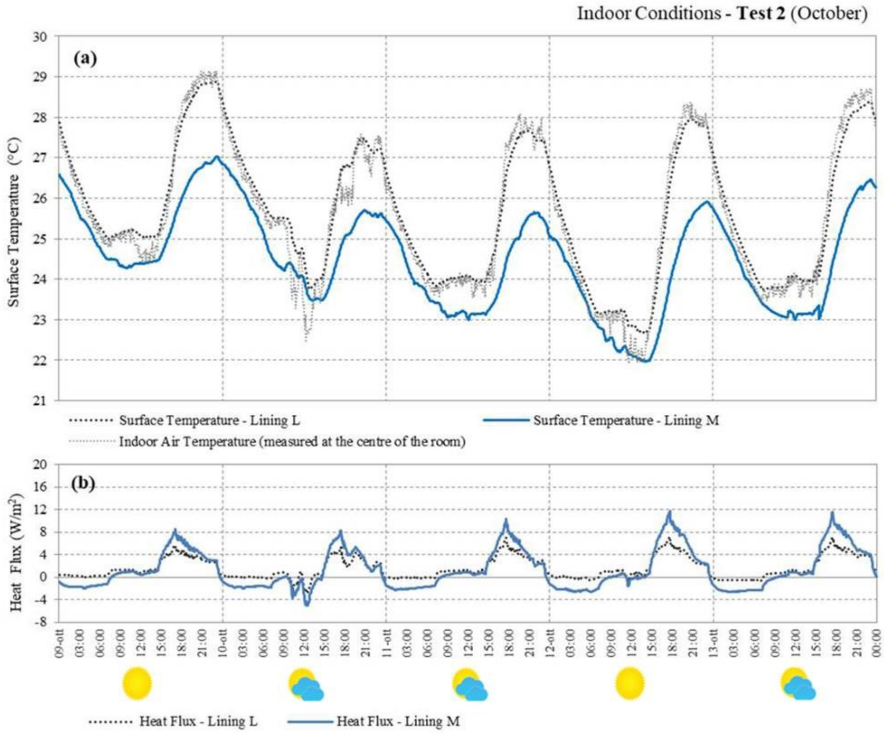

Figure 4.3: Indoor climatic conditions of Linings L (f =0.076, κ_1=12 kJ/m^{2}K) and M (f =0.072, κ_1=33 kJ/m^{2}K) registered in October: surface temperatures and indoor air temperature (a) and heat fluxes (b).

In the winter season (Test 3), the mean surface temperature of Lining M overtook that of Lining L by about 0.5°C (Fig.4.4a). Both internal linings stored the heat from the indoors when the heating system was switched on (positive fluxes) and thus their surface temperature increased. When the heaters turned off, the heat flux inverted, and the accumulated energy flowed inwards with subsequent cooling of the outmost layers (Fig.4.4b).

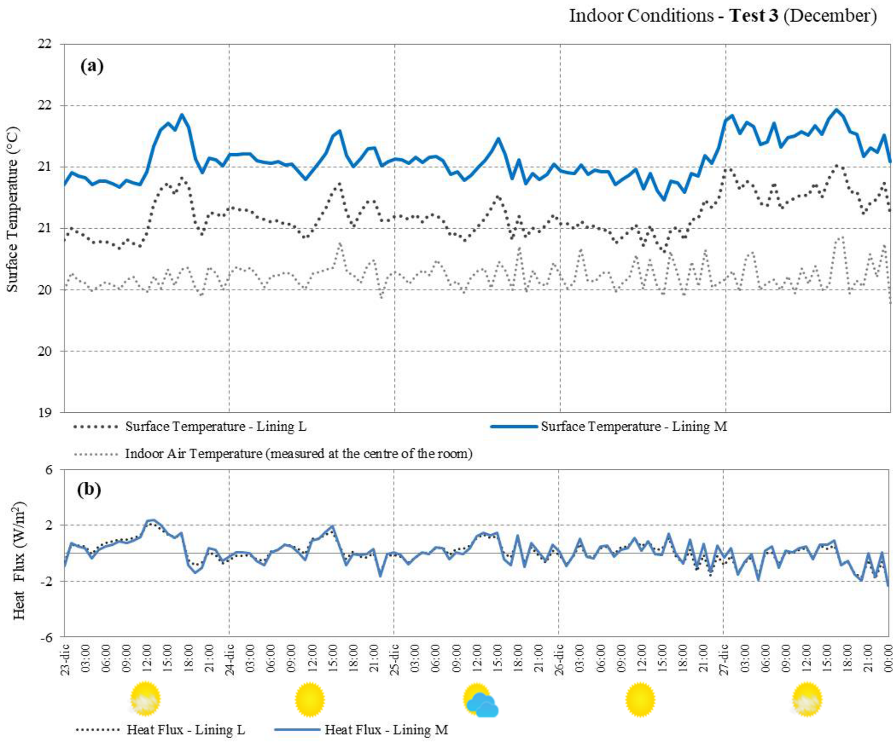

Figure 4.4: Indoor climatic conditions of Linings L (f =0.076, κ_1=12 kJ/m^{2}K) and M (f =0.072, κ_1=33 kJ/m^{2}K) registered in December: surface temperatures and indoor air temperature (a) and heat fluxes (b).

4.1.3 Thermal behavior of inner linings with same internal areal heat capacity but different decrement factor

The graph in (Fig.4.5a) compares the surface temperatures of M, H and H_I linings when the indoor environment was influenced by Test 1 settings. H and H_I linings followed a fairly similar trend during the day (notably between 10:00 and 15:00) and peaked at around the same value (28.4°C and 28.3°C respectively). Conversely, at nighttime, the curves differed: lining H_I dropped its temperature with a rather symmetric shape, compared to the rising counterpart, while lining H attenuated its decreasing rate, following a relatively flatter trend. What is quite unexpected is that lining M still exhibited the lowest surface temperature, over day and night. It stayed at 26.7 °C on average, with a minimum of 26.1 °C and a maximum of 27.6 °C.

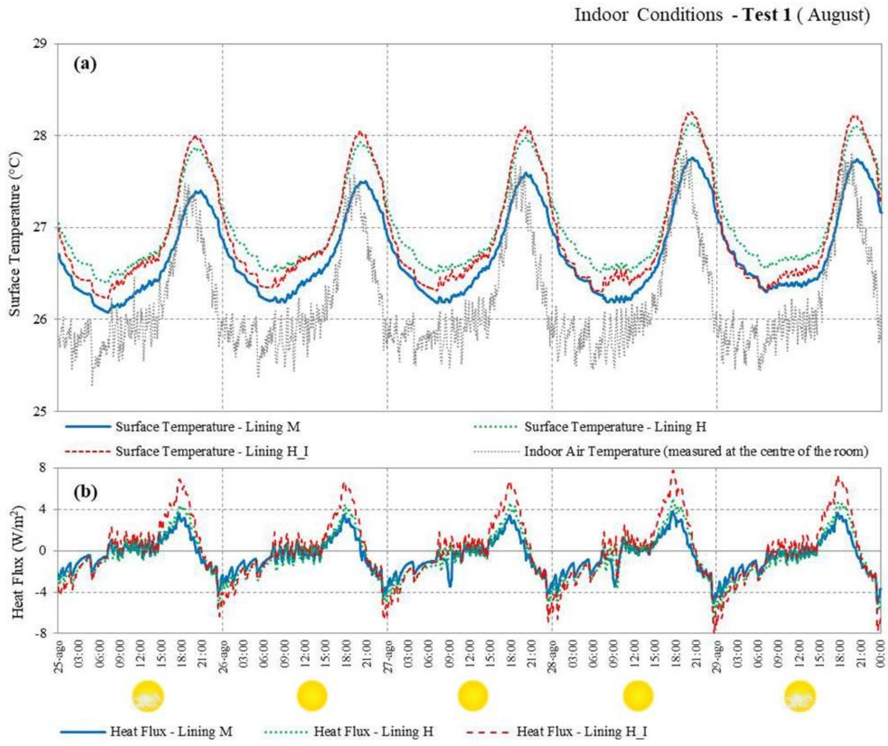

Figure 4.5: Indoor climatic conditions of Linings M (f =0.072, κ_1=33 kJ/m^{2}K), H (f =0.065, κ_1=44 kJ/m^{2}K) and H_I (f =0.047, κ_1=47 kJ/m^{2}K) measured in August: surface temperatures and indoor air temperature (a) and heat fluxes (b).

It is worth noticing that lining H followed the exact same trend of lining M, keeping the reciprocal offset at a rather constant value of 2.7 °C. Contrarily, the gap between lining M and lining H_I is driven to zero and even mildly reversed between midnight and 7a.m., when, concomitantly the heat flux through the lining H_I sudden plummeted. This suggests that the interposition of an extra insulation layer behind the internal lining facilitates the heat release in the indoor environment (as apparent from the highest fluxes at stakes too) by blocking a deeper penetration of the heat wave thus hindering the storage in the core.

The thermal fluxes through the envelopes pursued the same trend previously described in (Fig.4.5b): H and H_I linings, with their major storing capacity (higher κ_1 value) accentuated the major crests and troughs (and thereby emphasized the flywheel effect), while the discrepancy narrowed down during the morning and the early afternoon.

Indeed, the very low f value determined that the heat wave coming from the inside was strongly attenuated. The absorbed quota was then re-emitted inside causing overheating.

In Test 2 (Fig.4.6a), the inner linings were subjected to higher internal loads during the day when the simulator supplied both occupants and solar gains, hence the surface temperatures of the three linings reached higher maximum peaks, with respect to the previous scenario. On the other hand, the colder air outside determined the lower minimum values as well, particularly over the night.

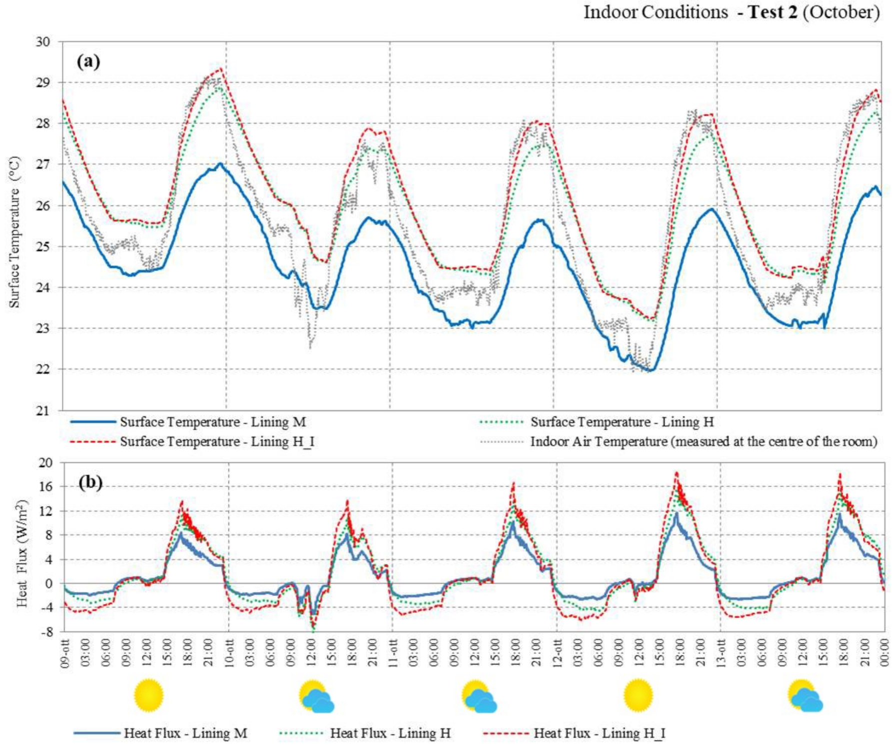

Figure 4.6: Indoor climatic conditions of Linings M (f =0.072, κ_1=33 kJ/m^{2}K),H (f =0.065, κ_1=44 kJ/m^{2}K) and H_I (f =0.047, κ_1=47 kJ/m^{2}K) registered in October: surface temperatures and indoor air temperature (a) and heat fluxes (b).

What emerges from the time trends in (Fig.4.6a), is that H and H_I linings' fluctuations almost overlapped during nocturnal hours, while the diurnal difference hit a high of 0.5°C. When the comparison is extended to the medium capacity lining too, the gap gets emphasized: H and H_I linings recorded surface temperatures about 1.5°C above M's. The thermal exchange through the envelopes is portrayed in (Fig.4.6b). Again, the balance between positive and negative heat flows is jeopardized, with a sizeable dominance of the released quota. The highest amount of stored heat is achieved by lining H_I, followed by linings H and M.

(Fig.4.7a) reports the winter indoor environment conditions of the test room (Test 3), with surface temperatures oscillating between a maximum peak of 21.5°C and a minimum one of 20.7°C.

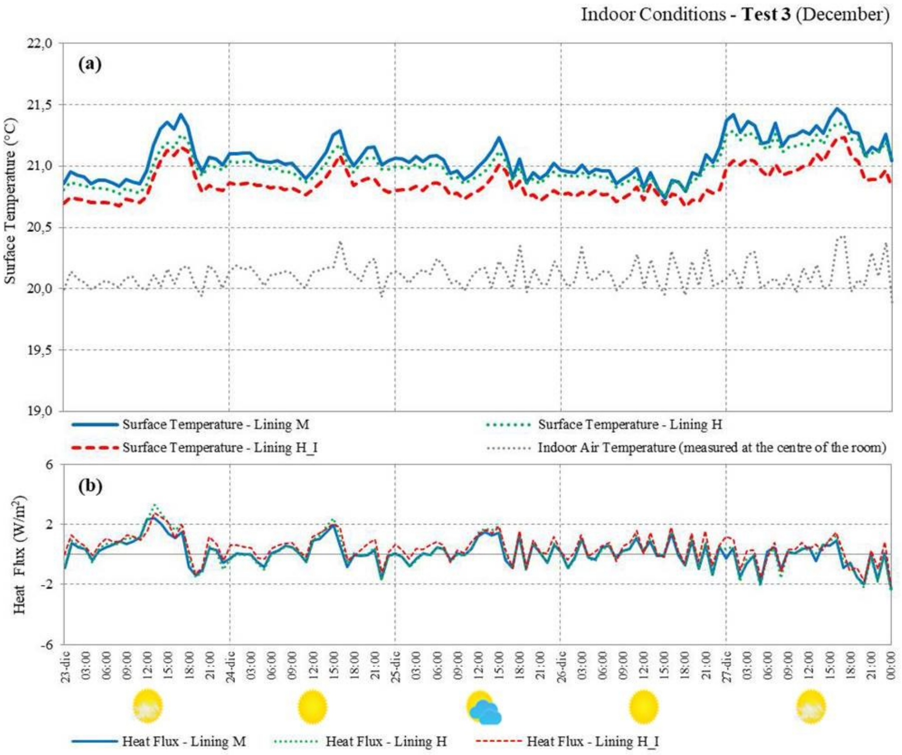

Figure 4.7: Indoor climatic conditions of Linings M (f =0.072, κ_1=33 kJ/m^{2}K), H (f =0.065, κ_1=44 kJ/m^{2}K) and H_I (f =0.047, κ_1=47 kJ/m^{2}K) registered in December: surface temperatures and indoor air temperature (a) and heat fluxes (b).

As for linings L and M, the heat transfer is mostly dictated by the on-off cycle of the heating system: during the day, when the heating was operative, the fluctuations of both surface temperature and heat flux were much more nervous than those recorded with the systems switched off. The distribution of outgoing and ingoing heat flows was still unbalanced (see Fig.4.7b), swinging between a negative average of -2 W/m^2 and a positive average of +3.3 W/m^2. In this Test, linings M and H did not substantially differ in terms of surface temperatures, staying on a mean value of about 21.07°C, while the addiction of internal insulation (Lining H_I) led to the lowest mean surface temperatures (around 20.8°C) throughout the day.

4.1.4 Discussion

In order to gain insight into the flywheel effect, for each test period, the thermal flux dataset of the sunniest day was elaborated into clustered columns (Fig.4.8-4.10) to comparatively visualize the energy per unit of surface (Wh/m^2) exchanged by the four lining samples with the indoors, hour per hour. It should be stressed here that nearly-zero values were strongly affected by the instrument sensitivity and were thereby disregarded in the analysis.

First, by looking at the y axis scale, it is plainly visible that the amount of energy going back and forth the internal lining was deeply influenced by the magnitude of internal loads (Test 2>Test1>Test3).

Second, the ranking in order of decreasing energy transfer goes with the κ_1 value: lining H_I come substantially on the top/bottom of the clustered columns for the most of the time, followed by lining H, lining M and lining L. It means that higher areal heat capacity factually mirrors in higher amount of energy stored and released by the component, yet this does not imply surface temperature equalization.

Third, the charge-discharge behavior is utterly different as the boundary conditions change:

- in August (Fig.4.8), the positive side of the chart is quite balanced with the negative counterpart, irrespective of the massive lining in object. Lining L is the only one that rejects heat into the indoor environment over the peak hours. All the others maintain an accumulative behavior. Lining M tends to discharge more (compared to the other massive components) in the morning (8:00-10:00) and in the evening (21:00-22:00). This might explain the strongest compensation of the surface temperature swings;
- in October (Fig.4.9), the overnight heat transfer is radically different from that recorded in summertime: the released heat does not counterbalance the stored quota and the peak values shift forwards by approximately 3 hours. This is the result of the new set of triggers at stake: heating system on instead of the cooling one, high internal loads instead of the medium ones. As a matter of fact, the overabundance of heat sources, despite the colder outdoor conditions, delayed the trend reversal and thus offset the energy balance towards the storage rather than the release. Comparatively speaking, the gap

between lining H and lining H_I narrowed down, in alignment with the analysis on the surface temperature;

- In December (Fig.4.10), when the internal load generation was disabled, and the heating system moderated the indoor environment, the heat transfer through the four linings apparently responded to the simultaneous activation of the air conditioning: consequently, a typical sinusoidal pattern is not recognizable. Sharp deviations or trend reversals were recorded over hourly time spans. Lining H_I accentuated the stored component, as happened during Test 1 and Test 2, but not the released component, which in turn, was generally higher with lining L. This difference might explain why the surface temperature got more smoothed with lining H_I in this case only. Conversely, the gap between lining M and H shrank.

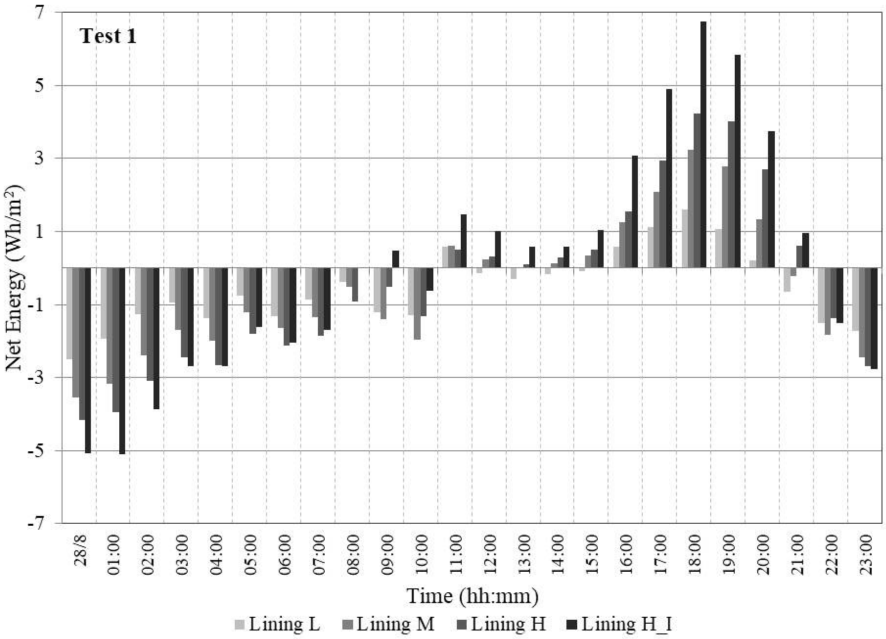

Figure 4.8: Energy per unit of surface exchanged in August 28 (Test 1).

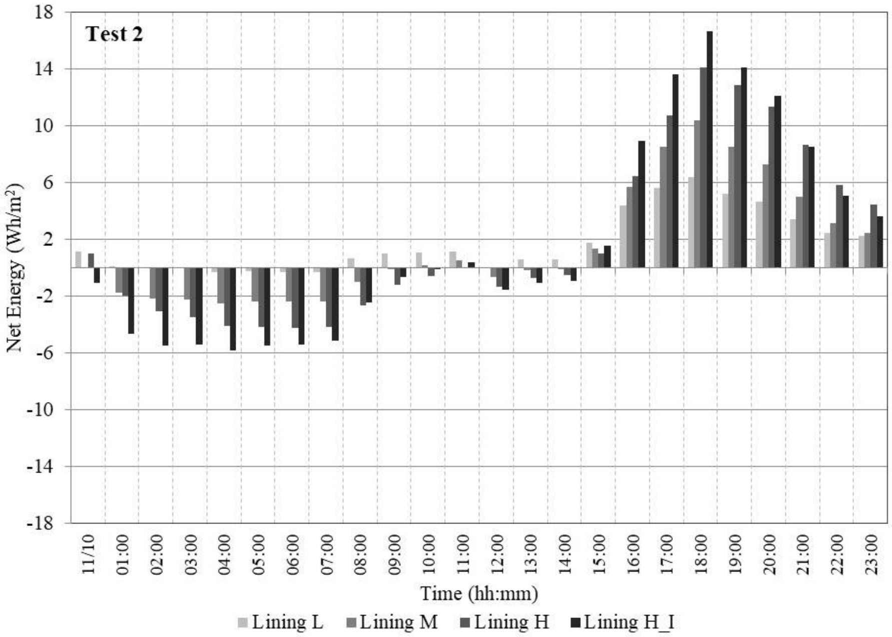

Figure 4.9: Energy per unit of surface exchanged in October 12 (Test 2).

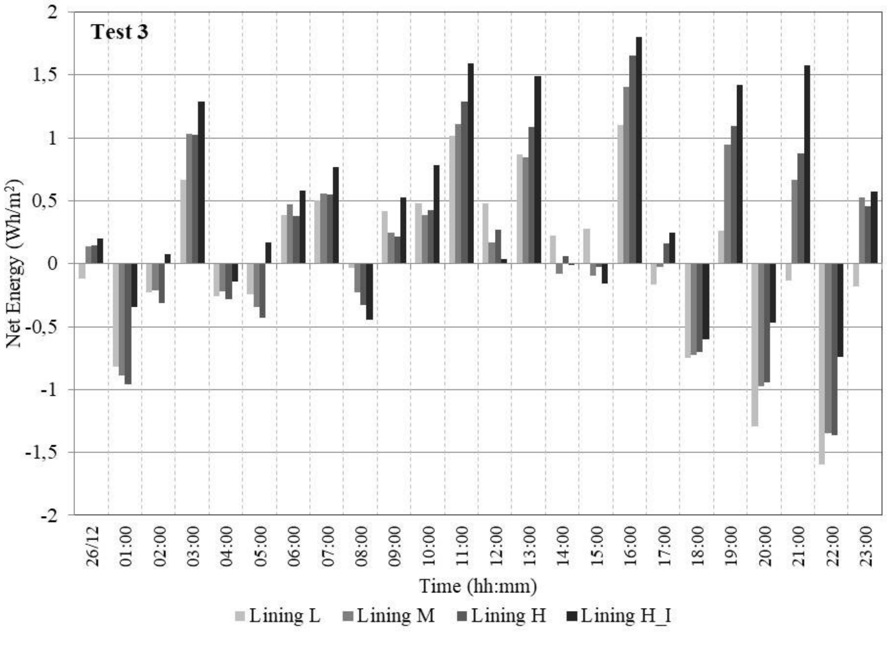

Figure 4.10: Energy per unit of surface exchanged in December 26 (Test 3).

4.2 Experimentation on ventilated skins

Results of thermal monitoring experiments are presented for representative periods of the different season investigated: summer and winter.

4.2.1 Summer mitigation potential on the outdoors

The beneficial effect of ventilated solutions with external massive cladding in lowering the outdoor surface temperatures on annual basis was highlighted by Patania et al. [45]. They concluded that such a technique could reduce the external surface temperature down to 10°C in summer with respect to ETICS systems. In this regard, similar results emerged in our study by comparing the obtained surface temperatures of the three ventilated technologies with the one of an ETIC system, recorded in a string without the ventilated layer just in adjacent to the prototypes. The comparison has been plotted for a single summer day, characterized by an outdoor mean temperature of 22 °C, an average daily solar radiation of 510 W/m^2 and a mean wind speed of 1.2 m/s. The addition of a ventilation layer lowers the external surface temperature down to 4 °C in the case of a lightweight external cladding (IM and L walls) and down to 10 °C when a massive external cladding, namely the EM wall, is considered (Fig.4.11).

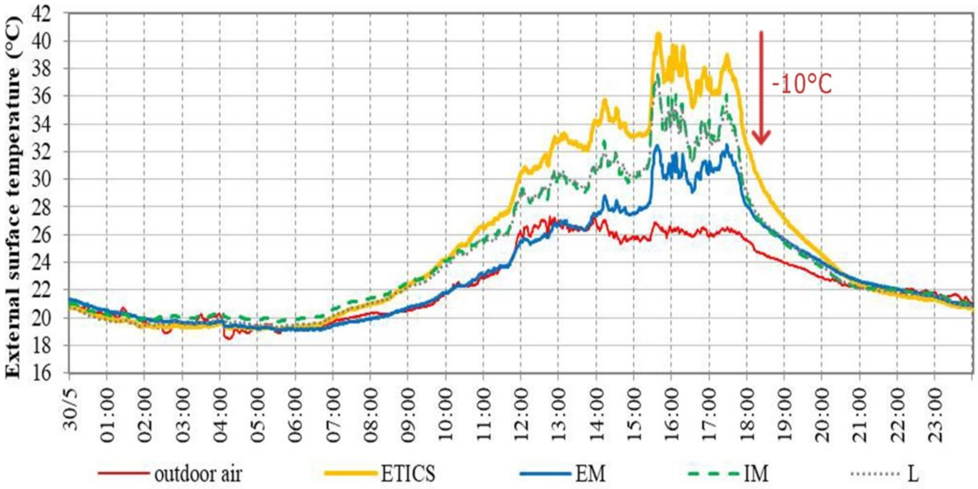

Figure 4.11: External surface temperatures of EM, IM and L prototypes compared with an ETICS system characterized by the same envelope without the ventilation gap, plotted for a single summer day.

4.2.2 Summer behavior of the facades

The present paragraph shows the results from the summer campaign for all the three prototypes. (Fig.4.12) provides an overview of the weather conditions of 5 consecutive days, representative of the typical Mediterranean summer climate. The mean outdoor air stayed at about 22 °C. During the day, the outside temperature swung between 20 °C and 28 °C whereas during the night, the temperature averagely varied between 17 °C and 23 °C. The maximum solar radiation was around 870 W/m^2. Overnight, the wind speed was nearly absent while the diurnal average was around 1.6 m/s, with a prevalent north direction.

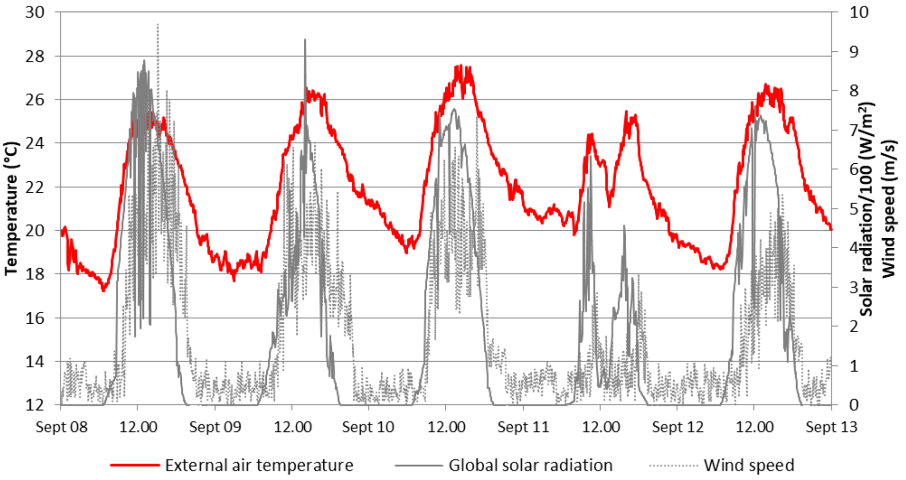

Figure 4.12: A selection of monitored summer outdoor environmental conditions (external air temperature, global solar radiation and wind speed).

The external surface temperatures profiles are plotted in (Fig.4.13). As expected, the temperatures (recorded at 115 cm from the inlet) were always significantly higher than the outdoor one. Moreover, when the solar radiation hit the west-side facades in the time slot (14:00 – 18:00), the values notably increased, with an average offset of 7 °C. However, the maximum values recorded by day differed for the three walls, since they were influenced by the presence of the mass. IM and L facades, designed with the same outer cladding (white shaved OSB panel), reported similar external surface temperature trends, reaching the highest values. Conversely, EM facade, characterized by a massive cladding, showed daily external surface peaks temperature almost 2 °C lower (September 12th) over peak hours than L. All the surface temperature collapsed suddenly when there was no solar radiation with surface temperatures staying almost 1 °C lower than the outdoor air during the night. Noticeably, by night, the surface temperature profiles were almost equal (00:00-07:00) for the three configurations. The EM solution exhibited the minimum peak since the outer mass released the daily stored heat, thus experiencing more prominent cooling. In the morning hours, the outer mass slowly began charging, with the EM wall increasing gradually its external surface temperature (lowest steepness in the morning ascending part among the three tested options). Therefore, the EM façade was able to keep its surface temperature around 1.5 °C lower than the outdoor temperature.

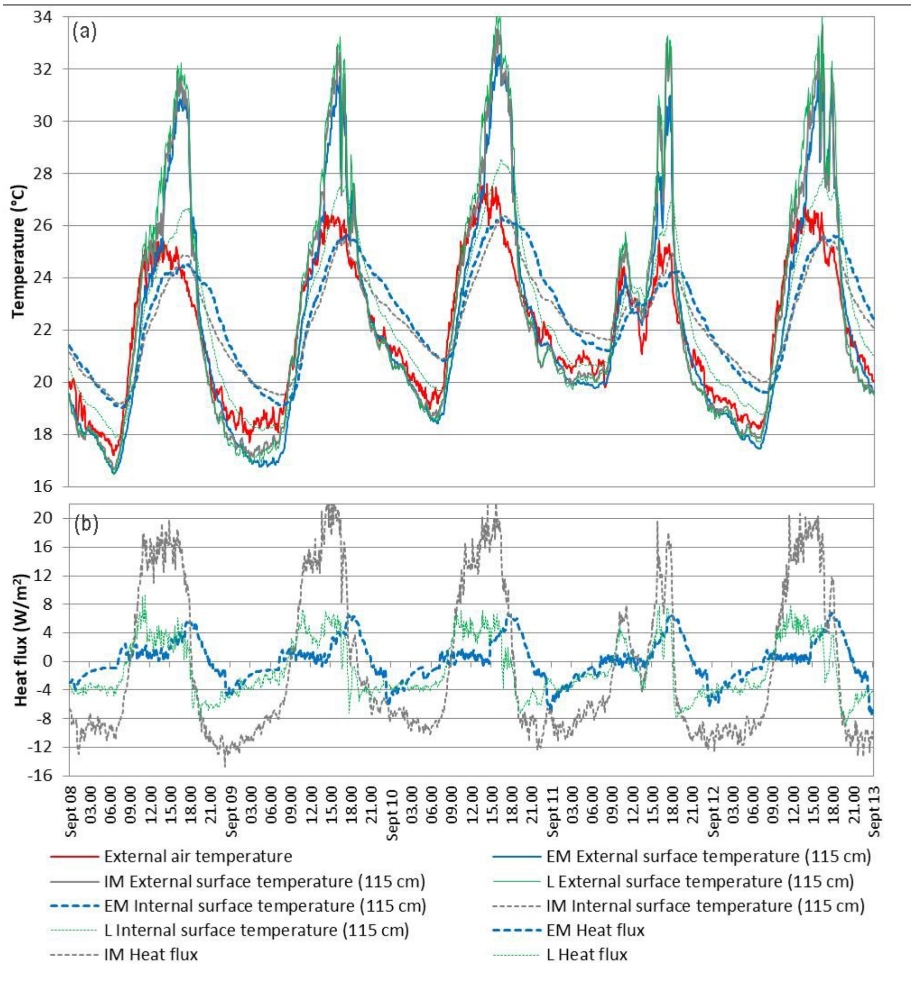

Figure 4.13: Summer thermal profiles of the (a) external air, the external and internal surface temperatures and (b) health fluxes of the three prototypes.

(Fig.4.13a) also reports the surface temperatures measured on the innermost side of the cavity at mid-height (115 cm from the inlet) for the three walls. The L wall went through the greatest thermal range, reaching the maximum daytime values (exceeding the ones of the outdoor air when the sun hit the façade) and the minimum ones by night (very close to the outdoor air when the solar radiation was absent or low). By contrast, EM and IM internal surface temperatures showed milder fluctuations with respect to the lightweight solution (L). This stems from the presence of massive bricks in the EM and IM walls air cavities (although in different positions), that directly impacts on the temperatures in the innermost side of the air gap. However, the mass positioned on the outer side of the gap registered the lowest values round the clock. This means that the EM solution succeeded at dissipating the retained heat in a more effective way with respect to IM by triggering a higher airflow rate within the cavity.

The thermal flux trends for the three walls (recorded at mid-height from the inlet, on the inner side of the air gap), are showed in (Fig.4.13b). The heat fluxes are considered positive with an incoming direction towards the test room. Around peak hours (11:00 – 16:00), the IM prototype reached the highest values, compared to those recorded by the EM and L ones. This can be explained by the fact that, only for the IM wall, the heat flux plate measures the storing action, since it was placed directly on the hollow bricks surface. The L wall heat flow always moved inwards during the day. By contrast, the heat flux of the EM wall was almost close to zero in the morning and increased its value later in the afternoon (with an inward direction). The mass positioned on the external side of the air gap operated as a thermal buffer between the outdoors and the ventilation chamber, needing more time before an appreciable thermal gradient occurred on the edge of the air gap to trigger the heat flow. In the evening the heat reversed, being released in the cavity (negative sign). In particular, IM and L walls heat fluxes suddenly dropped with very similar slopes while EM underwent a gradual decrement because of the conservative behavior of the external massive cladding that is less influenced by the external environment variations.

4.2.3 Summer thermal gradient

This section illustrates the data regarding the hourly values of the horizontal trend of the temperatures recorded in the three walls for a single summer day (September 12th). The temperature variation of the outdoors, the outer surface, the air cavity, the innermost side of the gap and the indoors are plotted in (Fig.4.14) for all the three ventilated solutions in the time slot (12:00-17:00). The values recorded at 19:00 (when the solar radiation is very low) are also included for reference. The horizontal temperature profiles were linearized. Moreover, the hourly values of air cavity velocity, global solar radiation and wind speed are given.

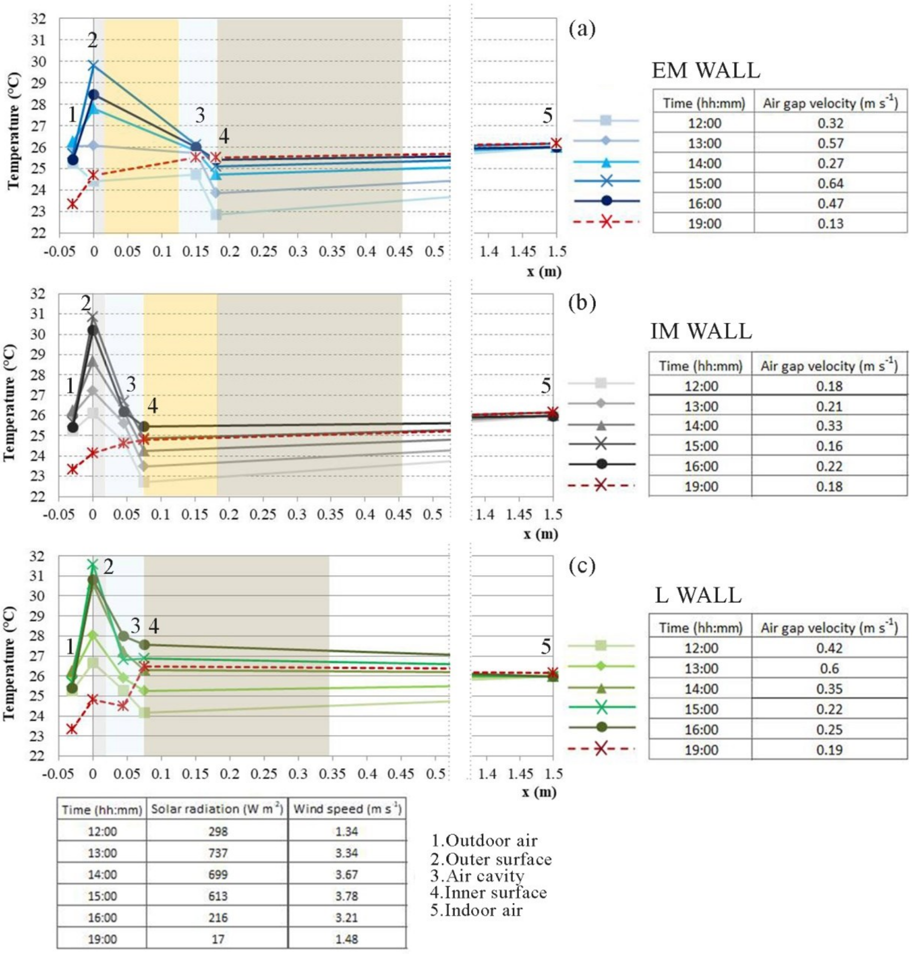

EM WALL

Time (hh:mm)	Air gap velocity (m s^{-1})
12:00	0.32
13:00	0.57
14:00	0.27
15:00	0.64
16:00	0.47
19:00	0.13

IM WALL

Time (hh:mm)	Air gap velocity (m s^{-1})
12:00	0.18
13:00	0.21
14:00	0.33
15:00	0.16
16:00	0.22
19:00	0.18

L WALL

Time (hh:mm)	Air gap velocity (m s^{-1})
12:00	0.42
13:00	0.6
14:00	0.35
15:00	0.22
16:00	0.25
19:00	0.19

Time (hh:mm)	Solar radiation (W m^{-2})	Wind speed (m s^{-1})
12:00	298	1.34
13:00	737	3.34
14:00	699	3.67
15:00	613	3.78
16:00	216	3.21
19:00	17	1.48

Figure 4.14: Trends of the average values of the temperatures across (a) EM, (b) IM and (c) L facades plotted for different hours in a summer day (September 12th).

The maximum peak on the outer skin is recorded at 15:00 for all the facades (Fig.4.14 a, b, c). It is evident that a gradual increase of the external surface determined an increase of the air gap temperatures. This implies that the thermal gradient between the indoors and outdoors is progressively reduced thus minimizing the heat expulsion through the envelope. Therefore, low air temperatures within the cavity are desirable, as in the case of EM wall (Fig.4.14a). Notably, the hourly gradient between the air gap and inner skin temperatures was the highest for IM wall (Fig.4.14b). Moreover, in the innermost sides, the massive configurations (EM and IM) recorded almost the same temperature range (23°C-25.5°C), with values lower than the indoors ones.

So, in lightweight building structures that offer less thermal resistance to the entire wall, the adoption of a thermal mass in contact with the air gap, although in different position, is found to be beneficial in terms of heat losses towards the outdoors. Conversely, the L façade exhibited the worst thermal behavior since not only it recorded the highest values in the outer and inner surfaces and in within the cavity but also emphasized the heat transfer towards the mock-up (Fig.4.14c).

4.2.4. Winter behavior of the facades

The present section illustrates the results obtained from the winter monitoring campaign. A portray of the outdoor boundary conditions in the coldest months is showed in (Fig.4.15). In this season, the outdoor temperature varied greatly, fluctuating from a minimum of 4°C during the night and a maximum of 16°C during the day. The maximum solar radiation in the sunniest day (December 24th) reached 440 W/m^2. The wind velocity was very low at night (approximately 0.5 m/s). The windiest days were December 23th and 27th characterized by peaks of 5 m/s during the day central hours. The prevalent wind direction was north.

The winter temperature trends of the external cladding surfaces, recorded at mid height (115 cm from the inlet), for EM, IM and L walls is presented in (Fig.4.16a). As for summer, all the temperatures were higher than the outdoor air during the time slot (14:00–17:00) in which the solar radiation hit the westbound facades. The L configuration external surface temperature reached again the highest values, with peaks of approximately 1°C above IM's. The EM wall external surface temperature remained the coolest throughout the day lowering the daily peaks down to 5°C in the warmest day (December 26th). During the nighttime, the outer surface temperatures of the three walls dropped significantly, especially with respect to the summer counterpart. However, it can be pointed out that the outdoor air fluctuations impacted more on the IM and L temperatures trends.

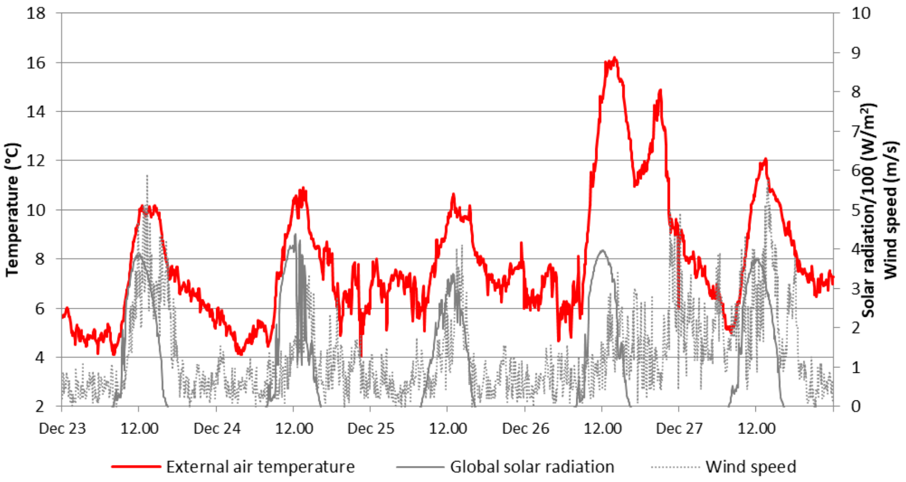

Figure 4.15: A selection of the monitored winter outdoor environmental conditions.

Conversely, the EM configuration recorded around 2°C less than the outdoor air since the mass on the outermost side cooled down the most. In the morning hours, this led to a broad difference (around 3°C) between the rising outdoor and EM surface temperatures since the beneficial nighttime cooling was better exploited in the coldest season.

In the coldest months, the temperature profiles recorded on the innermost side of the gap confirmed the summer findings (Fig.4.16a). The air temperature curves within the cavity kept their typical bell-shaped trends, less pronounced for the massive walls (EM and IM), emphasized for the lightweight one (L). Indeed, the L configuration registered the highest daily maximum temperature peaks in the gap (with values increasing to 4°C up with respect to the IM ones). In winter, the IM and L heat flux daily trends were confirmed (Fig.4.16b). EM exhibited again the lowest flux, but the trend followed that of the other walls.

4.2.5 Winter thermal gradient

The hourly values of the temperatures trends across the facades of the three prototypes for a single winter day (December 24th) are presented in (Fig.4.17). The data are given for the afternoon time slot (15:00-19:00), just before and after sunset in order to understand which solutions behaves as an active component with regard to the reduction of the heat losses through the wall. The values recorded at 12:00 (when the solar radiation is very high) are also included for reference. Global solar radiation, wind speed and air cavity velocity are also reported. The EM configuration exhibited the lowest air cavity temperatures (between 7.2-10.5°C), despite the highest airflow rates, due to the presence of a thermal buffer between the outdoors and the air cavity (Fig.4.17a).

Nonetheless, its values at midday on the internal surface (position 4) were slightly higher than IM solution, similar on the rest of the day. The heat transfer towards the outdoor environment was minimized at night. The L wall had higher surface temperatures during the day, reaching higher peaks at 12:00, while after the afternoon, it behaved like the other two walls. It can be concluded that EM and L solutions behaved more efficiently than the IM, especially in terms of heat transfer behavior (Fig.4.17b).

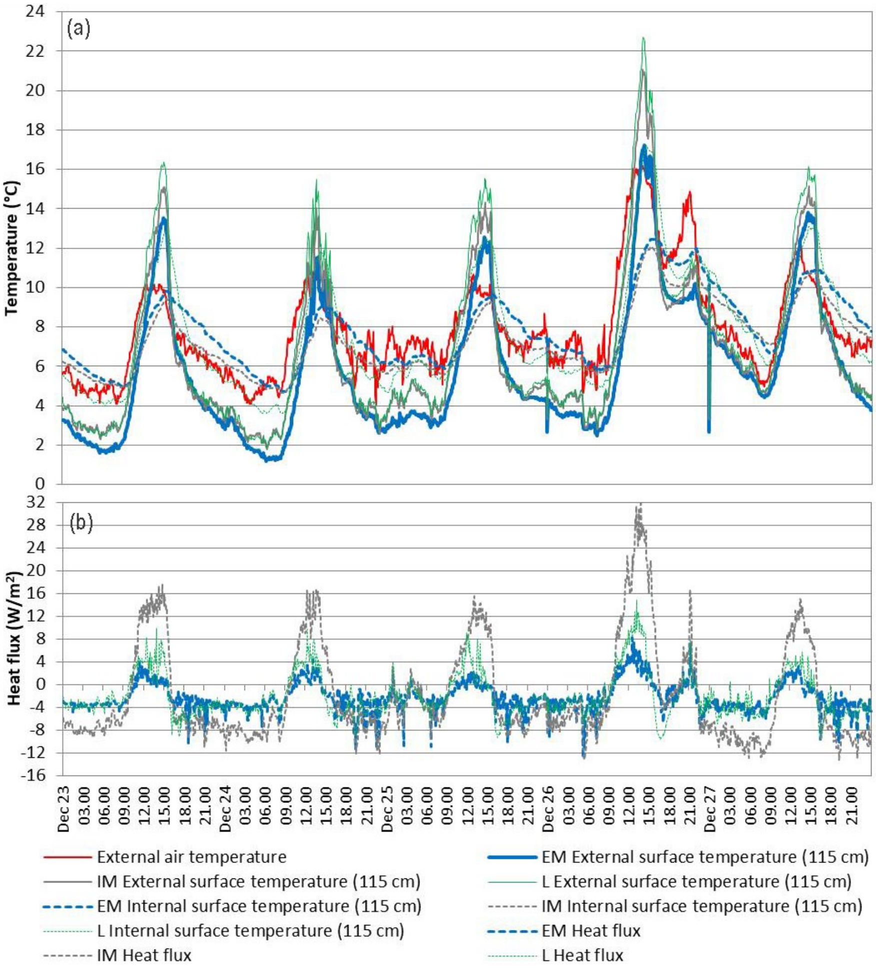

Fig.4.16. Winter thermal profiles of the (a) external air, the external and internal surface temperatures and (b) health fluxes of the three prototypes.

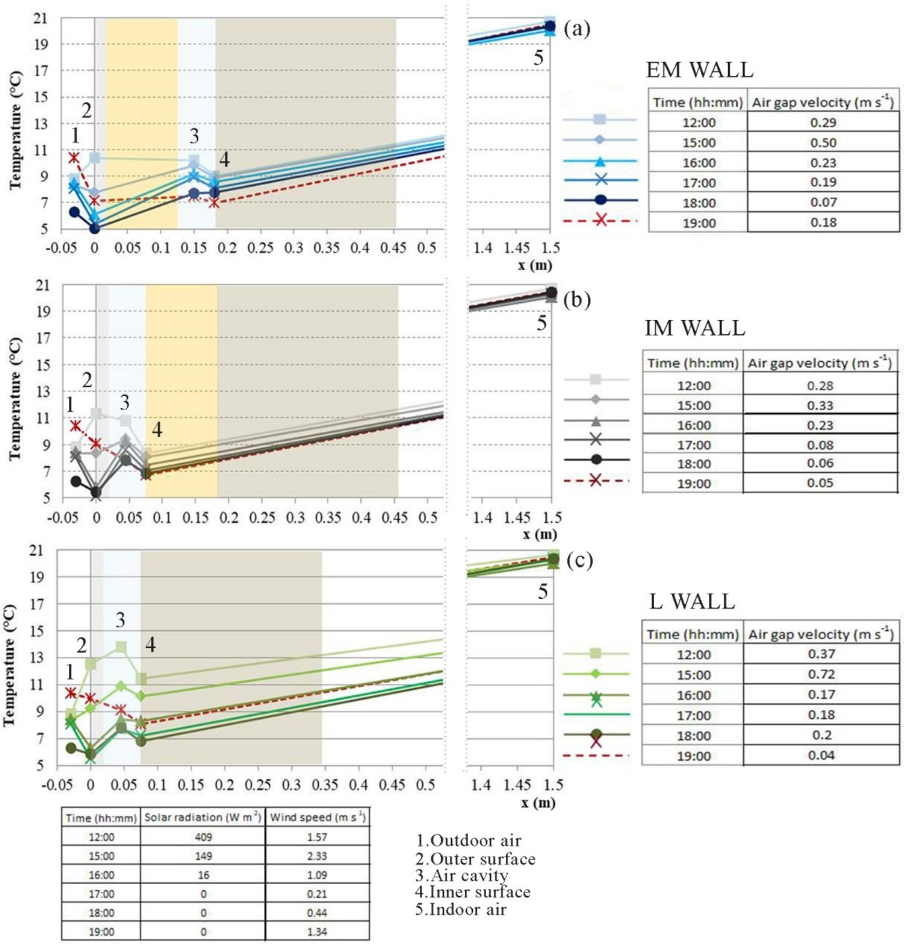

EM WALL

Time (hh:mm)	Air gap velocity (m s^{-1})
12:00	0.29
15:00	0.50
16:00	0.23
17:00	0.19
18:00	0.07
19:00	0.18

IM WALL

Time (hh:mm)	Air gap velocity (m s^{-1})
12:00	0.28
15:00	0.33
16:00	0.23
17:00	0.08
18:00	0.06
19:00	0.05

L WALL

Time (hh:mm)	Air gap velocity (m s^{-1})
12:00	0.37
15:00	0.72
16:00	0.17
17:00	0.18
18:00	0.2
19:00	0.04

Time (hh:mm)	Solar radiation (W m^{-2})	Wind speed (m s^{-1})
12:00	409	1.57
15:00	149	2.33
16:00	16	1.09
17:00	0	0.21
18:00	0	0.44
19:00	0	1.34

Figure 4.17: Trends of the average values of the temperatures across (a) EM, (b) IM and (c) L facades for different hours in winter (December 24th).

4.2.6 Discussion

This section presents the comparison between the airflow behavior of the EM and IM walls since from previous analysis they exhibited the better thermal performance on annual basis.

Impact of the mass position in the airflow rates in summer

The comparison between the air temperatures and air speed within the gap (measured at 115 cm height from the inlet, at the center of the gaps) for the EM and IM walls is plotted in (Fig.4.18) for a single summer day (September 12th, with daily average solar radiation of 400 W/m² and mean wind speed of 1.4 m/s).

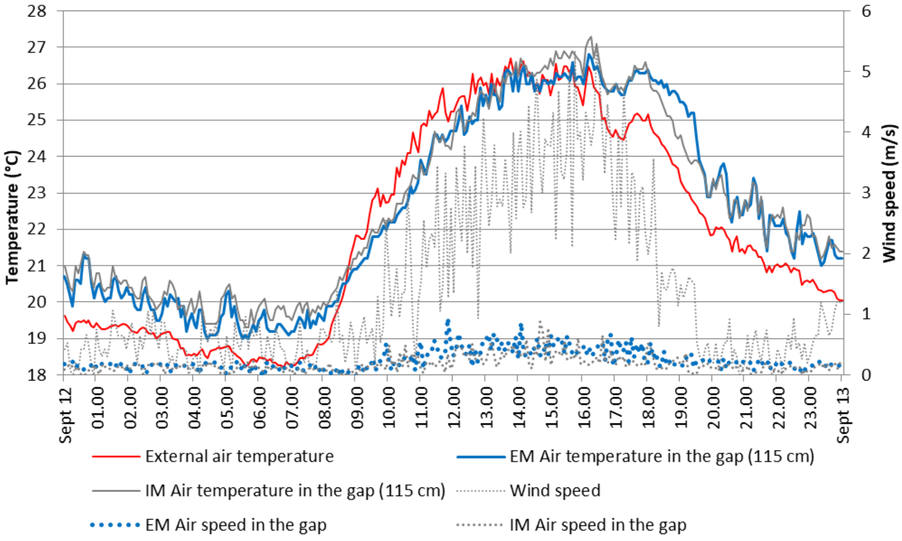

Figure 4.18: Temperature trends within the cavity for EM and IM prototypes with respect to the external air temperature and wind speed plotted for a single summer day (September 12th).

For both walls, the air temperatures within the gaps followed a similar trend, with maximum air temperatures approximately between 26-27 °C and minimum values around 19°C. The air velocity in the cavity for both walls peaked in the middle of the day when the outdoor temperature touched higher values than the temperature in the gap. Indeed, the airflow rates greatly differed: namely in the EM wall the air mean velocity was 0.24 m/s against 0.17 m/s recorded in IM's. However, the average stack flow was low, since the temperature difference between the air in the gap and the outdoor air (T_{gap}) never exceeded approximately 1.5 °C. Throughout the night (00:00-07:00), when the outdoor temperature was lower than that within the gaps, the stack was much attenuated (positive $T_{gap} \cong 1$) and there was almost no wind force. Therefore, the airflow in the gap was negligible (mean air velocity of 0.14 m/s and 0.11 m/s for EM and IM, respectively). The EM air temperature in the gap reached the minimum peak. In the morning (07:00-14:00), the temperature difference between the air in the gap and the external air assumed a negative value since the temperature trends outdoors and within the cavity inverted their reciprocal positions. The wind force was prominent, reaching peaks over 3 m/s, meaning that the ventilation was mainly wind-driven. In this range, the airflow values increased to 0.3 m/s and 0.22 m/s, for EM and IM respectively. The EM air temperature remained slightly cooler than the IM counterpart. In the afternoon (14:00-17:00), when the sun hit the facades, a milder increase of the IM air temperature over EM's was recorded, with the latter still very close to the outdoors (until 16:00). However, the highest air speed in the gap belonged to EM wall (0.44 m/s against 0.34 m/s of IM). After 17:00, the outdoor temperature dropped, and the wind speed diminished. Consequently, for both walls, the air temperatures within the gaps decreased, with a smoother decline in EM (17:00-19:00).

Impact of the mass position in the airflow rates in winter

The comparison between the air temperatures and air speed within the gap (measured at 115 cm height from the inlet, at the center of the gaps) for the EM and IM walls is plotted in (Fig.4.19) for a single winter day (December 24th, with daily average solar radiation of 215 W/m^2 and mean wind speed of 1 m/s). For both walls, the air temperatures within the gaps were warmer by night and coldest by day with respect to the external air. Moreover, the air speed in the ventilation gap was close to zero at night while it reached the highest values in the central hours of the day. Also, in winter the airflow rates were quite different: EM configuration showed an air mean velocity of 0.18 m/s against 0.12 m/s recorded in IM. The average stack flow was low, with the temperature difference between the air in the gap and the outdoor air of about 2.5°C. However, this value is higher than the one found in summer, since the selected winter day is characterized by a lower mean wind speed (1 m/s) that impact less on the temperatures within the gap.

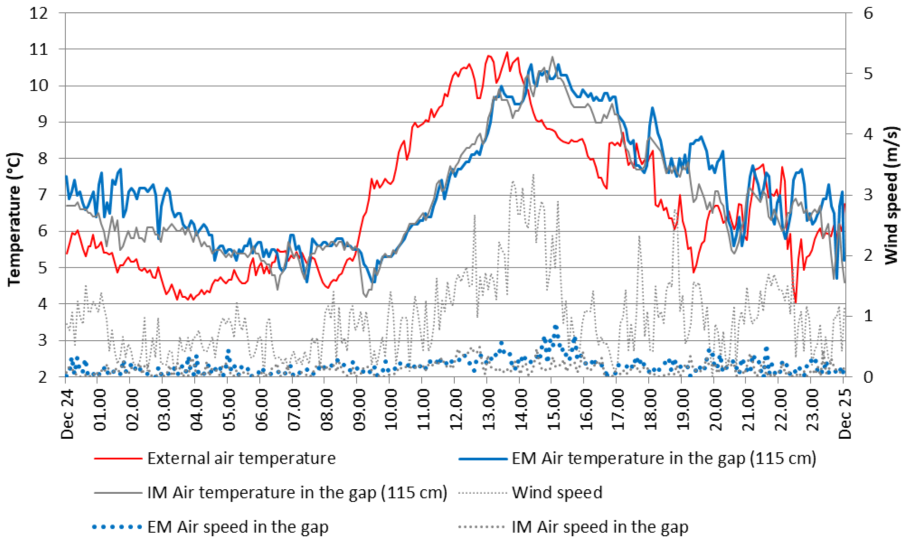

Figure 4.19: Temperature trends within the cavity for EM and IM prototypes with respect to the external air temperature and wind speed plotted for a single winter day (December 24th).

Chapter 5

Thermal behavior of the earth wall

The present chapter provides the results regarding the thermal behavior of the earth blocks panel. The thermal performance is analyzed by means of a monitoring campaign carried out in the summer months under different operative conditions.

5.1 Thermal responsiveness of the earth blocks panel under cooling system

A selection of 5 consecutive summer days are showed in (Fig.5.1), which reports outdoor temperatures fluctuations between a minimum of 17.9°C and a maximum one of 36°C, registering a mean value of 27°C. These values fall within the typical Mediterranean summer. The daily average solar radiation was around 500 W/m^2. The daily mean wind speed was low, approximately around 1.3 m/s.

The indoor air temperature (measured at the center of the room) and surface temperature trends of the three internal linings under Test 1 conditions (cooling system switched on) are showed in (Fig.5.2).

When the cooling system was on (Test 1), all the surface temperatures stayed higher than the indoor air, which fluctuated around its set-point value (26°C). The dry-clay panel (lining M) always registered the highest mean temperature (26.9°C) followed by the lining EB and L, respectively. However, among the three solutions, the lining EB exhibited the most flattened surface temperature profile, with a 0.26°C temperature difference between the maximum and minimum peaks.

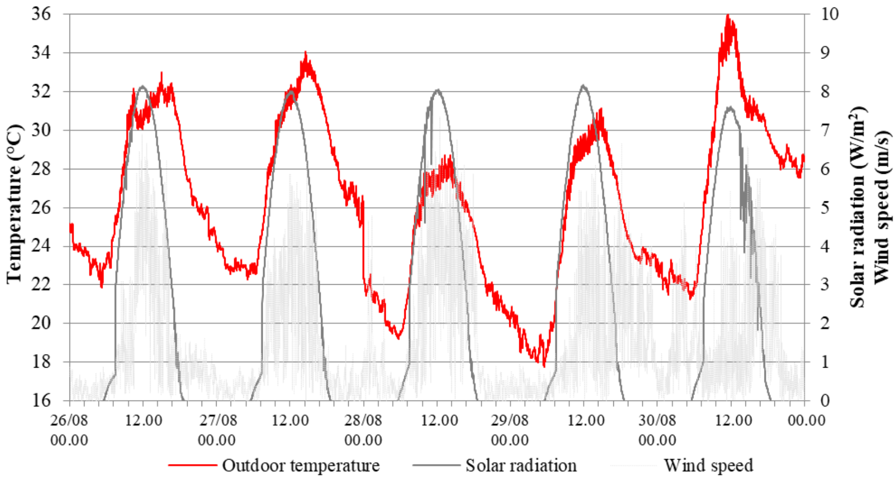

Figure 5.1: Outdoor weather conditions measured between August 26th-30th.

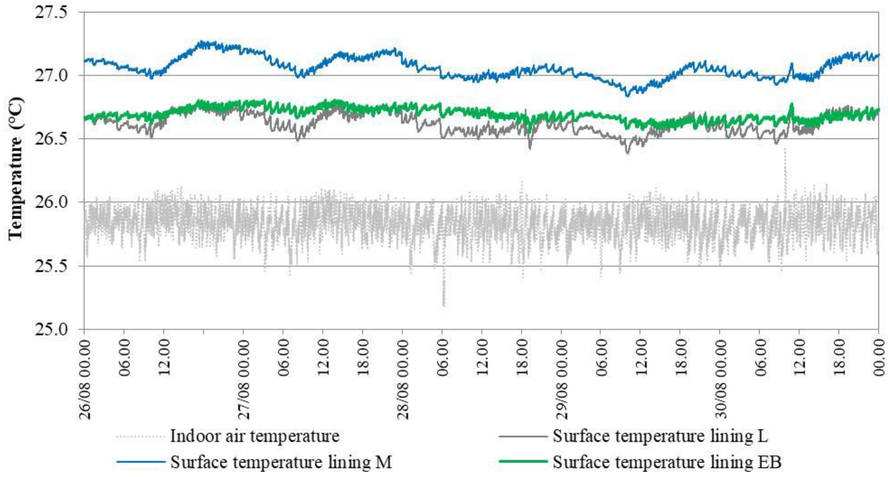

Figure 5.2: Internal linings surface temperatures and indoor air profiles measured between August 26th-30th.

The heat flowing profiles recorded on the linings surface are showed in (Fig.5.3). The negative sign of the thermal flux indicates that the lining is releasing the heat towards the indoor environment. Accordingly, the linings M and L emphasized the heat transfer towards the indoors between midday and sunset and minimized it in the morning hours. Notably, the lining L released the highest heat flux magnitude toward the test room (3.1 W/m^2). Conversely, the lining EB not only it stored the lowest heat flux values (0.76 W/m^2), but also released the lowest ones (2.2 W/m²), due to the higher thermal inertia of the component. This implies that the lining EB has a beneficial effect with regard to the summer indoor overheating.

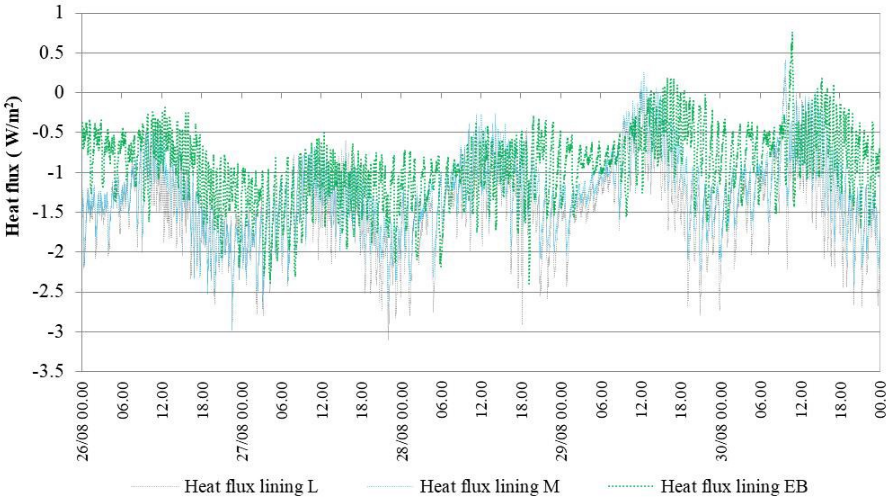

Figure 5.3: Heat flux profiles measured between August 26th-30th.

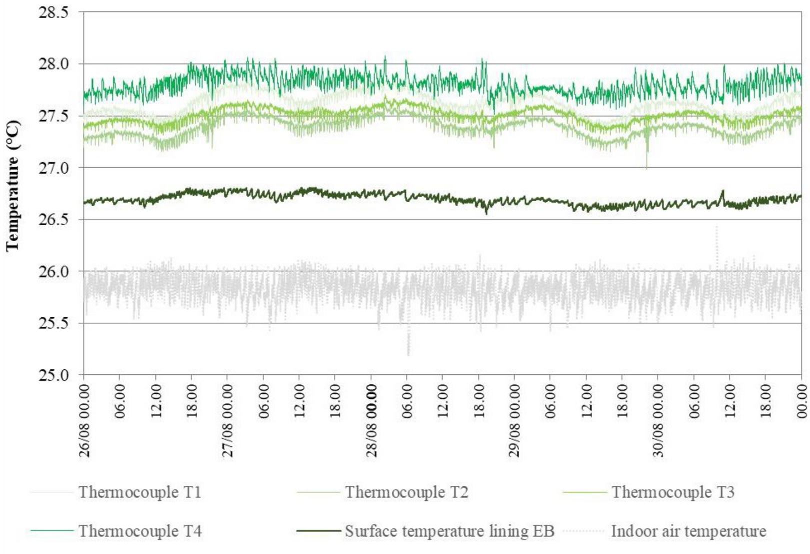

Figure 5.4: Temperatures measured inside the earth block panel between August 26th-30th.

The temperatures trends recorded by the thermocouples inside the earth block holes are presented in (Fig.5.4). All temperatures fell within a 1°C variation range. Overall, it is evident that, within the block, the temperatures were slightly higher than the EB surface's ones. Moreover, the thermocouple T4 (placed 25 mm from the block surface) registered the highest mean temperature value (27.6°C), fluctuating with an offset of 1.5 °C with respect to the lining EB's one.

5.2 Thermal responsiveness of the earth blocks panel under free-running regime

A sample of 5 consecutive summer days in which the outdoor temperature was typically high, varying between the range 14.2 – 29.7 °C and registering a mean value of 21°C is showed in (Fig.5.5). The weather was variable, including sunny days with solar radiation up to 800 W/m^2 (September 17th) and cloudy days (September 15th-16th). Wind speed was comparable to a light breeze (average value of 1.7 m/s).

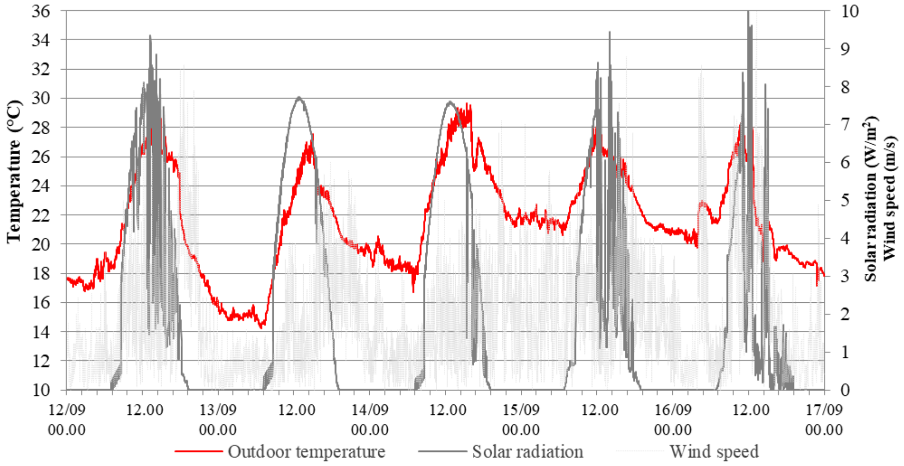

Figure 5.5: Outdoor weather conditions measured between September 12th-16th.

The indoor air temperature (measure at the center of the room) and surface temperature trends of the three internal linings under free-running mode (Test 2) are showed in (Fig.5.6). In free running regime, the surface temperatures trends followed the one of the indoor air. The dry-clay lining (M) recorded again the highest mean surface temperature (26.1°C). Average surface temperatures of plasterboard (L) and earth blocks panel (EB) were instead 25.7°C and 25.9°C, respectively. Between (00:00-14:00) time-slot, the lining EB surface was warmer than the plasterboard one. In the afternoon until midnight (14:00-00:00), their temperature trends reversed. The lining EB recorded lower surface temperatures in the afternoon and higher ones at night, shifting the diurnal temperature peak occurring on the lining surface thus limiting the indoor overheating phenomenon. From September 15th, the cooling system was switched on (set-point at 24°C) to cool down the mock-up indoor microclimate. As expected, in conjunction with this event, all the recorded temperatures inside the test room abruptly dropped. However, it is interesting to note that, thanks to its significantly thermal features, lining EB trend fell down with a less steep descending slope.

Heath fluxes profiles of linings L, M and EB are presented in (Fig.5.7). Under Test 2 conditions, all the three linings retained the heat (positive sign of the heat flux) more than the quota they released. It can be seen that the massive lining EB retained more heat during the warmest hours (due to its higher thermal capacity) and released it more by night, with respect to the other configurations with less inertia. When the cooling system was switched on, the reversal of the heath fluxes trends occurred.

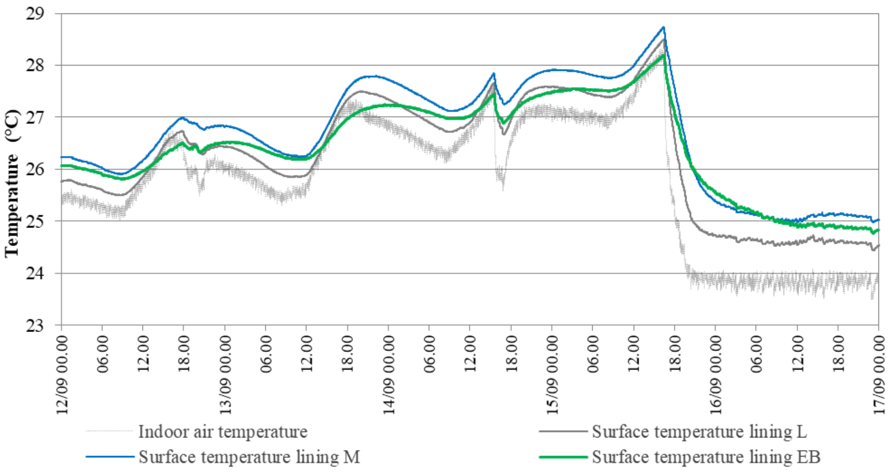

Figure 5.6: Internal linings surface temperatures and indoor air profiles measured between September 12th-16th.

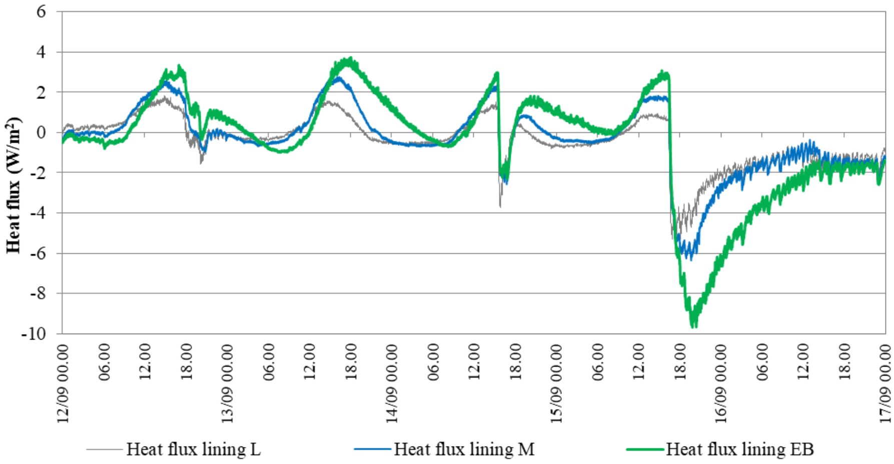

Figure 5.7: Heat flux profiles measured between September 12th-16th.

The temperatures trends of the thermocouples positioned in the block holes are illustrated in (Fig.5.8). Also, under Test 2 conditions, the temperatures within the block recorded higher values with respect to the EB surface's. Again, the thermocouple T4 showed the highest mean temperature value (27.9°C), maintaining an offset of 1.5 °C with respect to the lining EB's one.

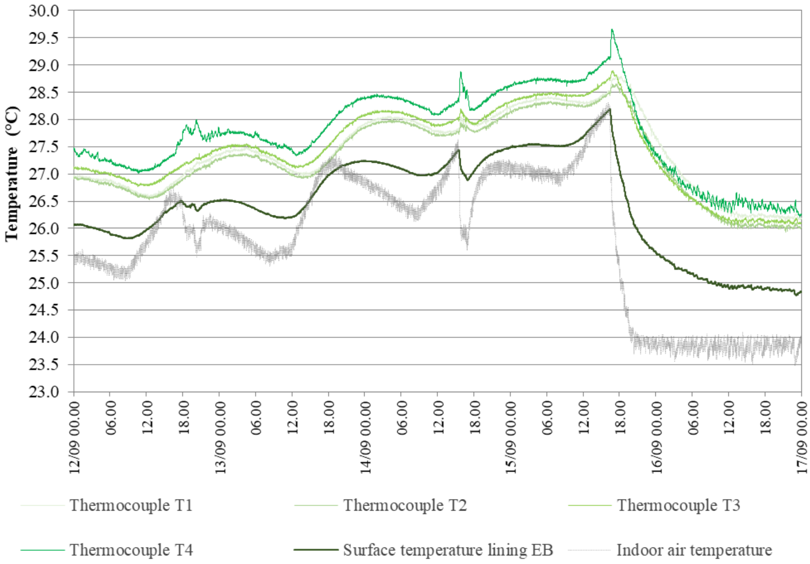

Figure 5.8: Temperatures measured inside the earth block panel between September 12th-16th.

5.3 Discussion

Two single days (August 29th and September 13th), belonging respectively to Test 1 and Test 2 indoor operative conditions and characterized by similar outdoor temperatures, were chosen and compared in order to gain insights onto the thermal behavior of the earth blocks panel (EB) with respect to the mitigation potential of the indoor environment (Fig.5.9).

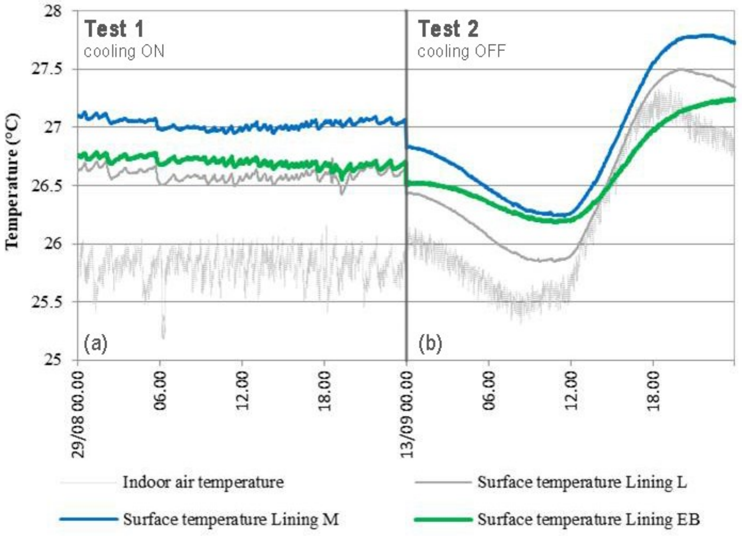

Figure 5.9: Comparison between the surface temperatures trends of linings L, M and EB under (a) Test 1 and (b) Test 2 scenarios.

When the cooling system was switched on (Fig.5.9a), the surface temperature trends followed the indoor air one, showing a flattened behavior, slightly oscillating around their mean value. The lining EB mean temperature surface value was 0.7° higher than the set-point one. When the microclimate control was off (Fig.5.9b), the surface temperatures followed the outdoor air temperature fluctuations. When the outdoor temperature began to rise, the linings surface temperatures also increased their values (with a slight shifting of the temperature peaks). Among them, the lining EB thanks to its higher thermal inertia rose gradually up to a temperature peak (27.2 °C) lower than the others. This behavior impacts positively in the mitigation of the summer indoor overheating, since the expected operative conditions of the mock-up will guarantee the best indoor comfort.

The different Test 1 and Test 2 operative systems strongly affected also the flywheel trends of all the three linings (Fig.5.10). When the cooling system was switched on, the lining EB, despite the prevalent heat direction towards the indoors, provided the smallest contribution to the indoor overheating (Fig5.10a). When the cooling system was off, the EB lining proved again to be the most successful in regulating the indoor microclimate, storing the highest quota of heat and releasing it towards the outdoors (Fig5.10b).

(Fig.5.11) presents the hourly temperature profiles from the indoor environment to the outdoors linearized in four time slots representative of the night (00:00), the morning (06:00), midday (12:00) and the evening (18:00) in order to study the temperature variations overtime. Regardless of the variation of the outdoor and indoor boundary conditions, the temperatures within the block holes stayed always approximately 1.5 °C higher with respect to the lining EB surface (Fig.511a,b). This behavior could be justified by the presence of a greenhouse that was built adjacent to the south wall of the mock-up at the time of the experimentation, which emphasized the heat transfer towards the room. Therefore, the high values recorded inside the greenhouse (over 50 °C) directly affected the temperatures within the block, despite the high thermal resistance of the building envelope.

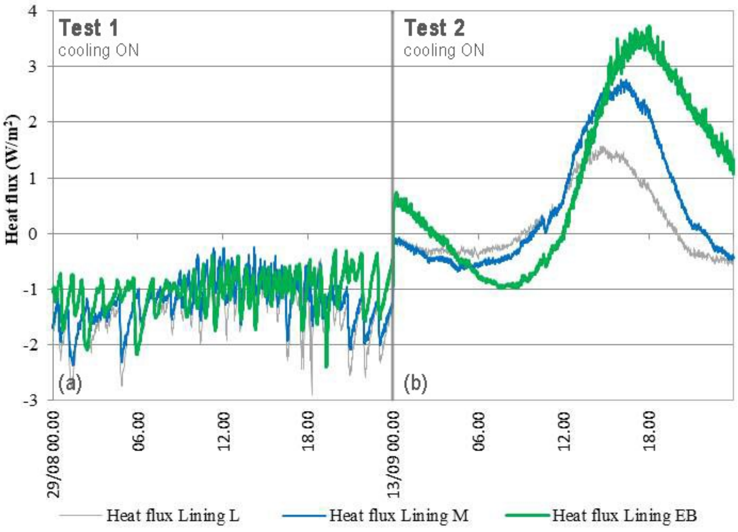

Figure 5.10: Comparison between the heat flux trends of linings L, M and EB under (a) Test 1 and (b) Test 2 scenarios.

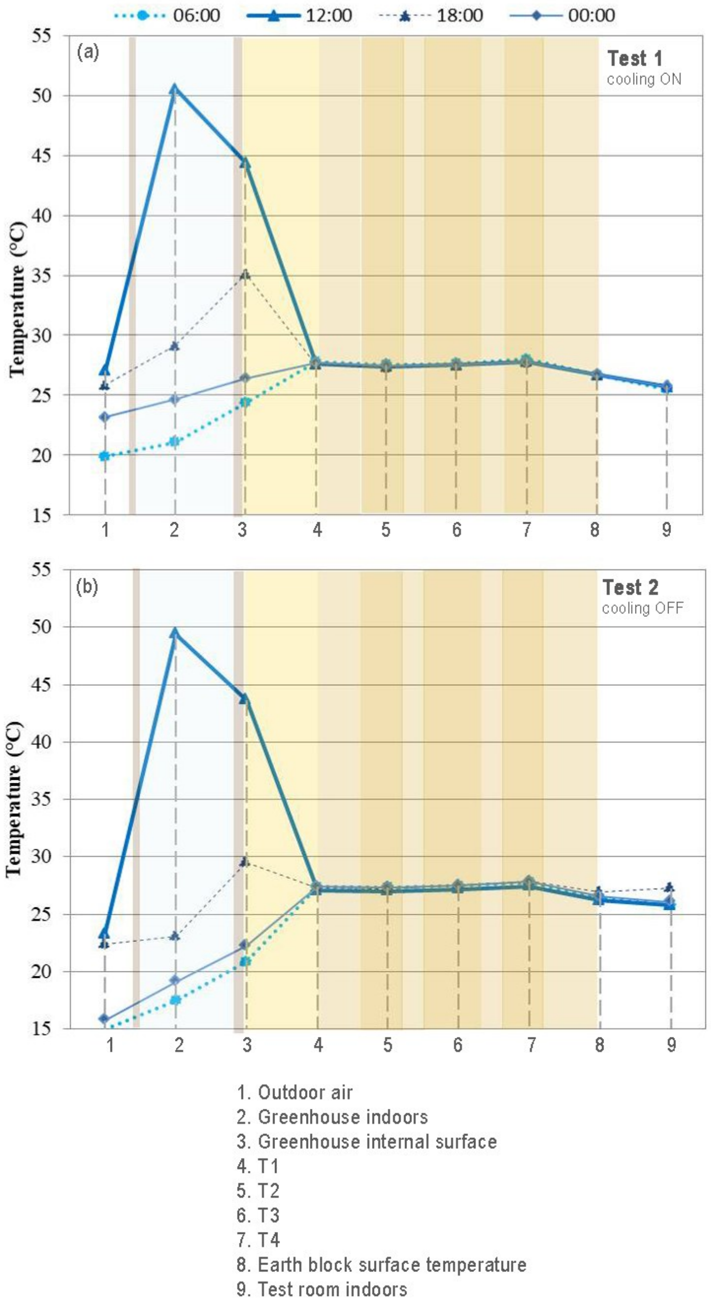

Figure 5.11: Comparison between the hourly temperature values from the outdoors to the indoors under (a) Test 1 and (b) Test 2 scenarios.

Chapter 6

Mechanical behavior of the earth wall

The chapter collects the results regarding the mechanical behavior of the earth blocks wall. The structural behavior of the wallettes was investigated by employing DIC technique to obtain the complete strains fields.

6.1 Material characterization

The compressive strengths of the earth blocks are summarized in Table 6.1. The average compressive strength f_{cm} was found to be 3.4 N/mm^2. As expected, this value is quite low as compared to the compressive strength of traditional baked bricks, commonly around 16 N/mm^2 [79].

Table 6.1. Compressive strength of the earth blocks.

Specimen	Avg. compressive strength f_{cm} (N/mm^2)	SD (N/mm^2)	COV (%)
A1-A9	3.4	0.4	0.12

The failure mode was the same for all the specimens tested, with cracks originating before the peak load (Fig.6.1a). Cracks were located on the front and back sides of the blocks, close to the point of application of the load.

The average and characteristic initial shear strengths f_{voi} and f_{vok} parallel and perpendicular to the dovetail joints (configurations A and B) are reported in Table 6.2. The characteristic initial shear strength f_{vok} parallel to the dovetail joints was 0.03 N/mm^2. The coefficient of variation (COV) is relatively high, as typical in handmade construction processes. The typical failure mode is reported in (Fig.6.1b). The characteristic initial shear strength f_{vok} perpendicular to the dovetail joints was 1.90 N/mm². The failure mode is reported in (Fig.6.1c), denoting a good interlocking effect of the dovetail joint and corner expulsion.

Table 6.2: Initial shear strengths of the triplets.

Specimen °	Avg. tensile strength f_{vo} (N/mm²)	Characteristic tensile strength f_{vok} (N/mm²)	SD (N/mm²)	COV (%)
Configuration A	°	°	°	°
TA1-TA3	0,04	0.03	0.01	18,6
Configuration B	°	°	°	°
TB1-TB3	2.37	1.90	0.14	5.8

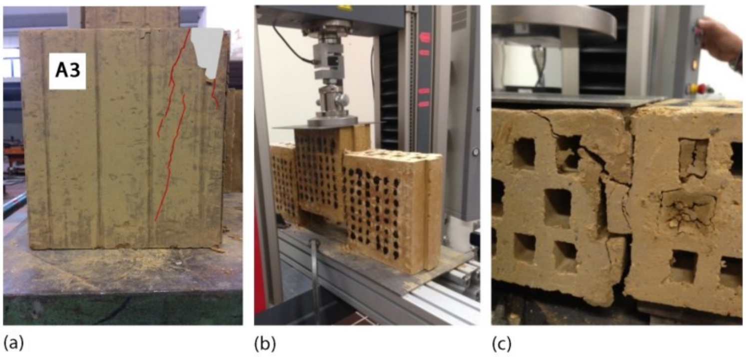

Figure 6.1: Failure modes of (a) the earth block, (b) of the triplet (configuration A) and (c) of the triplet (configuration B).

6.2 Compression test results on the wallettes

The stress – strain diagrams for the 3 wallettes is shown in (Fig.6.2), where the strain values were obtained through DIC and post-processed in MATLAB. The specimens exhibited an approximately linear behavior up to the maximum load with a brittle failure. The compressive strength f_c, Young's modulus determined at 1/3 of maximum stress E_i and Poisson's ratio ν of the wallettes are summarized in Table 6.3. The mean value of the compressive strength of the wallettes f_{cm} was approximately 2 N/mm².

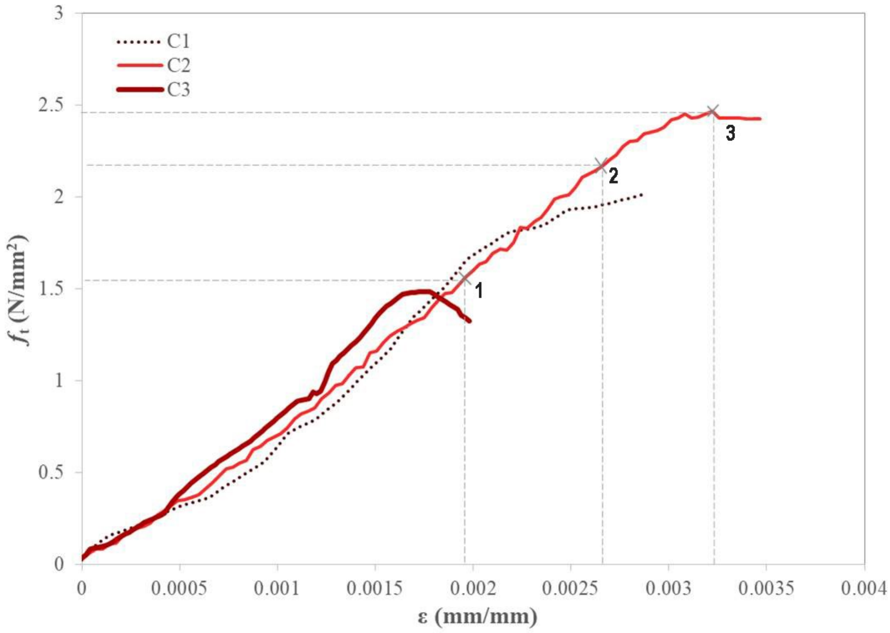

Figure 6.2: Stress – strain curves of the wallette specimens under compression test.

Table 6.3: Compressive strength, Young modulus and normal strain of the wallette.

Specimen	f_c (N/mm²)	E_i (N/mm²)	ν
C1	2.02	591	0.22
C2	2.46	703	0.23
C3	1.48	740	0.28
f_{cm}	1.99	678	0.24
SD	0.49	78	0.03
COV	25%	11%	13%

The DIC allowed recovering the complete deformation field at each point of the wall. The evolution in time of the vertical displacement s_y, the vertical strain ε_y and the shear strain γ_{xy}, are shown in three distinct frames (Fig.6.3) corresponding to the three highlighted points of (Fig.6.2). From the evolution of s_y, it could be noted that the wall behaves as a series of vertical slender adjacent columns rather than a cohesive unit (Fig.6.3a). Indeed, the alignment of the vertical joints avoids the uniform downward distribution of the load. This leads to a modest out-of-plane instability phenomenon (confirmed by the 3D-DIC), which is slightly mitigated by the presence of the dovetail joints. As expected, the ε_y is uniformly distributed on the ROI surface with evident areas of strain concentration (Fig.6.3b). The “column effect” is also visible by the evolution of the γ_{xy} which registered high relative slidings between the vertical members (Fig.6.3c).

The cracks history of the specimens under uniaxial compression load obtained through a visual survey is presented in (Fig.6.4). The cracks propagated from the upper region of the specimens and along the masonry surface, with clay expulsions in proximity of the applied force. The cracks lines on the single columns surface were not visible in the strain γ_{xy} maps since the ROI mesh captured the global failure behavior, rather than the local one. It is clear from the figure that, since the second and fourth columns were subject to a vertical displacement, the load was supported completely by the other three columns.

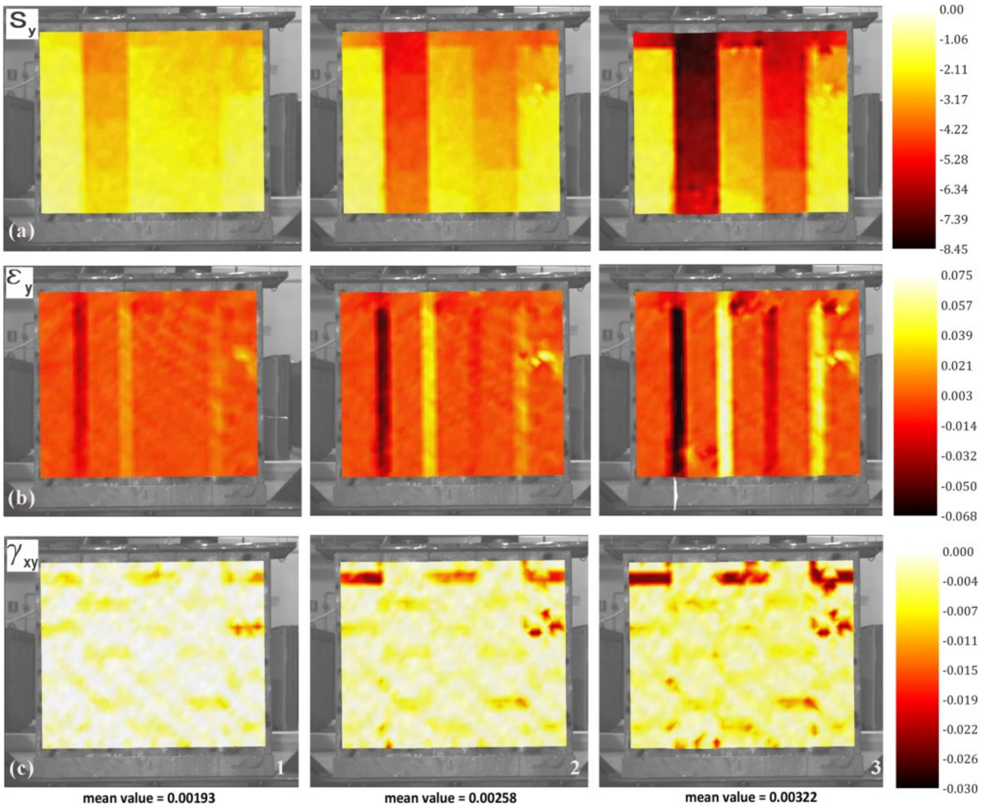

Figure 6.3: Complete displacement and strains fields of the wallette under uni-axial compression load.

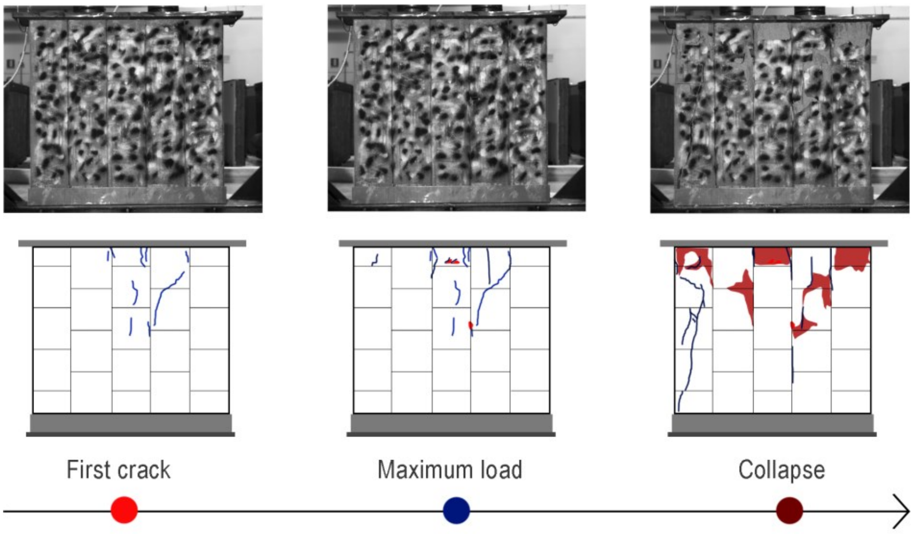

Figure 6.4: Hand-drawn history of the cracking pattern of the wallette under uniaxial compression load.

6.3 Diagonal compression test results on the wallettes

The shear stress–strain curves for the 3 wallettes are presented in (Fig.6.5). It can be noted a distinctive yield point when the elasticity of the specimen exceeded, and first cracks appeared. The collapse occurred later, after an increment of the diagonal compression force. The tensile strength f_t, shear modulus G and shear strain of the wallettes are reported in Table 6.4. The diagonal compression test registered a very low average strength value f_{tm} (0.00245 N/mm^2). This is due to the specific construction technique which relies only on the friction between the horizontal and the vertical dovetail joints since the thin mortar layer is characterized by low resistance.

The evolution in time of the horizontal displacement s_x, the vertical displacement s_y and the shear strain γ_{xy}, is illustrated for three distinct moments (Fig.6.6) corresponding to the three highlighted points of (Fig.6.5). The evolution of displacements s_x and s_y highlighted that, for low values of the applied load, the specimen opened in two parts with a rigid motion along the loading line. This is due to the low adhesion at the interface between the blocks (Fig.6.6a,b).

Additionally, slidings along the joint lines were also visibile from the γ_{xy} maps (Fig.6.6c).

The cracks history of the specimens under a diagonal compression load derived from a visual inspection is presented in (Fig.6.7). All specimens exhibited brittle behaviour and sudden failure. Fragile type-cracks originated very close to the normal loading line and propagated through the joints, without damaging the blocks. At the end of the tests, all the specimens were completely disrupted.

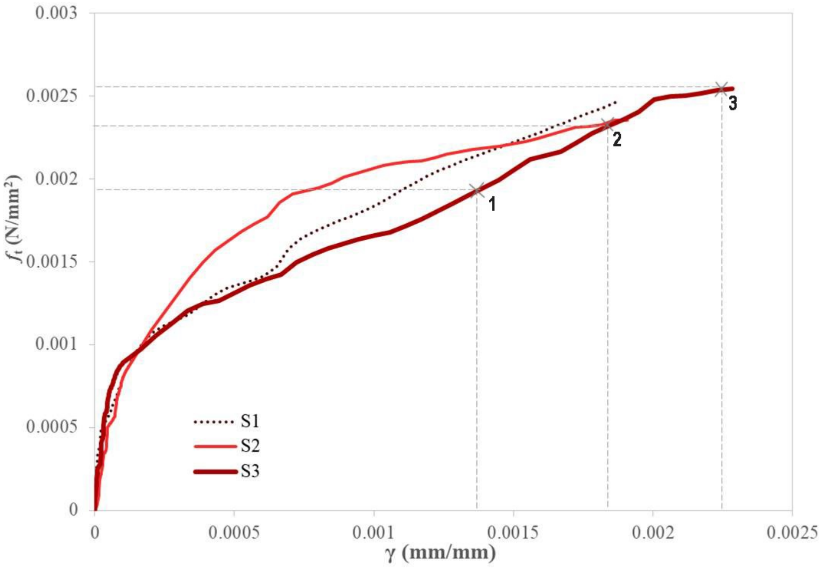

Figure 6.5: Shear stress–strain curves of the wallettes specimens under diagonal compression test.

Table 6.4: Tensile strength, shear modulus and shear strain of the wallettes.

Specimen	f_t (N/mm^2)	G (N/mm^2)	γ
S1	0.00246	7.76	0.000105718
S2	0.00236	8.09	9.70814E-05
S3	0.00254	10.20	8.26778E-05
f_{tm}	0.00245	8.68	9.51591E-05
SD	0.00009	1.32	1.16398E-05
COV	4%	105%	12%

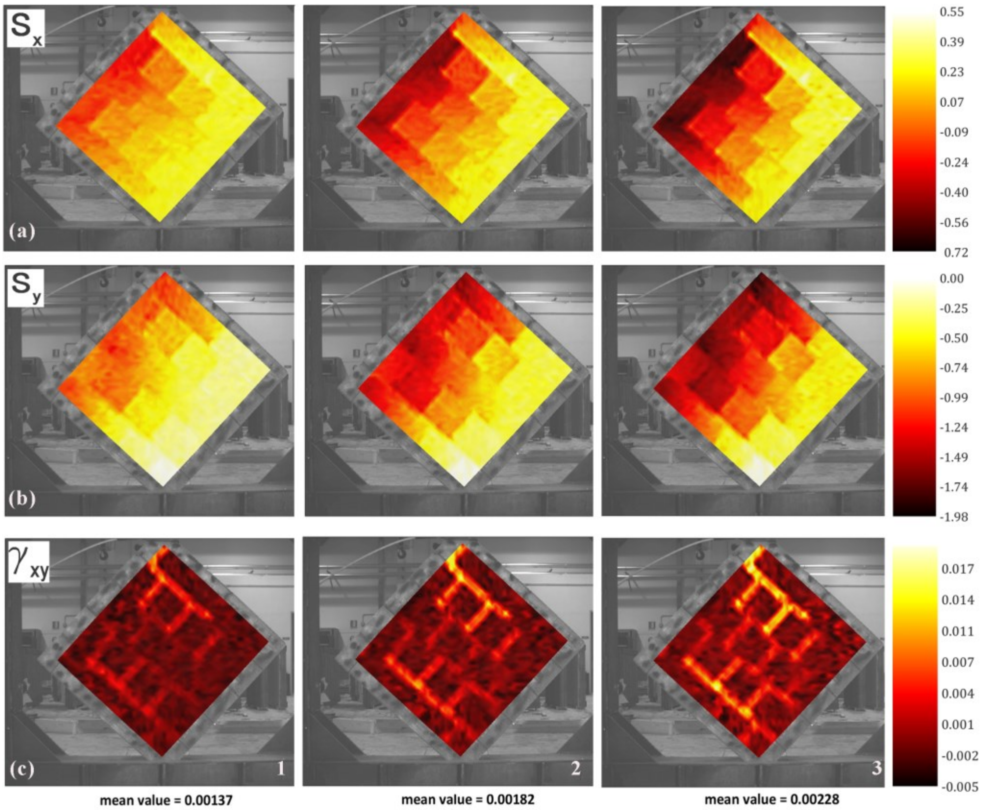

Figure 6.6: Complete displacement and strains fields of the wallette under diagonal compression load.

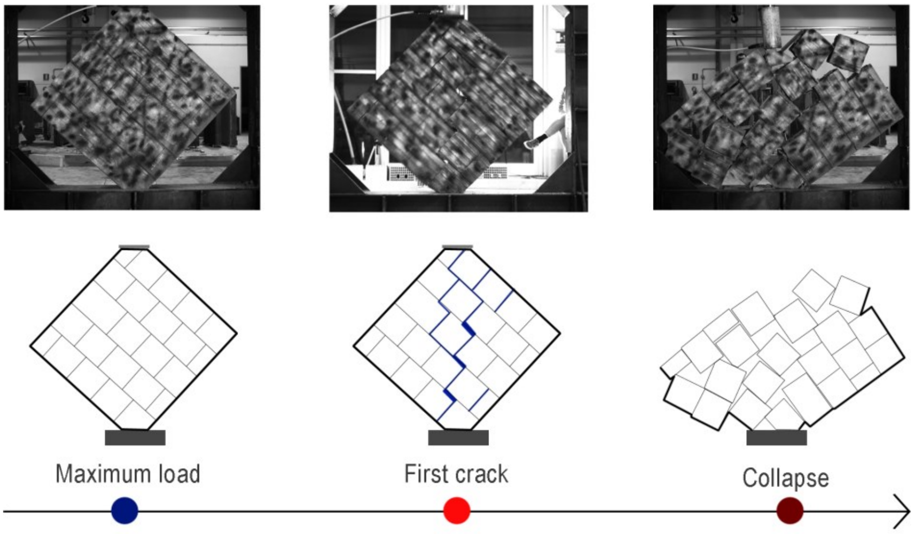

Figure 6.7: History of the cracking pattern of the wallette under diagonal compression load.

6.4 Shear tests with the pre-compression results on the wallettes

The results obtained under different pre-compression values (0.2 N/mm^2 and 0.4 N/mm^2) were quite similar therefore only the shear stress–strain diagrams for the 3 specimens subject to a pre-compression load of 0.2 N/mm^2 are here presented (Fig.6.8). In the first part, the curves showed a linear trend until the first crack appeared. Then, a plastic region occurred with formation of diagonal cracks until failure. The tensile strength f_t, shear modulus G and shear strain γ of the wallettes are collected in Table 6.5. As expected, the test showed a slight increase (about 2.4%) in terms of tensile strength with respect to the diagonal tensile findings without pre-compression.

The evolution in time of s_x, s_y and γ_{xy} were recovered (Fig. 6.9). As expected, the horizontal displacement s_x showed an approximatly linear trend along the vertical axis (Fig. 6.9a). The vertical displacement s_y showed a relevant sliding along the vertical joints. This phenomenon has already been pointed out in the full strain maps of the compression test (Fig. 6.9b). In the shear strain γ_{xy} maps, two inclined crack lines originating from the point of application of the shear force were visible (Fig. 6.9c).

The hand-drawn cracks history of the specimens under a shear and constant compression load is represented in (Fig.6.10). Indeed, given that the masonry doesn't have aligned horizontal joints, a sliding shear failure along the central part of the specimen, as it happens in traditional masonry, is not possible. Failure was associated with superficial cracks on the specimens surface.

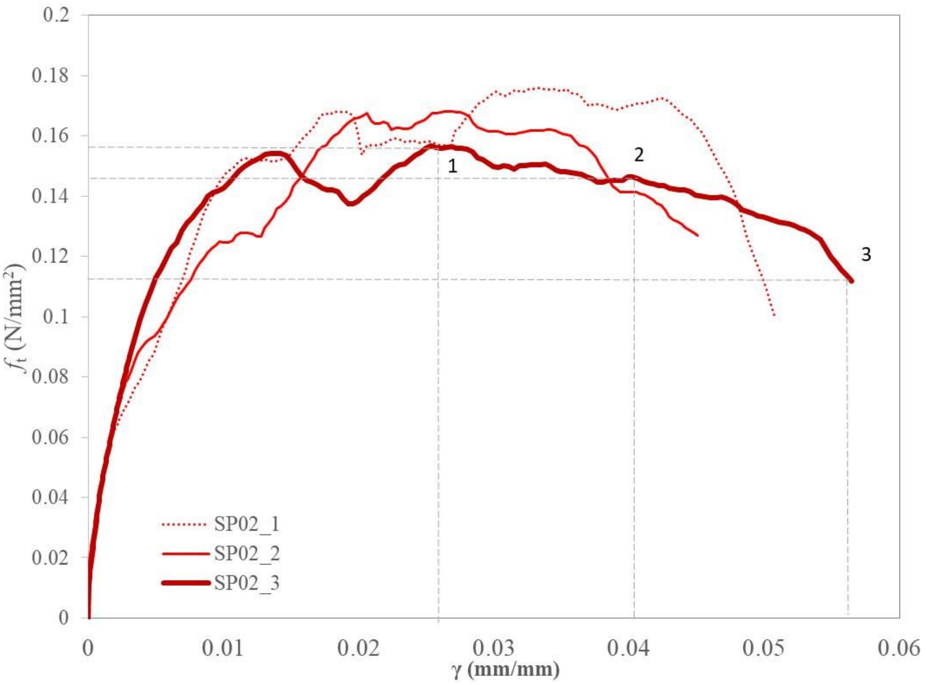

Figure 6.8: Shear-strain curves of the wallettes specimens under a shear and 0.2 N/(mm^2) constant compression load.

Table 6.5. Tensile strength, shear modulus and shear strain of the wallettes under a pre-compression load.

Specimen	f_t (N/mm^2)	G (N/mm^2)	γ
SP02_1	0.176	35	0.051
SP02_2	0.168	40	0.045
SP02_3	0.157	39	0.056
f_{tm}	0.167	38	0.051
SD	0.010	3	0.006
COV	5.7%	7.0%	11.2%

SP04_1	0.176	344	0.048
SP04_2	0.171	310	0.035
SP04_3	0.180	329	0.042
f_{tm}	0.176	327	0.041
SD	0.005	17	0.006
COV	0.027	0	0.148

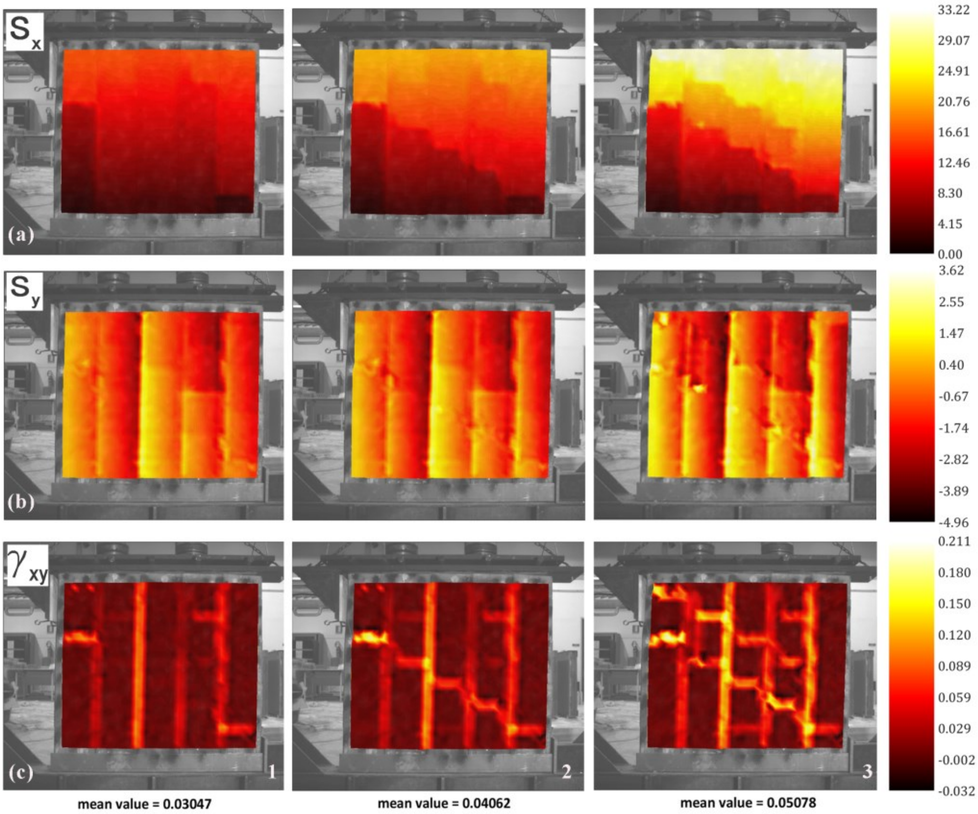

Figure 6.9: Complete displacements and strain field of the wallette under a pre-compression load.

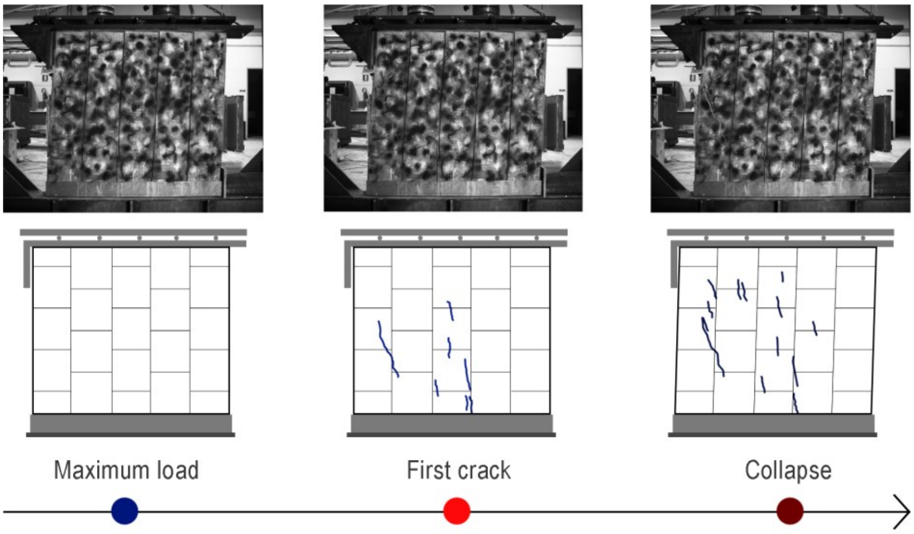

Figure 6.10: History of the cracking pattern of the wallette under a shear and precompression load.

6.5 Discussion

The collected data have been compared with the ones available from other researches, in order to determine where the obtained mechanical results stands within the masonry framework.

The average compressive strength f_{cm} of the single unit (earth blockn with dovetail joints) was compared with the ones of either unbaked bricks with different mixtures, namely adobe block [80], earth block without stabilizers and manually compressed [81], earth block with coarse sand [81], and compressed earth block CEB [82]. The average compressive strength f_{cm} values were summarized in the bar chart in (Fig.6.11). The adobe block mixed with variably sized straw fibers and water had the lowest value, without exceeding 1.47 N/mm^2. Quagliarini et al. found that a block made only of compressed earth mixture and produced by manual compaction almost duplicate the mean compressive value obtained by the latter (2.88 N/mm^2). However, the same author underlined that an increment of the volume fraction of coarse sand (over 40%) and a decrement of straw fibers (0.2%) diminishes the average compressive strength of the block down to 2.14 N/mm^2. The unbaked earth block with dovetail joints registered and higher value of f_{cm} (3.4 N/mm^2). Indeed, the presence of wood fibers in the mixture positively influenced the overall compressive strength value. Within the unbaked masonry framework, the CEB is the one achieving the highest average compressive strength (around 15.15 N/mm^2) given that such technology also takes into account cement content and water in the mixture [82].

The average tensile strength f_{vo} parallel to the dovetail joints of the triplet configuration A was compared with the ones of several triplet configurations made of different brick and mortar assemblies given the lack of data regarding experimentation on unbaked clay (Fig.6.12). The lowest tensile value (0.02 N/mm^2) was found for the concrete bricks and cement mortar triplet where the poor adhesion force was attributed to the reduced surface contact in the brick-mortar interface [83]. A slightly better result (0.04 N/mm^2) was obtained both by the unbaked triplet with dovetail joints and the clay brick-lime mortar configuration tested in [84]. The same author tested also two other types of mortar, namely cement lime and cement, which increased the shear bond up to 0.2 N/mm^2 and 0.5 N/mm^2, respectively. The highest mortar-brick bond strength value was reached using cementitious mortar with recycled aggregate [85].

The values of the average compressive strength f_{cm} and the Young modulus E_i of the wallettes were compared with the ones of other unbaked earthen masonries. Data are presented in (Fig.6.13a). Besides the cob wall mechanical properties [86] that exhibited the lowest f_{cm} and E_i values (1.59 N/mm^2 and 651 N/mm^2 respectively), the unbaked earth wallette f_{cm} and E_i values were significantly lower than the ones of the rammed earth and earth block masonries [86]. Notably, the rammed earth configuration reached the highest values with an average compressive strength of 343 N/mm^2 and and elastic modulus of 4143 N/mm^2. The decrement in terms of compressive strength of the earth wallette could be due to the fact that the earth blocks assembly was designed as a veneer wall instead of a load bearing one.

The tensile strenght f_{tm} and shear modulus G of the unbaked earth wallette was compared with the results of the same earthen masonries in [86] (Fig.6.13b). As already mentioned, the unbaked earth wallette, tested under diagonal compression, exhibited a scarce tensile behavior. Indeed, the values of tensile strength (0.00245 N/mm^2) and shear modulus (8.68 N/mm^2), were the lowest among the masonries.

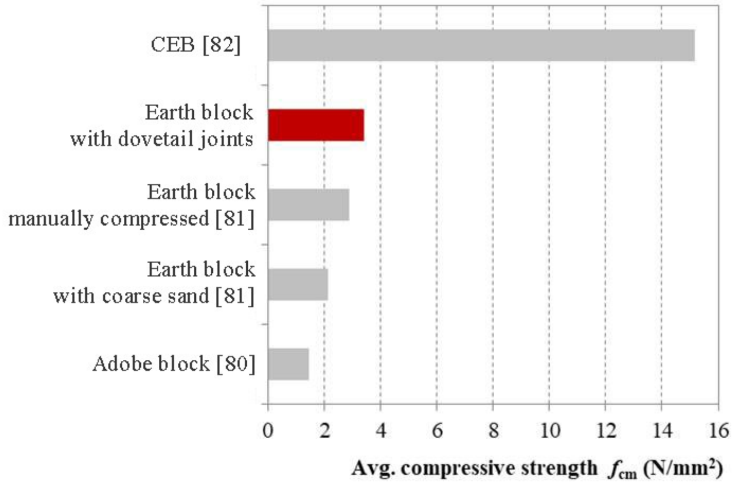

Figure 6.11: Comparison of the average compressive strengths of different types of earth bricks.

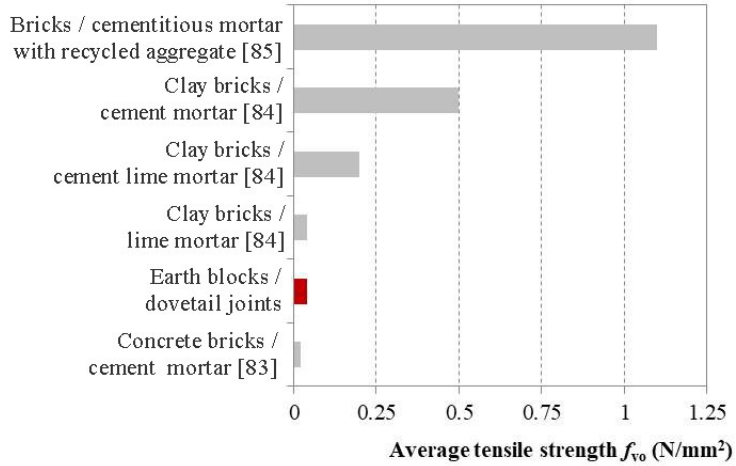

Figure 6.12: Comparison of the average tensile strengths of different types of triplet configurations.

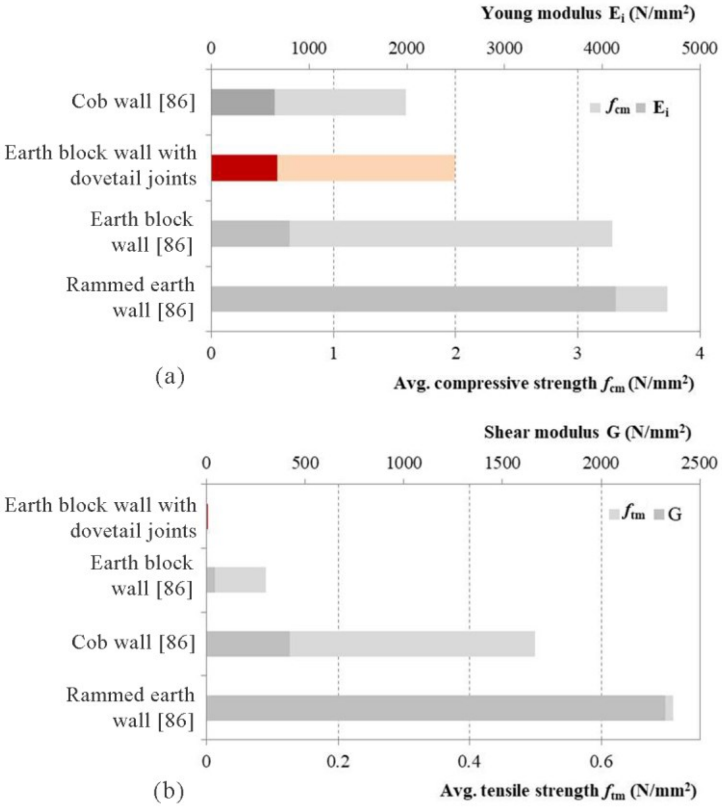

Figure 6.13: Comparison of the (a) compressive strengths and (b) tensile strengths of different types of earthen masonries.

Chapter 7

Conclusion

An experimental research on alternative solutions for energy and structural retrofits was performed. A multi-disciplinary approach was adopted with the aim of investigating the thermal and mechanical optimization of integrated technologies in CLT walls and PF structures.

Firstly, the present study addressed the energy optimization of the innermost and outermost sides of a CLT wall. To meet this goal, an extensive experimental monitoring campaign on a suitable mock-up was arranged, under Mediterranean climatic conditions. Four different internal linings and three ventilated prototypes were simultaneously tested under distinct combinations of outdoor and indoor thermal stress. The following conclusions were drawn:

- High thermal capacity walls with high internal areal heat capacity and very low decrement factor, namely H and H_I, proved not to be the best practice, when compared to medium thermal capacity solution with low f (0.072) and medium-high κ_1 (33 kJ/m^2K). In fact, the latter exerted the strongest smoothing action on the daily temperature swings. By adding an internal extra layer of insulation to the high thermal capacity lining (H_I), the heat losses lessened but a strong thermal barrier effect came into play. Therefore, such massive wall couldn't deploy its full battery capacity as the heat wave was hindered from reaching its deepest contingent penetration into the wall's layers. The best choice in hot summer climate was found to be the high thermal capacity solution (M) with f values not excessively low (>0.07). The adopted method also allows to extend the results to several climates, internal gains (according to different usage) and fenestration percentages since the experimental measures were carried out on a windowless mock-up;

- The ventilated prototype EM represented the optimal solution on annual basis, with regard to the other ventilated skins thermo-physical performance and natural ventilation potential under study. The insertion of a thermal mass in the outer layer increased the air velocity in the gap hence emphasizing the stack effect. Moreover, the incoming and outgoing heat fluxes through the envelope were reduced in summer and winter, respectively, as the outer mass operated as a thermal buffer between the outdoor and the ventilation chamber. Moreover, the EM facade coolest external surface temperatures can have a positive impact in regulating the urban microclimate overheating.

The obtained results underlined which was the best practice when facing the optimization of a lightweight and hyper-insulated building in Mediterranean climate. Therefore, these findings could be useful for designers of the external envelope that will be guided towards (i) solutions for the innermost layer with low but not excessively low decrement factor *f* (around 0.07) and high internal thermal inertia (higher than 30 kJ/m^2K) and (ii) the inclusion of a thermal mass on the façade outermost surface that maximizes the external areal heat capacity of the building envelope.

Further, the work investigated the thermal and structural performance of an enclosure wall made of unbaked earth blocks that are adopted in PF buildings. To such extent, an extensive summer monitoring campaign on a earth blocks panel and a set of laboratory tests on earth blocks wallettes were carried out. Results showed that:

- The adoption of an earth blocks panel in the innermost side of a lightweight and hyper-insulated building envelope provided a positive contribution to the regulation of the indoor environment that is prone to indoor overheating during Mediterranean hot summers. The high capacitive material was able to cool down its surface and retain more heat during peak hours, regardless of different operative conditions (switching on/off of the cooling system), thus implying better indoor comfort and a reduction in terms of energy consumption;
- The average compressive strength of the earth blocks wallettes was low (around 3.5 N/mm^2). The value was similar to the one of an adobe blocks. The initial tensile strength of the triplets was low (0.04 N/mm^2), regardless of the presence of the dovetail joints. The compression tests highlighted that the geometry of the block coupled with the horizontally staggered assembly led to a force distribution with a “column behavior”, as opposed to what happens in traditional masonries. However, the adoption of dovetail joints reduced possible out-of-plane instability phenomenon. The diagonal compression test

registered a low tensile resistance value (0.00245 N/mm^2) underlining that the low-quality earth mortar coupled with the joints vertical alignment did not guarantee a proper bond between the blocks thus enhancing the fragile behavior and the assembly disruption. The aforementioned mean tensile strength value of the wallettes had a slight increment (2.4%) when the specimens were also subject to a pre-compression load. The shear test under pre-compression loads shows an increasing of the shear resistance, thanks to the dovetail joints configuration providing the panel a monolithic behavior.

Overall, the unbaked earth blocks wallettes did not exhibit meaningful mechanical properties, as they recorded compressive and tensile values lower than other earth masonries. However, the wall assembly under study was not designed as load-bearing and the dovetail joints exhibited a good interlocking effect (f_{vok} 1.90 N/mm^2). Moreover, the DIC technique allowed recovering the effective displacements and strains fields on the overall region of interest of the specimens and visualizing the deformation and collapse mechanism, not easily identifiable with traditional test methods.

In conclusion, the thermal and structural findings on unbaked earth masonries experimentally assessed that the adoption of such a assembly as enclosure walls in PF structures, could be considered an effective integrated retrofit strategy for the energy optimization and structural improvement of light-framing buildings.

References

[1] Directive 2010/31/EU of the European Parliament and of the Council of 19 May 2010 on the energy performance of buildings.

[2] F. Clementi, E. Quagliarini, G. Maracchini, and S. Lenci, Post-World War II Italian school buildings: typical and specific seismic vulnerabilities, vol. 4, pp. 152–166, 2015.

[3] C. Regnier, K. Sun, T. Hong, and M. A. Piette, Quantifying the benefits of a building retrofit using an integrated system approach : A case study, Energy Build., vol. 159, pp. 332–345, 2018.

[4] A. Marini, C. Passoni, P. Riva, P. Negro, E. Romano, and F. Taucer, Technology options for earthquake resistant, eco-efficient buildings in Europe: Research needs, 1st edition, Publications Office of the European Union, 2014.

[5] Z. Ma, P. Cooper, D. Daly, and L. Ledo, Existing building retrofits: Methodology and state-of-the-art, Energy Build., vol. 55, pp. 889–902, 2012.

[6] F. Stazi, F. Tomassoni, A. Vegliò, and C. Di Perna, Experimental evaluation of ventilated walls with an external clay cladding, Renew. Energy, vol. 36, no. 12, pp. 3373–3385, 2011.

[7] S. Burhenne, O. Tsvetkova, D. Jacob, G. P. Henze, and A. Wagner, Uncertainty quantification for combined building performance and cost-benefit analysis," vol. 62, 2013.

[8] Dalla Mora T., Righi A., Peron F., Romagnoni P. (2017) Evaluation of Thermal Performance, Environmental Impact, and Cost Effectiveness of an XLam Component for Retrofitting in Existing Buildings. In: Sayigh A. (eds) Mediterranean Green Buildings & Renewable Energy. Springer, Cham.

[9] I. Sustersic and B. Dujic, Seismic strengthening of existing buildings with cross laminated timber panels, World Conference on Timber Engineering 2012, WCTE 2012. 4.

[10] Directive 2002/91/EC of the European Parliament and of the Council of 16 December 2002 on the energy performance of buildings.

[11] P. T. Tsilingiris, Wall heat loss from intermittently conditioned spaces. The dynamic influence of structural and operational parameters, Energy Build., vol. 38, no. 8, pp. 1022-1031, 2006.

[12] S. A. Al-Sanea and M. F. Zedan, Improving thermal performance of

building walls by optimizing insulation layer distribution and thickness for same thermal mass, Appl. Energy, vol. 88, no. 9, pp. 3113–3124, 2011.

[13] E. Kossecka and J. Kosny, Influence of insulation configuration on heating and cooling loads in a continuously used building, Energy Build., vol. 34, no. 4, pp. 321–331, 2002.

[14] F. Ascione, R. F. De Masi, F. de Rossi, S. Ruggiero, and G. P. Vanoli, MATRIX, a multi activity test-room for evaluating the energy performances of 'building/HVAC' systems in Mediterranean climate: Experimental set-up and CFD/BPS numerical modeling, Energy Build., vol. 126, pp. 424–446, 2016.

[15] F. Ascione, R. F. De Masi, F. de Rossi, S. Ruggiero, and G. P. Vanoli, "MATRIX, a multi activity test-room for evaluating the energy performances of 'building/HVAC' systems in Mediterranean climate: Experimental set-up and CFD/BPS numerical modeling" Energy Build., vol. 126, pp. 424–446, 2016.

[16] P. T. Tsilingiris, Parametric space distribution effects of wall heat capacity and thermal resistance on the dynamic thermal behavior of walls and structures, Energy Build., vol. 38, no. 10, pp. 1200–1211, 2006.

[17] S. A. Al-Sanea, M. F. Zedan, and S. N. Al-Hussain, Effect of thermal mass on performance of insulated building walls and the concept of energy savings potential, Appl. Energy, vol. 89, no. 1, pp. 430–442, 2012.

[18] K. Gregory, B. Moghtaderi, H. Sugo, and A. Page, Effect of thermal mass on the thermal performance of various Australian residential constructions systems, Energy Build., vol. 40, no. 4, pp. 459–465, 2008.

[19] S. Verbeke and A. Audenaert, Thermal inertia in buildings: A review of impacts across climate and building use, Renew. Sustain. Energy Rev., no. May, pp. 1–19, 2017.

[20] C. Di Perna, F. Stazi, A. U. Casalena, and M. D'Orazio, Influence of the internal inertia of the building envelope on summertime comfort in buildings with high internal heat loads, Energy Build., vol. 43, no. 1, pp. 200–206, 2011.

[21] N. Aste, A. Angelotti, and M. Buzzetti, The influence of the external walls thermal inertia on the energy performance of well insulated buildings, Energy Build., vol. 41, no. 11, pp. 1181–1187, 2009.

[22] M. A. Fayazbakhsh, F. Bagheri, and M. Bahrami, An inverse method for calculation of thermal inertia and heat gain in air conditioning and refrigeration systems, Appl. Energy, vol. 138, pp. 496–504, 2015.

[23] L. Rodrigues, V. Sougkakis, and M. Gillott, Investigating the potential of adding thermal mass to mitigate overheating in a super-insulated low-energy timber house, Int. J. Low-Carbon Technol., vol. 11, no. 3, pp. 305–316, Sep. 2016.

[24] F. Stazi, C. Di Perna, and P. Munafò, Durability of 20-year-old external insulation and assessment of various types of retrofitting to meet new energy regulations, Energy Build., Vol. 41, no. 7, pp. 721-731, Jul 2009.

[25] D. Medjelekh, L. Ulmet, S. Abdou, and F. Dubois, A field study of thermal and hygric inertia and its effects on indoor thermal comfort: Characterization of travertine stone envelope, Build. Environ., vol. 106, pp. 57–77, 2016.

[26] C. Baglivo, P. M. Congedo, A. Fazio, and D. Laforgia, Multi-objective optimization analysis for high efficiency external walls of zero energy buildings (ZEB) in the Mediterranean climate, Energy Build., vol. 84, pp. 483–492, 2014.

[27] C. Baglivo and P. M. Congedo, Design method of high performance precast external walls for warm climate by multi-objective optimization analysis, Energy, vol. 90, pp. 1645–1661, 2015.

[28] F. Stazi, E. Tomassoni, and C. Di Perna, Super-insulated wooden envelopes in Mediterranean climate: Summer overheating, thermal comfort optimization, environmental impact on an Italian case study, Energy Build., vol. 138, pp. 716–732, 2017.

[29] D. Finney, Buildings for a future, Springedition, v.13, no.4. Green Building Press, 2004.

[30] C. Rosenzweig, W. D. Solecki, L. Parshall, M. Chopping, G. Pope, and R. Goldberg, Characterizing the urban heat island in current and future climates in New Jersey, Environmental hazards, vol. 6, no. 1, pp. 51–62, 2005.

[31] M. Santamouris, Regulating the damaged thermostat of the cities Status, impacts and mitigation challenges, Energy Build., vol. 91, pp. 43–56, 2015.

[32] E. Di Giuseppe, M. Pergolini, and F. Stazi, Numerical assessment of the impact of roof reflectivity and building envelope thermal transmittance on the UHI effect, 9th International Conference on Sustainability, Energy Procedia, vol. 134, no. 2016, pp. 404–413, 2017.

[33] Y. Wang, U. Berardi, and H. Akbari, Comparing the effects of urban heat island mitigation strategies for Toronto, Canada, Energy Build., vol. 114, pp. 2–19, 2016.

[34] M. Santamouris et al., Energy & Buildings On the energy impact of urban heat island in Sydney: Climate and energy potential of mitigation technologies, Energy Build., vol. 166, pp. 154–164, 2018.

[35] M. Santamouris, Using cool pavements as a mitigation strategy to fight urban heat island. A review of the actual developments, Renew. Sustain. Energy Rev., vol. 26, pp. 224–240, 2013.

[36] P. Seferis, P. Strachan, A. Dimoudi, and A. Androutsopoulos, Investigation of the performance of a ventilated wall, Energy Build., vol. 43, no. 9, pp. 2167–2178, 2011.

[37] M. Shahrestani et al., Experimental and numerical studies to assess the energy performance of naturally ventilated PV façade systems, Sol. Energy, vol. 147, pp. 37–51, 2017.

[38] D. Bikas, K. Tsikaloudaki, K. J. Kontoleon, C. Giarma, S. Tsoka, and D. Tsirigoti, Ventilated Facades: Requirements and Specifications Across Europe, Procedia Environ. Sci., vol. 38, pp. 148–154, 2017.

[39] M. Ibañez-puy, M. Vidaurre-arbizu, J. A. Sacristán-fernández, and C. Martín, Opaque Ventilated Façades: Thermal and energy performance review, Renew. Sustain. Energy Rev., vol. 79, no. April 2016, pp. 180–191, 2017.

[40] M. R. D. A. Santiago, F. Peci Lopez, Sensitivity study of an opaque ventilated façade in the winter season in different climate zones in Spain, Renew. En., vol. 75, pp. 524–533, 2015.

[41] E. Iribar-Solaberrieta, C. Escudero-Revilla, M. Odriozola-Maritorena, A. Campos-Celador, C. García-Gáfaro, Energy performance of the opaque ventilated facade, Energy Procedia, vol. 78, pp. 55–60, 2015.

[42] A. Gagliano, F. Nocera, and S. Aneli, Thermodynamic analysis of ventilated facades under different wind conditions in summer period, Energy Build., vol. 122, pp. 131–139, 2016.

[43] S. Fantucci, C. Marinosci, V. Serra, and C. Carbonaro, Thermal performance assessment of an opaque ventilated façade in the summer period: calibration of a simulation model through in-field measurements, Energy Procedia, vol. 111, no. September 2016, pp. 619–628, 2017.

[44] C. Sanjuan and M. J. Sua, Experimental assessment of the performance of open joint ventilated façades with buoyancy-driven airflow, Sol. Energy, vol. 91, pp. 131–144, 2013.

[45] F. Patania, A. Gagliano, F. Nocera, A. Ferlito, and A. Galesi, Thermofluid-

dynamic analysis of ventilated facades, Energy Build., vol. 42, no. 7, pp. 1148–1155, 2010.

[46] C. Alonso, F. Martín-consuegra, I. Oteiza, E. Asensio, G. Pérez, and I. Martínez, Effect of façade surface finish on building energy rehabilitation, Sol. Energy, vol. 146, pp. 470–483, 2017.

[47] F. Stazi, G. Ulpiani, M. Pergolini, and C. Di Perna, The role of areal heat capacity and decrement factor in case of hyper insulated buildings : An experimental study, Energy Build., vol. 176, pp. 310–324, 2018.

[48] M. Hall and D. Allinson, Analysis of the hygrothermal functional properties of stabilised rammed earth materials, Build. Environ., vol. 44, no. 9, pp. 1935–1942, 2009.

[49] P. Taylor and M. B. Luther, Evaluating rammed earth walls : a case study, Sol. E.nergy, vol. 76, pp. 79–84, 2004.

[50] F. Pacheco-Torgal and S. Jalali, Earth construction: Lessons from the past for future eco-efficient construction, Constr. Build. Mater., vol. 29, pp. 512–519, 2012.

[51] B. V. Venkatarama Reddy and P. Prasanna Kumar, Embodied energy in cement stabilised rammed earth walls, Energy Build., vol. 42, no. 3, pp. 380–385, 2010.

[52] O. Bayode, Y. Michael, and D. Adedeji, Review of economic and environmental benefits of earthen materials for housing in Africa, Front. Archit. Res., vol. 6, no. 4, pp. 519–528, 2017.

[53] E. Quagliarini and S. Lenci, The influence of natural stabilizers and natural fibres on the mechanical properties of ancient Roman adobe bricks, J. Cult. Herit., vol. 11, no. 3, pp. 309–314, 2010.

[54] C. H. Kouakou and J. C. Morel, Strength and elasto-plastic properties of non-industrial building materials manufactured with clay as a natural binder, Appl. Clay Sci., vol. 44, no. 1–2, pp. 27–34, 2009.

[55] V. Sharma, B. M. Marwaha, and H. K. Vinayak, Enhancing durability of adobe by natural reinforcement for propagating sustainable mud housing, Int. J. Sustain. Built Environ., vol. 5, no. 1, pp. 141–155, 2016.

[56] K. Ghavami, R. D. Toledo Filho, and N. P. Barbosa, Behaviour of composite soil reinforced with natural fibres, Cem. Concr. Compos., vol. 21, no. 1, pp. 39–48, 1999.

[57] Ş. Yetgin, Ö. Çavdar, and A. Çavdar, The effects of the fiber contents on the mechanic properties of the adobes, Constr. Build. Mater., vol. 22, no. 3,

pp. 222–227, 2008.

[58] H. Binici, Investigation of fibre reinforced mud brick as a building material, Constr. Build. Mater., vol. 19, pp. 313–318, 2005.

[59] L. Miccoli, A. Garofano, P. Fontana, and U. Müller, Experimental testing and finite element modelling of earth block masonry, Eng. Struct., vol. 104, pp. 80–94, 2015.

[60] D. Maskell, A. Heath, and P. Walker, Laboratory scale testing of extruded earth masonry units, J. Mater., vol. 45, pp. 359–364, 2013.

[61] EN 1015-11, Metodi di prova per malte per opere murarie Parte 11 : Determinazione della resistenza a flessione e a compressione della malta indurita, 2007.

[62] EN 1052-3, Metodi di prova per muratura - Determinazione della resistenza iniziale a taglio, 2007.

[63] J. Milosevic, M. Lopes, A. S. Gago, and R. Bento, Testing and modeling the diagonal tension strength of rubble stone masonry panels, Eng. Struct., vol. 52, pp. 581–591, 2013.

[64] M. L. Beconcini, P. Croce, and D. Pellegrini, Comportamento meccanico di tamponamenti in blocchi di laterizio rettificati e giunti sottili, L'indistria dei laterizi, vol. 106, pp. 113–128, 2007.

[65] M. A. Sutton, F. Matta, D. Rizos, R. Ghorbani, S. Rajan, and D. H. Mollenhauer, Recent Progress in Digital Image Correlation : Background and Developments since the 2013 W M Murray Lecture, Exp. Mech., pp. 1–30, 2017.

[66] N. McCormick and J. Lord, Digital image correlation, Mater. Today, vol. 13, no. 12, pp. 52–54, 2010.

[67] M. Tekieli, S. De Santis, G. de Felice, A. Kwiecień, and F. Roscini, Application of Digital Image Correlation to composite reinforcements testing, Compos. Struct., vol. 160, pp. 670–688, 2017.

[68] C. Caggegi, D. Sciuto, and M. Cuomo, Experimental study on effective bond length of basalt textile reinforced mortar strengthening system: Contributions of digital image correlation, Meas. J. Int. Meas. Confed., vol. 129, no. June, pp. 119–127, 2018.

[69] M. Di Benedetti, S. Cholostiakow, H. Fergani, E. Zappa, A. Cigada and M. Guadagnini, DIC for strain measurement in small scale GFRP RC specimens, SMAR 2015.

[70] B. Ghiassi, J. Xavier, D. V Oliveira, A. Kwiecien, and P. B. Lourenço,

Evaluation of the bond performance in FRP – brick components re-bonded after initial delamination, Compos. Struct., vol. 123, pp. 271–281, 2015.

[71] D. Markulak, T. Dokšanović, I. Radić, and I. Miličević, Structurally and environmentally favorable masonry units for infilled frames, Eng. Struct., vol. 175, no. March, pp. 753–764, 2018.

[72] Guerrero, N., Martínez, M., Picón, R. et al., Experimental analysis of masonry infilled frames using digital image correlation," Mater. Struct., vol. 47, no. 5, pp. 873–884, 2014.

[73] R. Ghorbani, F. Matta, and M. A. Sutton, Full-Field Deformation Measurement and Crack Mapping on Confined Masonry Walls Using Digital Image Correlation, Exp. Mech., vol. 55, no. 1, pp. 227–243, 2015.

[74] E. Speranzini, R. Marsili, M. Moretti, and G. Rossi, Image Analysis Technique for Material Behavior Evaluation in Civil Structures, Materials (Basel)., vol. 10, no. 7, p. 770, 2017.

[75] F. Stazi, Thermal inertia in energy efficient building envelopes, 1st edition, Butterworth-Heinemann, Italy, 2017.

[76] K.L. Getter, D. Bradley Rowe, J.A. Andresen, I.S. Wichman, Seasonal heat flux properties of an extensive green roof in a Midwestern U.S. climate, Energy Build., vol. 43, pp. 3548–3557, 2011.

[77] Lin Bau-Show, Yu Chin-Chung, Su Ai-Tsen, and Lin Yann-Jou, Impact of climatic conditions on the thermal effectiveness of an extensive green roof, Build. Environ., vol. 67, pp. 26–33, 2013.

[78] L. Zhu, R. Hurt, D. Correia, and R. Boehm, Detailed energy saving performance analyses on thermal mass walls demonstrated in a zero energy house, Energy Build., vol. 41, pp. 303–310, 2009.

[79] H. U. Sajid, M. Ashraf, Q. Ali, and S. H. Sajid, Effects of vertical stresses and flanges on seismic behavior of unreinforced brick masonry, Eng. Struct., vol. 155, no. April 2017, pp. 394–409, 2018.

[80] R. Illampas, I. Ioannou, and D. Charmpis, Adobe bricks under compression : Experimental investigation and derivation of stress – strain equation, Constr. Build. Mat., vol.53, pp. 83-90, 2014.

[81] Q. Piattoni, E. Quagliarini, and S. Lenci, Experimental analysis and modelling of the mechanical behaviour of earthen bricks, Constr. Build. Mat., vol. 25, pp. 2067-2075, 2011.

[82] J. Sitton, Y. Zeinali, W. Heidarian, and B. Story, Effect of mix design on compressed earth block strength, Constr. Build. Mat., vol. 158, pp. 124-131,

2018.

[83] S. B. Singh, P. Munjal, Bond strength and compressive stress-strain characteristics of brick masonry, J. Building Eng., vol. 9, pp. 10-16, 2017.

[84] V. Alecci, M. Fagone, T. Rotunno, M. De Stefano, Shear strength of brick masonry walls assembled with different types of mortar, Constr. Build. Mat., vol. 40, pp. 1038-1045, 2013.

[85] V. Corinaldesi and G. Moriconi, Behaviour of cementitious mortars containing different kinds of recycled aggregate, Constr. Build. Mat., vol. 23, pp. 289-294, 2009.

[86] L. Miccoli, U. Müller, and P. Fontana, Mechanical behaviour of earthen materials: A comparison between earth block masonry, rammed earth and cob, Constr. Build. Mat., vol. 61, pp. 327-339, 2014.

[87] E. Quagliarini, S. Lenci, and M. Iorio, Mechanical properties of adobe walls in a Roman Republican domus at Suasa, J. Cult. Herit., vol. 11, pp. 130-137, 2010.

Publications

- Di Giuseppe E., Pergolini M., Stazi F., “Numerical assessment of the impact of roof reflectivity and building envelope thermal transmittance on the UHI effect”, Seb 17, Energy Procedia, 2017;
- Stazi F., Pergolini M., Di Perna C., «Comportamento termico degli involucri alla luce dei criteri ambientali minimi (CAM)», Costruire in Laterizio 172, 2017;
- Stazi F., Ulpiani G., Pergolini M., Di Perna C., “The role of internal areal heat capacity and decrement factor in case of hyper insulated buildings: an experimental study”, Energy Build 176 (2018) 310-324;
- Stazi F., Ulpiani G., Pergolini M., Di Perna C., “Experimental comparison between three types of opaque ventilated facades”,Open Jour. Build. Constr. (2018).